UNIVERSITÀ DEGLI STUDI DI BRESCIA

DIPARTIMENTO DI INGEGNERIA DELL'INFORMAZIONE

DOTTORATO DI RICERCA IN TECHNOLOGY FOR HEALTH

Settore Scientifico Disciplinare: IIND-04/A

CICLO XXXVII

DEVELOPMENT OF 3D PRINTED SENSOR-BASED TOOLS TO ENHANCE NEUROSURGICAL LEARNING EXPERIENCE

Dottorando
Giacomo Santona

Supervisors

Antonio Fiorentino, Università degli Studi di Brescia

Mauro Serpelloni, Università degli Studi di Brescia

Francesco Doglietto, Università Cattolica del Sacro Cuore, Roma

Abstract

The endoscopic transsphenoidal approach (ETA) is a novel approach used by both neurosurgeons and otolaryngologists to treat the pituitary adenoma, a tumor that grows near the pituitary gland. The procedure starts by inserting surgical instruments from the nostril, then surgeons pass through the nasal cavity and approach the sphenoid sinus, where they start the dissection of the sphenoid bone in order to expose and then to remove the pituitary tumor. Two of the most delicate aspect of the surgery are the handling of the arachnoid membrane, which covers the tumor, and choosing the best strategy to remove the tumor, since the approach changes according to its hardness, a parameter that is difficult to predict during the preoperative planning phase. The arachnoid is one of the three meninges, which are thin membranes that surround the brain and the spinal cord. It consists of two parts: the external arachnoid barrier cell membrane and the arachnoid trabeculae, a spider web-like structure where the cerebrospinal fluid (CSF) flows. The tumor growth deforms the membrane which, pushed by the internal pressure of the CSF, collapses inside the sella turcica during the removal of the adenoma, in a sort of curtain effect, covering the remains of the tumor. The surgery can be considered successful only if the whole tumor is removed. Otherwise, it could grow back from its remnants, meaning that the patient would have to return to the operating room. The arachnoid membrane is very fragile; therefore, surgeons must exercise caution when moving it to search for any tumor remains. In particular, inexperienced surgeons must learn how to perform such maneuvers safely during tumor removal, since tearing the arachnoid membrane is associated with the potentially life-threatening complication risk of post-operative CSF leak.

It is well recognized that ETA has a long learning curve, which requires integrated and specific training. A review of the literature was conducted to investigate all the different training solutions that are available to surgeons to gain experience, besides entering the operating room and learning on the field. From a state of the art analysis, the training solutions available can be grouped into four categories: cadaveric head, animal head, 3D printed model and virtual/augmented reality simulators. What emerged is the lack of a reproduction of the arachnoid collapse during simulation and the lack of a repeatable way to simulate the pituitary adenoma, which is based only on the surgeons' experience. One of the most interesting solutions for its effectiveness and availability is the use of boiled egg white.

From the results of the review the aims of this thesis were defined:

- to develop of a sensor-based system to overcome the lack of a proper representation of the arachnoid collapse in a training solution

- to study the mechanical properties of pituitary adenoma, by developing a new surgical instrument, to both help surgeons during the surgery and to find a more accurate representation of the tumor in future training models.

The first part of the thesis describes the development of the 3D printed sensorized system to reproduce the arachnoid, from the prototype to the final version tested with experienced surgeons. The training model novelty consists of a sensor-based system that enables surgeons to physically interact with a representation of the arachnoid membrane during transsphenoidal surgery. In addition, the system provides surgeons with real-time feedback on the force applied to the membrane. Through validation tests with experienced neurosurgeons and otolaryngologists, it was possible to establish a preliminary threshold value above which the force applied to the membrane causes it to tear. The membrane is very thin and fragile, and its tearing during surgery can cause CSF leakage, which can increase the patient's risk. Consequently, surgeons should receive training to handle such delicate membranes prior to entering the operating room, thereby reducing the risk of tearing the arachnoid membrane. The system that has been studied was implemented in an already developed training model obtained from Computed Tomography (CT) data of a patient. It consists of a container filled with distilled water to mimic the CSF, closed on the surface by a layer of polymeric film, to mimic the arachnoid membrane, as found in literature. The final version of such system, named “tank”, was designed and 3D-printed on a Stratasys Dimension BST1200es in ABS, to ensure better water tightness. The tank was designed to be mounted to the training model, in order to increase realism. The aim of this innovative system is to evaluate the force applied by the surgeon when pressing the membrane and to find a threshold value, above which the force exerted can be dangerous for the patient. To measure the force applied to the membrane, a pressure sensor was connected to the tank to register the variation of pressure of the CSF induced by an external force on the polymeric arachnoid membrane. The system was then characterized using an indenter with a load cell mounted, which records the contact force. Using a curette mounted on a micrometric slide, the polymeric film was pressed as in real surgery. Then, the model with the tank equipped was tested by eleven international surgeons, and a first threshold value above which the force exerted by the surgeons breaks the arachnoid was determined. During the simulation, in order to increase the realism, a reproduction of the pituitary adenoma made with boiled egg white was added. A preliminary value of maximum force was found from the experience with surgeons. The threshold found is in line with the literature, which describes the level of force measured during a real ETA using a curette with a load cell within.

The second part consists of the design of a novel instrument to test the hardness of the pituitary adenoma intraoperatively. The aim is to directly measure the hardness of the pituitary tumor in vivo, providing surgeons with important data on the consistency of the specific tumor they are removing, allowing them to choose the best strategy and reduce potential errors. The instrument, named “probe”, consists of three parts:

- a rigid case, which was 3D printed in PLA
- a magnet with a tunnelling magneto-resistive (TMR) sensor
- a highly deformable tip

The tip consists of a circular plate with thin and highly flexible beams, which is folded on the rigid case, and glued through the beams; the circular base is thus the contact point. The tip was 3D printed in TPU to enhance its deformability.

The idea is to measure the hardness of materials through the deformation of the tip when a known displacement is applied. Using a TMR sensor with a magnet fixed on a highly deformable tip, it is possible to determine the deformation of the tip according to the movement of the magnet. In particular, the harder the sample tested, the greater the deformation of the tip. This particular use of a TMR sensor represents the main novelty of the project: the evaluation of the mechanical properties, in this case the hardness of soft tissues, by measuring the deformation of the tip, which is determined as the displacement undergone by the magnet during compression of the instrument. This choice makes it possible to have a closed environment for the electronics, thus enabling sterilization processes.

The main challenge of this project is to develop a probe with a maximum diameter of 5 mm, capable of fitting within the nasal cavities to perform intraoperative tests. The probe was fabricated by Fused filament fabrication (FFF) additive manufacturing. The case was made in PLA, while the tip was made in flexible TPU. Three prototypes were designed and tested: the first was developed to determine whether the system is capable of discerning different soft materials, i.e. silicones, but the overall diameter of the instrument was not suitable. With the second prototype the design was improved to fit the probe within the nasal cavities, and tests were performed using an egg white sample. The development of the final prototype focused its attention on the fabrication process of the tip: in particular, the goal was to enhance the sensitivity of the instrument, without losing its stability. An optimal combination of the printing parameters and the design of the tip was found.

Sommario

L'approccio endoscopico transfenoidale (ETA) è una tecnica innovativa utilizzata da neurochirurghi e da otorinolaringoiatri per rimuovere l'adenoma ipofisario, un tumore che cresce vicino alla ghiandola pituitaria, o ipofisi. L'intervento comincia inserendo strumenti chirurgici nella narice, dopodiché i chirurghi, passando attraverso la cavità nasale, raggiungono il seno sfenoidale, dove iniziano la dissezione dell'osso sfenoide per esporre e rimuovere il tumore ipofisario. Due degli aspetti più delicati dell'intervento sono: gestire l'aracnoide che tende a coprire i resti dell'adenoma da rimuovere e la scelta della migliore strategia per rimuovere il tumore, poiché l'approccio cambia in base alla sua durezza, un parametro difficile da prevedere durante la fase di pianificazione preoperatoria. L'aracnoide è una delle tre meningi, ovvero delle sottili membrane che circondano il cervello e il midollo spinale. È composta da due parti: la membrana aracnoidea esterna e lo spazio aracnoideo, una struttura simile a una ragnatela al cui interno scorre il liquido cerebrospinale (CSF). La crescita del tumore deforma la membrana che, spinta dalla pressione interna del CSF, collassa all'interno della sella turcica durante la rimozione dell'adenoma, in una sorta di effetto tenda, coprendo i resti del tumore. L'intervento può essere considerato di successo, se l'intero tumore viene rimosso, in caso contrario, i residui del tumore potrebbero causarne la ricrescita, rendendo necessario un nuovo intervento chirurgico. La membrana aracnoidea è molto fragile, pertanto, i chirurghi devono prestare molta attenzione quando la muovono per cercare eventuali resti del tumore. In particolare, i chirurghi inesperti devono imparare a eseguire tali manovre in sicurezza, poiché la rottura dell'aracnoide con conseguente fuoriuscita del CSF è associata al rischio di complicanze potenzialmente letali per il paziente.

L'intervento ha una lunga curva di apprendimento e quindi richiede una formazione integrata e specifica per i chirurghi. Per capire meglio come tale formazione venga fatta è stata condotta una revisione della letteratura per investigare tutte le diverse soluzioni di formazione disponibili per i chirurghi per acquisire esperienza, oltre all'entrare in sala operatoria ed imparare sul campo. Da un'analisi dello stato dell'arte, le soluzioni di formazione disponibili possono essere raggruppate in quattro categorie: teste di cadaveri umane e animali, modelli stampati in 3D e simulatori di realtà virtuale e/o aumentata. Ciò che è emerso è la mancanza di una riproduzione del collasso aracnoideo e la mancanza di un modo ripetibile per simulare l'adenoma ipofisario, che si basa solo sull'esperienza dei chirurghi. Una delle soluzioni più interessanti per la sua efficacia e disponibilità è l'utilizzo dell'albume d'uovo cotto.
Dai risultati della revisione sono stati definiti gli obiettivi di questa tesi:

- sviluppare un sistema basato su sensori per superare la mancanza di una rappresentazione adeguata del collasso aracnoideo durante la formazione chirurgica;
- studiare le proprietà meccaniche dell'adenoma ipofisario, sviluppando un nuovo strumento chirurgico, per avere una valutazione diretta della durezza della massa tumorale in sala operatoria e trovare una rappresentazione più accurata del tumore in futuri modelli di addestramento.

La prima parte della tesi descrive lo sviluppo del sistema sensorizzato stampato in 3D per riprodurre l'aracnoide, dal prototipo alla versione finale testata con chirurghi esperti. La novità di questo modello di *training* consiste in un sistema basato su sensori che consente ai chirurghi di interagire fisicamente con una rappresentazione della membrana aracnoidea durante la chirurgia transfenoidale. Inoltre, il sistema fornisce ai chirurghi un feedback in tempo reale sulla forza applicata alla membrana. Da dei test di validazione con neurochirurghi e otorinolaringoiatri esperti è stato possibile stabilire un valore di soglia preliminare oltre il quale la forza applicata sulla membrana ne provoca la lacerazione. La membrana è molto sottile e fragile, e la sua rottura durante l'intervento può causare perdite del CSF, aumentando il rischio per il paziente. Di conseguenza, i chirurghi dovrebbero ricevere una formazione specifica nel gestire tali membrane delicate prima di entrare in sala operatoria, riducendo così il rischio di rottura. Il sistema studiato è stato implementato in un modello di addestramento già sviluppato ottenuto dai dati di Tomografia Computerizzata (CT) di un paziente. Tale sistema consiste in un contenitore riempito con acqua distillata che simula il CSF, chiuso in superficie da uno strato di pellicola polimerica, che simula l'aracnoide, come trovato in letteratura. La versione finale di tale sistema, denominata *tank*, è stata progettata e stampata in 3D su una *Stratasys Dimension BST1200es* in ABS, per garantire una migliore tenuta dell'acqua. Il *tank* è stato progettato per essere montato sul modello di addestramento, al fine di aumentare il realismo. L'obiettivo di questo sistema innovativo è di valutare la forza applicata dal chirurgo quando preme sulla membrana e trovare un valore soglia, oltre il quale la forza esercitata può essere pericolosa per il paziente. Per misurare la forza applicata alla membrana, un sensore di pressione è stato collegato al *tank* per registrare la variazione di pressione del CSF indotta da una forza esterna sull'aracnoide. Il sistema è stato poi caratterizzato utilizzando un indentatore con una cella di carico montata, che registra la forza di contatto. Utilizzando una curetta montata su un cursore micrometrico, la pellicola polimerica è stata pressata come in un intervento reale. Successivamente, il modello con il *tank* equipaggiato è stato testato da undici chirurghi internazionali con cui è stato possibile determinare un primo valore di soglia oltre il quale la forza esercitata romperebbe l'aracnoide. Il valore soglia trovato è in linea con la letteratura, che descrive il livello di forza misurato durante un ETA reale utilizzando una

curetta con una cella di carico. Durante la simulazione, per aumentare il realismo, è stata aggiunta una riproduzione dell'adenoma ipofisario realizzata con albume d'uovo bollito, come suggerito dalla letteratura, nei cosiddetti *EggHead,* modelli di training nei quali la regione sellare è simulata con un uovo sodo.

La seconda parte consiste della tesi descrive la progettazione di un nuovo strumento per testare la durezza dell'adenoma ipofisario direttamente in sala operatoria. L'obiettivo è quello di misurare direttamente la durezza del tumore ipofisario durante l'intervento, fornendo ai chirurghi dati importanti sulla consistenza del tumore specifico che stanno asportando, consentendo loro di scegliere la strategia migliore e di ridurre i potenziali errori. Lo strumento, denominato "sonda", è composto da tre parti:

- una custodia rigida, stampata in 3D in PLA,
- un magnete con un sensore a magnetoresistenza tunnel (TMR),
- una punta ad alta deformabilità.

La punta consiste in una piastra circolare con attorno travi sottili e ad alta deformabilità, che viene ripiegata sulla custodia rigida ed incollata dalle travi; la piastra circolare è quindi il punto di contatto dello strumento con la superficie da misurare. La punta è stata stampata in 3D in TPU data la sua alta deformabilità.

L'idea è quella di misurare la durezza dei materiali attraverso la deformazione della punta quando viene applicato uno spostamento noto. Utilizzando un sensore TMR con un magnete fissato su una punta, è possibile determinare la deformazione in base allo spostamento del magnete. Più duro è il campione testato, maggiore è la deformazione subita dalla punta. Questo particolare utilizzo di un sensore TMR rappresenta la principale novità del progetto: la valutazione delle proprietà meccaniche, in questo caso la durezza, di tessuti soft, tramite la misura della deformazione della punta, determinata come lo spostamento subito dal magnete durante la compressione dello strumento. Questa scelta consente di avere un ambiente chiuso in cui disporre l'elettronica, permettendo così i processi di sterilizzazione.

L'aspetto più complesso di questo progetto è sviluppare una sonda con un diametro non più grande di 5 mm, che riesca quindi ad arrivare fino al tumore per eseguire test intraoperatori. Della sonda sono stati progettati e testati tre prototipi: il primo è stato sviluppato per determinare se il sistema è in grado di distinguere diversi materiali *soft*, ad esempio i siliconi. Con il secondo prototipo il design è stato migliorato per adattare la sonda alle cavità nasali, e sono stati eseguiti test utilizzando un campione di albume d'uovo. Lo sviluppo del prototipo finale si è concentrato sul processo di fabbricazione della punta: in particolare, l'obiettivo era

migliorare la sensibilità dello strumento, senza perdere la sua stabilità. È stata trovata una combinazione ottimale dei parametri di stampa e del design della punta.

Table of Contents

ABSTRACT II

SOMMARIO V

TABLE OF CONTENTS IX

CHAPTER 1 STATE OF THE ART 1

1.1 Introduction 1

1.2 Material and Methods 3

1.2.1 Search Strategy 3

1.2.1.1 Inclusion and exclusion criteria 3

1.2.1.2 Quality assessment and data extraction 3

1.3 Results 5

1.3.1 Enhanced Cadaver models 6

1.3.2 Animal models 7

1.3.3 Artificial models 8

1.3.3.1 Box-Trainer 8

1.3.3.2 CT-based models 9

1.3.4 Training simulators 11

1.3.4.1 Virtual Reality simulators 11

1.3.4.2 Augmented Reality simulators 12

1.3.5 Models and simulators for Surgical Planning 14

1.4 Discussion 14

1.5 Conclusions 16

CHAPTER 2 FABRICATION OF THE TRAINING MODEL 18

2.1 Design of the model 19

2.1.1 Selection of materials and processes 20

2.2 Results and Discussion 32

2.2.1 3D printing 32

2.2.2 Fabrication of silicone molds 33

2.2.2.1 Face mold 37
2.2.2.2 Turbinates mold 37
2.2.2.3 Silicone parts 38
2.2.3 TRAINING MODEL MOUNTED 39
2.2.4 PRELIMINARY VALIDATION 40
2.3 CONCLUSIONS 42

CHAPTER 3 DEVELOPMENT OF A SENSOR-BASED SYSTEM TO REPRODUCE THE FALL OF THE ARACHNOID 44

3.1 INTRODUCTION 44
3.2 THE ETA SENSOR-BASED TRAINING MODEL 45
3.2.1 THE ELECTRONIC SETUP 45
3.2.2 PROTOTYPE 1 - CONCEPT 49
3.2.2.1 Materials and methods 49
3.2.2.2 Characterization of the first prototype 50
3.2.3 PROTOTYPE 2 – SENSOR-BASED TANK 57
3.2.3.1. Materials and Methods 57
3.2.3.2 Results 61
3.2.2.3 Discussions 66
3.3 CONCLUSIONS 68

CHAPTER 4 SENSOR-BASED INSTRUMENT TO MEASURE THE HARDNESS OF PITUITARY ADENOMAS 69

4.1 THE CONCEPT 70
4.2 DESIGN OF THE PROBE AND FABRICATION 71
4.3 THE ELECTRONIC SETUP 73
4.3.1 Sensor Characterization 75
4.3.2 Probe Characterization – Indentation Tests 75
4.4 SENSOR-BASED TISSUE PROBE PROTOTYPES 76
4.4.1 PROTOTYPE 1 - CONCEPT 77
4.4.1.1 TMR Characterization 77
4.4.1.2 Sample Preparation 79
4.4.1.3 Prototype 1 - Results 80

4.4.2 PROTOTYPE 2 – WORKING PROBE 82
4.4.2.1 TMR Characterization 82
4.4.2.2 Sample tested 84
4.4.2.3 Results – Prototype 2 85
4.4.3 PROTOTYPE 3 – OPTIMIZED PROBE 88
4.4.3.1 The new highly deformable tip 88
4.4.3.2 Process Characterization of the tip 89
4.4.3.3 Indentation tests 96
4.5 CONCLUSIONS **103**

CHAPTER 5 CONCLUSIONS AND FUTURE STUDIES **105**

REFERENCES **110**

Chapter 1

State of the Art

1.1 Introduction

The Endoscopic Transsphenoidal approach (ETA) surgery is a novel surgical technique that recently evolved in endoscopic skull base surgery [1]. Both neurosurgeons and otolaryngologists use it to treat pituitary adenoma (PA), a tumor that grows near the pituitary gland. The procedure starts by inserting surgical instruments from the nostrils, then surgeons pass through the nasal cavity and approach the sphenoid sinus, where they start the dissection of the sphenoid bone in order to expose and then to remove the pituitary tumor. Throughout the years, there has been increased knowledge of how to take advantage of the relatively large median and paramedian corridors to the base of the skull base [2–5], the indications for this surgery have been expanding, together with its complexity.

One of the most delicate aspects of surgery is the correct handling of the arachnoid membrane. The arachnoid is one of the three meninges, which are thin membranes that surround the brain and the spinal cord. Its fragility is widely recognized among surgeons, who must exercise caution when interacting with it. In fact, during tumor removal, it collapses inside the sella turcica in a sort of curtain effect due to the internal pressure of the CSF, which ranges from 10 to 20 mmHg in healthy adults [6]. So, the arachnoid may cover the remains of the tumor, and surgeons must carefully move the membrane to check for residual tumor parts to be removed. Inexperienced surgeons must learn how to perform such maneuvers safely during tumor removal to avoid damage to the arachnoid, which is associated with the potentially life-threatening complication risk of post-operative CSF leak. However, as already mentioned, the arachnoid collapse is something still unfamiliar with all the available training solutions (both commercial and experimental) [7]. In fact, the reproduction of the arachnoid membrane was only mentioned by Lin et al. [8], and it was simulated with polymeric film and water-insoluble tissue paper in a model by Harada et al. [9] for other surgeries.

It is well recognized that ETA surgery has a long learning curve [10], which requires integrated and specific training [11]. Though traditional neurosurgical training is still primarily based on experience in the operating room, many complementary methods are now available. The cadaver laboratory has been classically used to acquire basic technical skills and knowledge of detailed surgical anatomy. Still, high maintenance costs and the challenge of

simulating pathologies might limit its utility. Thanks to 3D printing technologies, it has become possible to create customized models replicating normal and pathological anatomy [12]. Furthermore, thanks to virtual reality (VR) development, simulators may provide a repeatable experience in a more complex anatomical environment. In addition, the development of Augmented Reality (AR) simulators might enhance the quality of training.

In this evolving scenario, a review was conducted to explore and categorize every training solution reported in literature that is nowadays available to learn all the necessary skills to successfully perform ETA. PubMed and Scopus databases were analyzed using specific research keywords, additionally, commercially available solutions which were not reported in the literature were found with Google research. The described models were grouped into 4 major categories: (1) enhanced cadaveric heads, (2) animal models, (3) training artificial solutions (with increasing complexity) and (4) training simulators (based on virtual or augmented reality). Finally, a fifth category of models was added, since it was found to be interesting, even though the purpose of the described solution was not primarily training, but pre-operative surgical planning. This fifth category was called “pre-operative planning models and simulators”. In addition to acquiring the required skills for performing surgery on a real patient in an operating room setting, the gold standard for training is represented by human cadaveric heads, as they provide a more realistic representation of the human anatomy. However, their high maintenance costs and their low availability make them an inaccessible option. Conversely, virtual reality simulators, particularly augmented reality simulators and artificial models, offer an excellent alternative that has grown in popularity over recent years. Nevertheless, these simulators still lack haptic realism and anatomical fidelity, which renders them unsuitable for the acquisition of fundamental skills. The most comprehensive alternative thus far identified is the use of augmented reality in conjunction with human cadaver head models. This represents an encouraging prospect that may well undergo further development in the near future. However, it also emerged from the tumor at the majority of training solutions identified do not offer a realistic and cost-effective simulation of the most intricate and prevalent surgical procedure: the tumor removal with arachnoid preservation.

This section is adapted from the paper “Training models and simulators for endoscopic transsphenoidal surgery: a systematic review”, published in the journal Neurosurgical Review in September 2023 [7].

1.2 Material and Methods

1.2.1 Search Strategy

The state of the art was explored through a systematic review of literature, which was conducted following the PRISMA 2020 statement [13,14]. It was performed by searching articles from 1997 to 2022 on PubMed and Scopus, with the following keywords:

- training AND (transsphenoidal OR transnasal) AND (phantom OR simulator OR model)
- physical AND (simulator OR phantom OR model) AND (endoscopic endonasal)
- (Pituitary OR hypophysis) AND surgery AND training AND (model OR phantom OR simulator)
- (transsphenoidal) AND ((3D print*) OR (three dimension* print*))
- ((3D print*) OR (three dimension* print*)) AND tumor AND pituitary OR hypophysis; (Endoscopic endonasal) AND ((3D print*) OR (three dimension* print*))
- (neurosurgical) AND training AND ((phantom) OR (model) OR (simulator)) AND (3D print*) OR (three dimension* print*)
- (Skull base) AND (surgery) AND (training) AND ((model) OR (phantom) OR (simulator)).

Additional references and models or simulators used for training in endoscopic transsphenoidal surgery were identified by reference analysis and investigations on the web using the Google search engine.

1.2.1.1 Inclusion and exclusion criteria

Inclusion criteria were: English Language, training models, or simulators for endoscopic transsphenoidal surgery.

Exclusion criteria were the following: non-English language, papers unavailable at our libraries, Models/Simulators for other surgical interventions, and other studies (e.g., reviews with no novel data).

1.2.1.2 Quality assessment and data extraction

Articles were imported into the reference management software Zotero (version 6.0.8), and duplicates were removed. For each selected study, an accurate full-text analysis was

performed to extract the following information about the training model or simulator, when available: reproduced anatomy, data on training and validation studies, and costs.

The selected studies were divided into the following categories (Fig. 1.1):

1. Enhanced Cadaver models (ECH)
2. Animal models (AM)
3. Artificial models

   3.1 Box-Trainers

   3.2 CT-based: mono-material model (m), multi-material model (M), and the “EggHead”
4. Training simulators: Virtual Reality (VR) simulator and Augmented Reality (AR) simulator
5. Preoperative planning models/simulators.

The difference between "model" and "simulator" is that simulators are models in a virtual reality environment and with real-time feedback for the surgeon. Each training model/simulator was listed in a table based on the category. In addition, each model was described in the table reporting the following data when available:

- First author and year of publication for academic reports, or name of the developers and nation, for commercially available models/simulator (CA)
- Whether the model included the Tumor (T) and the Arachnoid Membrane (A) in their model
- Simulated Tasks for which the model was conceived and used
- Assessment or validation of the model
- The reported cost of the used materials or the retail price.

For the CT-based training models, a 5-point sub-column was added to evaluate their anatomical reliability and defined "anatomy score". The sub-column score gives an overall evaluation of the anatomical accuracy of the model; points are given according to the design of the model: +1 point per mono-material (m) models or +2 points for multi-material (M) ones M; +1 or +2 points according to the degree of reproduced details, such as the skin, dura mater, optic nerve or ICA; and +1 point if the tumor or the arachnoid are reproduced.

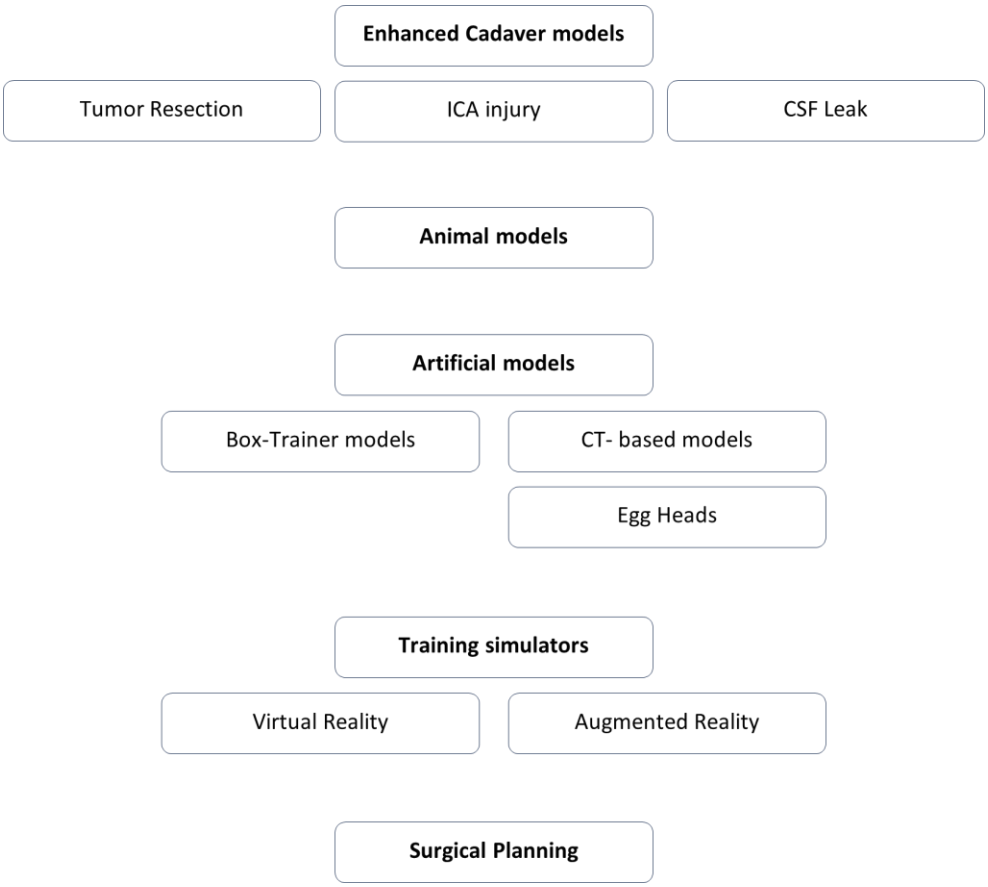

Fig. 1.1 Training Models and Simulators diagram.

1.3 Results

The initial literature search yielded 1199 articles: 675 from PubMed and 524 from Scopus. Of these articles, 568 were removed before screening because they were duplicates. The remaining 631 articles were screened and evaluated by title. At this point, 380 articles were excluded, and a full-text screening was performed to determine if the remaining 251 articles met the inclusion criteria. Of the 251 articles identified for retrieval, 2 were removed (because the full text was not available). 249 reports were screened for eligibility and 181 were removed because they did not meet the inclusion criteria, specifically 15 were removed because of language; 8 were removed because of experience with a pre-existing model or simulator; 76 were removed because the model/simulator described was used to simulate other surgeries; 51 were removed because no model/simulator was described in the reports; 9 were removed because they were designed for planning and 22 were removed because they were previous reviews of the literature. Finally, 101 reports were included in this systematic review, including 6 articles retrieved from previous papers [15–36] and 28 websites (Figure 1.2).

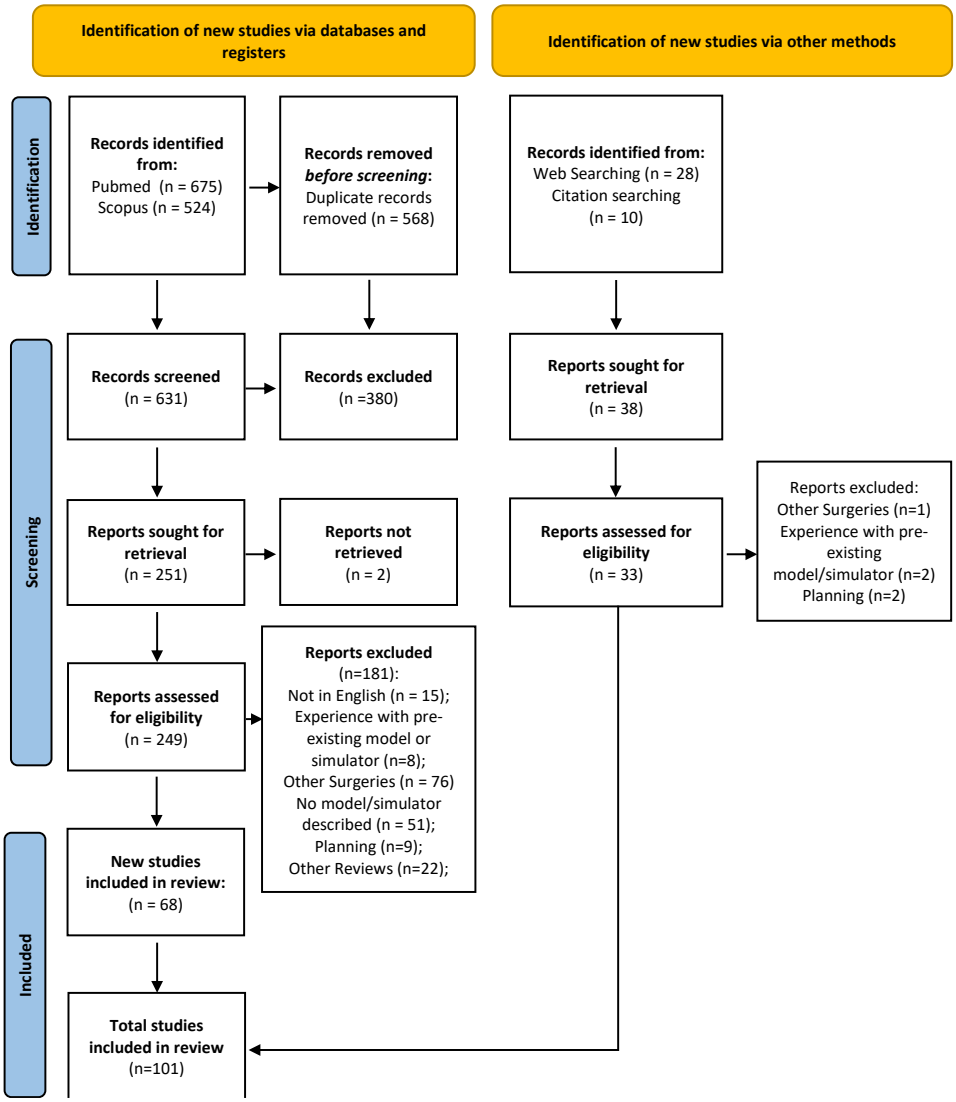

Fig. 1.2 PRISMA 2020 flow chart.

1.3.1 Enhanced Cadaver models

The cadaver-based training models can be divided into three main groups, according to the training experience they provide (Table 1.1): tumor resection [37–40], management of ICA injury [41–46], and CSF leak repair [45,47–49].

The tumor resection models are designed to train neurosurgeons to resect a sellar tumor [37–39]. The idea is based on the work of Gragnaniello et al., who injected resin into the sella turcica to mimic the texture and location of a pituitary tumor [39].

In ICA injury models, a red-dyed solution is pumped into the arterial system to mimic blood [41–46]; an ICA lesion is caused, and the surgeon can be trained to deal with it.

The CSF models are obtained by perfusing a water-based solution in the subarachnoid or subdural space so that the surgeon can be trained in skull base reconstruction [48–51].

Although anatomical specimens are intuitively used at their best only once, some models can be used multiple times for training, lowering their total cost [44,45,52]. For example, Mladina et al. [53] reported a cost of $1520 per resident.

Table 1.1. Enhanced cadaver models. The table reports the ECH models that have been modified to simulate different surgeries, the simulated task, who assessed the model, and whenever available, the cost.

FA/Dev. (YOP/Nation)	ECH		Simulated task	Assessment	Cost/Price
	Type	T			
Gragnaniello (2010) [39]	Tr	SRSP	SBS	Experts	n/a
Berhouma (2013) [37]	Tr	SRSP	EETA	Authors	n/a
Pham (2014) [42]	ICAI	-	ICAIR	Residents	n/a
Ciporen (2017) [43]	ICAI	-	ICAIR	Residents	600 $[a]
Pacca (2017) [44]	ICAI	-	ICAIR	Surgeons	n/a
Gagliardi (2018) [38]	Tr	SRSP	EETA	Surgeons	n/a
AlQahtani (2018, 2021) [50,51]	CSFL	-	CSFLR	Surgeons	n/a
Shen (2018) [45]	ICAI	-	ICAI	Surgeons	n/a
Christian (2018) [48]	CSFL	-	CSFLR	Residents	n/a
Donoho (2019, 2021) [41,46]	ICAI	-	ICAIR	Residents	275 $[b]
Mattavelli (2020) [49]	CSFL	-	CSFLR	Experts	n/a
Li (2022) [40]	Tr	-	ETTA	Surgeons	n/a

Abbreviations: $ = US dollars, $/head = US dollars x Cadaveric Head, $/trainee = US dollars x trainee, CSFL = Cerebrospinal fluid leakage, CSFLR = Cerebrospinal fluid leakage repair, Dev. = Developers, ECH = Enhanced Cadaver Models, EETA = Endoscopic Endonasal Transsphenoidal Approach, ETTA = Endoscopic Transnasal Transsphenoidal Approach, FA = First Author, ICAI = Internal Carotid Artery Injury, ICAIR = Internal Carotid Artery Injury Repair, n/a = not available, SBS = skull base surgery, SRSP = Stratathane resin ST-504 polymer, T = Tumor, Tr = Tumor resection.

[a] = 500-700 $ per cadaver head.

[b] = marginal cost per trainee

1.3.2 Animal models

These models use animals to provide training, on surgical instrumentation handling (Table 1.2). The animals include Wistar rats [54], sheep [55–59], and lambs [60,61,53,62]. In addition, one hybrid model included live sheep and has been specifically designed to manage ICA rupture.

Table 1.2. Animal-based models. The table reports animal-based training models, the simulated task, who assessed the model, and whenever available, the cost.

FA/Dev. (YOP/Nation)	Animal	Simulated task	Assessment	Cost/Price
Fernandez-Miranda (2010) [54]	Wistar rat	EESBS	Surgeons	n/a
Valentine (2011, 2016, 2016) [57–59]	Sheep[c]	ICAI	Authors	n/a
Mladina (2013) [61]	Lamb	CSFL	Authors	n/a
Awad (2014) [55]	Sheep	ERT	Surgeons	6$

Skitarelić (2015) [62]	Lamb	EESS	Authors	2$
Isaacson (2015) [56]	Sheep	ETr	Authors	n/a
Mallmann (2016) [60]	Lamb	EESS	Surgeons	n/a
Mladina (2018) [53]	Lamb	ESSBS	Residents	3-4$

Abbreviations: $ = US Dollars, CSFLR = Cerebrospinal Fluid Leak Repair, Dev. = Developers, EESBS = Endoscopic, Endonasal Skull-Base Surgery, EESS = Endoscopic Endonasal Sinus Surgery, ERT = Endoscopic Rhinology Tasks, ETr = Endoscopic Training, FA = First Author, ICAIR = Internal Carotid Artery Injury Repair, n/a = not available, YOP = Year Of Publication

[c] This model is hybrid as the SIMONT artificial model is also used.

1.3.3 Artificial models

By definition, these models are fabricated artificially. They can be divided into two major categories: the first is represented by the so-called Box-Trainers (Table 3), while the second comprises anatomically more realistic models (Table 4). Artificial training models are considered the most cost-effective alternative to cadaver-based training [63]. Tables 1.3 and 1.4 report each model's costs when available.

1.3.3.1 Box-Trainer

If compared to CT-based models, the anatomical accuracy of Box-Trainers is significantly lower, but they are easier to fabricate and cheaper. The models under this category are characterized by a box with two holes representing the head and the nostrils. Different materials and training modules can be used inside the box, e.g., chicken wing or tangerine [64–67], rings, and pegs, to create specifically designed exercises [68–73]. These models aim to develop the surgeon's dexterity [74]. The Box-Trainers are reported in Table 1.3.

Table 1.3. Non-anatomical (Box-Trainer). The table reports the Box-Trainers, the simulated task, who assessed the model, and whenever available, the cost.

FA/Dev. (YOP/Nation)	Box-Trainer			Simulated Task	Assessment	Cost/Price
	Type	T	A			
Hirayama (2013) [68]	E	-	-	HI	Surgeons	180$
Jusue-Torres (2013) [64]	F[d]	-	-	EEA	Surgeons	10$
Singh (2016) [69]	E	-	-	EES	Surgeons	100–150$
Sanromán-Álvarez (2017) [65]	EF	Egg	-	TP	Residents	n/a
Berkowitz (2017) [70]	E	-	-	TE	Students	n/a
Srivastav (2017) [71]	E[e]	-	-	HI	Novices	n/a
Xie (2018) [72]	EF	-	-	CSFLR	Surgeons	100$[f]
Altun (2020) [66]	F	CB	-	EETA	Experts	100$
Gallet (2021) [75]	EF	-	-	EES	Surgeons	n/a
Tikka (2022) [74]	F	-	-	EEA	Fellows	n/a
Bright (2022) [73]	E	-	-	TP	Surgeons	15$

Abbreviations: $ = US Dollars, A = Arachnoid, CB = the tumor was simulated with the medullar content of a chicken bone, CSFLR = Cerebrospinal Fluid Leak Repair, Dev. = Developers, E = Exercise Based Box-Trainer, EEA = Endoscopic Endonasal Approach, EES = Endoscopic Endonasal Surgery, EETA = Endoscopic Endonasal

Transsphenoidal Approach, EF = Exercise and Food based Box-Trainer, Egg = Chicken or Quail Egg used to mimic the content of the sella turcica, F = Food Based Box-Trainer, FA = First Author HI = Handling Instruments, n/a = not available, T = Tumor, TE = Transnasal Endoscopy, TP = Transnasal procedures, YOP = Year Of Publication.

[d] = additional training simulation with the chicken wing inside a Phacon training model.
[e] = improved version of Sing et al. Box-Trainer.
[f] = 15$ for the disposable parts.

1.3.3.2 CT-based models

These training models are developed from patient-specific CT data (Table 1.4). The overall level of anatomical accuracy is strongly related to the design, materials, and technology used. Some are mono-material solutions [76–78], while others are multi-material to reproduce the different tissues of the human head more accurately [66,79–82,8,83–94]. A brilliant and cheap solution frequently incorporated in CT-based models is the "EggHead", described by Engel et al. [81]: a chicken or quail egg reproduces the sellar region anatomy [40,75,77,80,81,88,92]. The eggshell mimics the sphenoid bone, the vitelline membrane is the dura mater, and the albumen and yolk represent the contents of the sella. According to Wen et al. [92], the egg may be raw or soft-boiled. Among multi-material training models, some are commercially available, such as SIMONT by ProDelphus [95], Kezlex: A22 [96], A39 [97], and A43 [98] by Japan Medical Company [99]. The Sinus Model Otorhino Neuro Trainer, SIMONT - Otorhino Surgical Trainer, is the training model developed which allows the performing of many neurosurgical operations [100], including removing the pituitary adenoma. One of the most innovative features is Neoderma®, the material developed by Pro Delphus used to mimic the mechanical properties of the skin and the mucous membranes [101–103]. The model is available on the website [104] for US$ 3798.00, while the portable version costs US$ 1630. In the literature, its use has been described by Valentine et al. [57–59]. Kezlex is a series of training models developed by Japan Medical Company [99]. Among all the training solutions [105], the most pertinent are models A22 [96], A39 [97], and A43 [98]. Oyama et al. described their experience with the A22 for various neurosurgical approaches. Maza et al. [85] described the A43 model. This training model was developed to help the neurosurgeon deal with a catastrophic ICA injury. The cost is not reported on the website, but Muto et al. [86] reported in their article the cost of the A43 model of $4000 plus $250 for the reusable platform.

Table 1.4. Training models. The table reports the Training model, including m (mono-material) models, M (multi-materials) models and EggHead, the simulated task, who assessed the model, and whenever available, the cost. The sub-column score gives an overall evaluation on the anatomical accuracy of the model, points are given according to the design of the model: +1 point per m models or +2 points for M; +1 or +2 points to the details reproduced such as the skin, the dura mother, the optic nerve or the ICA; and +1 point if the tumor or the arachnoid are reproduced.

FA/Dev. (YOP/Nation)	Training Model					Simulated Task	Assessment	Cost/Price
	Type/ Name	Anatomy	T	A	Score			
Briner (2007) [76]	m	PS	-	-	3/5	ESS	Experts	n/a
Chen (2010) [106]	M	Head	-	-	4/5	EETA	Authors	n/a
Okuda (2010) [77]	m	SB	Egg	-	2/5	EETA	Authors	n/a
Waran (2012) [91]	M	SB	-	-	3/5	ETr	Experts	n/a
Okuda (2014) [88]	M	Head	Egg	-	3/5	TP	Surgeons	n/a
Chan (2015) [107]	m	SB	-	-	2/5	ETr	Experts	600$[g]
Chan (2015) [107]	M	SB	-	-	3/5	ESS	Expert	900$[g]
Narayanan (2015) [87]	M	Head	-	-	3/5	TP	Surgeons	n/a
Engel (2015) [81]	M	Head	Egg	-	4/5	TP	Surgeons	2500[h]
Tai (2016) [90]	M	Head	-	-	3/5	EEA	Surgeons	500$[i]
Kashapov (2016) [82]	M	Head	SR	-	4/5	ESBS	Surgeons	200$[h]
Wen (2016) [92]	M	Head	Egg	-	4/5	EETA	Surgeons	n/a
Shah (2016) [78]	m	Head	-	-	2/5	EETA	Resident	n/a
Zheng (2018) [94]	M	Head	-	-	4/5	ESBS	Experts	500$[i]
Masuda (2018) [84]	M	Head	-	-	4/5	EETA	Authors	n/a
Lin (2018) [8]	M	SR	ns	ns[j]	4/5	ETA	Experts	n/a
Ding (2019) [80]	M	Head	Egg	-	5/5	EETA	Residents	n/a
Zheng (2019) [93]	M[k]	SR	ns	-	5/5	EETA	Residents	n/a
Shen (2020) [89]	M	Head	SG	-	5/5	EETA	Authors	n/a
London (2021) [83]	m	Head	-	-	3/5	PESS	Surgeons	63$[g]
Masalha (2021) [63]	M	Head	-	-	4/5	CSFLR	Surgeons	80$[g]
Lai (2021) [108]	M	Head	Pm	-	5/5	ESBS	Experts	570$[g]
Li (2022) [40]	m	Head	Egg	-	2/5	ETTA	Surgeons	200Y[g]
Li (2022) [40]	M	Head	-	-	4/5	ETTA	Surgeons	3000Y[g]
Pro Delphus (Brazil) [95]	SIMONT [104]	Head	ns	-		NT[100]	[57–59,102,103]	3798$ - 1630$
JMC (Japan) [99,105]	Kezlex [96–98]	Head	-	-		NT	[85,101,109,110]	n/a

Abbreviations: $ = US Dollars, € = Euros, CSFLR = Cerebrospinal Fluid Leak Repair, Dev. = Developers, EEA = Endoscopic Endonasal Approach, EETA = Endoscopic Endonasal Transsphenoidal Approach, Egg = Chicken or Quail Egg used to mimic the content of the sella turcica, ESBS = Endoscopic Skull-Base Surgery, ESS = Endoscopic Sinus Surgery, ETA = Endoscopic Transsphenoidal Approach, ETr = Endoscopic Training, ETTA = Endoscopic Transnasal Transsphenoidal Approach, FA = First Author m = mono-material, M = Multi-material, n/a = not available, ns = not specified, NT = Neurosurgical Training, PESS = Pediatric Endoscopic Sinus Surgery, Pm = polyvinyl alcohol cryogel mixed with water, PS = Paranasal Sinus, SB = Skull-Base, SG = Silica Gel, SR = Sellar Region, SBS = Skull Base Surgery T = Tumor, TP = Transsphenoidal Procedure, Y = Yuan, YOP = Year Of Publication.

[g] = cost per model

[h] = production cost

[l] = material cost

[j] = the arachnoid was reproduced for a non-transsphenoidal training model.

[k] = in the article are reported 3 different model, the M was chosen as it is considered the best option by the authors.

1.3.4 Training simulators

Training simulators can be divided into two categories, as they are either based on virtual (VR) or augmented reality (AR). Table 5 reports the relative costs of each model when available.

1.3.4.1 Virtual Reality simulators

VR simulators consist of a PC with a virtual environment software that represents the patient's data, and the surgeons interact with it by simulating actual surgeries using joysticks [111–113], special haptic devices [114–118] or surgical instruments [119]. Virtual reality simulators are a technologically advanced alternative to train surgeons to perform complex surgeries before they enter the operating room [4,64]. Two different VR simulators were found to be available online, the NeuroVR and Voxel-Man Sinus. The NeuroTouch-Endo, now NeuroVR, is the training simulator developed by NRC and NeuroSim [120] (Canada); it is a VR simulator that simulates endoscopic transnasal procedures [121] with MRI data for patient-specific features. In addition, it has haptic devices that provide force feedback [116,122], and it is available on the CAE website [123]. The Voxel-Man Sinus [124] is the training simulator developed by the University Medical Center Hamburg-Eppendorf (Germany) [125] for paranasal sinus surgery [126]. The Voxel-Man provides an accurate haptic and visual representation of surgery and is based on standard PC hardware [127]. The Voxel-Man can be purchased [128] for $ 145,255.95$ [129].

1.3.4.2 Augmented Reality simulators

AR simulators are VR simulators where surgeons interact with a physical, CT-based [107,130–133] or cadaver [119,133–137] head. Additionally, Cai et al. [138] developed an application that can be used for AR simulators. Two models were available for purchase, the Phacon Sinus Trainer and the TNS Box.

The PHACON Sinus Trainer comprises a series of simulators developed by Phacon GmbH (Germany) [139]. The most suitable for this review were found with the web research: the [S-00005] PHACON Sinus Trainer [140], available at 8.910€ [141], and the [S-00007] PHACON Sinus Assistant [142], purchasable at 1.870€ [143]. The module for the transnasal approach, the [SN-ah] PHACON Sinus Patient "Meyer" – pituitary tumor, can be purchased separately for 290€ [144]. The simulator consists of a multi-material modular head connected via visual registration to specially developed software that assists the neurosurgeon by providing CT data displayed as a virtual 3D model; it can automatically detect injuries to high-risk structures. The TNS Box is one of the multiple simulators developed by UpSurgeOn [145]. It consists of an anatomically accurate modular and multi-material simulator designed explicitly for the transsphenoidal approach to the pituitary gland. The simulator comprises an external box with a disposable nasal cavity and a face mask on the front. The TNS is provided with an App available on the App Store or Google Play, which improves the training experience with a virtual reality environment [146]. The TNS is now available at UpSurgeOn website [147] at €599 - €699. It is also possible to purchase disposable nasal cavities separately [148]. Two articles reported a positive experience with the simulators [149,150]. In Table 1.5 are reported the Training Simulators found.

Table 1.5. Training Simulators. The table reports VR and AR simulators. In the sub-column "Devices" is reported the tools that surgeons use to interact with the simulator, while the sub-column "Model" is for the AR simulators only, and it is reported the physical model where the simulation is performed.

FA/Dev. (YOP/Nation)	Training Simulator					Simulated Task	Assessment	Cost
	Type/Name	Devices	Model	T	A			
Wolfsberger (2004, 2006) [111,113]	VR	Joystick	-	T	-	EETA	Authors	n/a
Pößneck (2005) [114]	VR	Haptic	-	-	-	ESS	Residents	n/a
Neubauer (2005) [112]	VR	Joystick	-	T	-	EETA	Authors	n/a
Dixon (2011, 2012, 2014) [134–136]	AR	Instruments	CH	-	-	ESBS	Experts	n/a
Prisman (2011) [137]	AR	Instruments	CH	-	-	ESBS	Surgeons	n/a
De Notaris (2013) [119]	VR	Instruments	CH	-	-	EEA	Residents	n/a
Varshney (2014) [116]	VR[l] [120]	Haptic	-	-	-	ESS	Authors	n/a
Li (2016) [133]	AR	Instruments	m, CH	-	-	ESBS	Surgeons	n/a
Won (2018) [117]	VR [151]	Haptic	-	-	-	ESBS	Authors	n/a
Barber (2018) [130]	AR	Instruments	m	T	-	ESS	Authors	1000$
Heredia-Pérez (2019) [118]	VR	Haptic	-	T	-	REETA	Surgeons	n/a
Lai (2020) [131,132]	AR	Instruments	m	-	-	ESBS	-	n/a
Kim (2020) [152]	VR	Haptic	-	-	-	ESSBS	Experts	n/a
Cai (2022) [138]	AR[m]	-	-	T	-	PTR	-	n/a
UKE (Germany) [124,125]	Voxel-Man Sinus	Instruments	-	-	-	ESS [126]	[127]	145,255.95$ [128,129]
NRC and NeuroSim (Canada) [120]	NeuroVR	Instruments	-	T	-	NT [121]	[116,122]	n/a [123]
Phacon GmbH (Germany) [139]	Phacon	Instruments	M	-	-	NT [140,142]	[64,153]	1870€ [143]; 8910€ [141]; 290€ [144]
UpSurgeOn S.r.l. (Italy) [145]	TNS	Instruments	M	T	-	EETA [146]	[149]	599-€699€ [147]; disp.: n/a [148]

Abbreviations: $ = US Dollars, € = Euros, A = Arachnoid, CH = Cadaver Head, Dev. = Developers, disposable n/a = Disposable cavities cost not available, EEA = Endoscopic Endonasal Approach, EETA = Endoscopic Endonasal

Transsphenoidal Approach, ESBS = Endoscopic Skull-Base Surgery, ESS = Endoscopic Sinus Surgery, ESSBS = Endoscopic Sinus and Skull-Base Surgery, FA = First Author, m = mono-material Head, M = Multi-material Head, n/a = not available, NT = Neurosurgical Training, disp = disposable cavities, PTR = Pituitary Tumor Resection, RTBTR = Robotic Transsphenoidal Brain Tumor Resection, YOP = Year Of Publication.

[l] = Simulator developed upon the NeuroVR platform.

[m] = Application for AR training simulator.

1.3.5 Models and simulators for Surgical Planning

Table 1.6 reports models and simulators conceived for surgical planning, which are not included in this systematic review but might help neurosurgeons improve their knowledge on the subject [22,154–162].

Table 1.6. Surgical Planning training models/simulators: the model and simulators reported in this table are those designed to help neurosurgeons during preoperative planning.

FA/Dev. (YOP/Nation)	Surgical Planning Model/Simulator				Planning	Assessment	Cost
	Type/Name	Anatomy	T	A			
Shinomiya (2018) [22]	m	SR	BR	-	EETA	Experts	n/a
Zhang et al. (2018) [162]	m	PS-SB	-	-	PSS	Experts	3$/m
Huang (2019,2021) [156,157]	m	SR	T	-	EETA	Authors	900-1500Y
Panesar (2021) [159]	M	SB	T	-	ESBS	Experts	3-40$/m
Chaudhary (2021) [154]	m	SR	T	-	EETA	Experts	n/a
Chopra (2021) [155]	m	SR	T	-	EETA	Authors	n/a
Bracco Group (Italy) [163]	Dextroscope	Head	-	-	NT	[158,160,161]	n/a

Abbreviations: $ = US Dollars, A = Arachnoid, BR = Blue Resin (Vero Cyan®, Stratasys), Dev. = Developers, EETA = Endoscopic Endonasal Transsphenoidal Approach, ESBS = Endoscopic Skull-Base Surgery, FA = First Author, m = mono-material, M = Multi-material, n/a = not available, NT = Neurosurgical Training, PSS = Paranasal Sinus Surgery, PS-SB = Paranasal Sinus – Skull-Base, SB = Skull-Base, SR = Sellar Region, T = Tumor, Y = Yuan, YOP = Year Of Publication.

1.4 Discussion

It is recognized that the endoscopic endonasal transsphenoidal approach has a long learning curve [10]. To ensure safe and effective surgery, it is crucial to have excellent hand-eye coordination under the endoscopic vision and make sound clinical and intraoperative judgments. The required confidence can only be achieved after many surgeries in the operating room. However, this learning process can be sped up with proper training in a safe environment outside the operating room. This review aimed to show all alternatives for training in endoscopic transsphenoidal surgery. We found four categories of training systems:

Enhanced cadaver head training models, Animal models, Training Models (CT-based, Box-Trainer, and EggHead), and Training Simulators (Virtual Reality and Augmented Reality).

Human cadaver heads remain the gold standard for training: the anatomical reliability is still higher if compared to every other option [29]. However, their low availability [23,49,50] and the fact that they are suitable for limited training experience, makes them an expensive and not easily accessible option [48]. Costs of one human cadaveric head range from almost 600$ [52] to 1000$ [82], while Mladina et al. [53] reported a cost of 1520$ per resident for training. In addition, the maintenance costs of anatomy laboratories are high [34]. Using Animal heads is a cheap and readily available option, but the anatomy is divergent [62]. Nevertheless, they can be considered a good alternative as an inexpensive and simple system to teach residents the dexterity required to fully exploit the more expensive cadaver head, as stated by Mladina et al. [53]. Their main advantages are the costs, which are lower than 6$ [53,55,62], making them the cheapest solution for initial training.

Compared to human and animal specimens, Training Models have the advantage of being versatile. The developers can choose the anatomical accuracy level they want to obtain, which is related to the costs of the system. Modular solutions, in which not all parts are disposable, are a way to optimize the costs of this solution. Among the different solutions, the Box-Trainers are cheaper and easier to fabricate. However, the low degree of anatomical accuracy makes them suitable as a first tool to teach how to handle surgical instruments in the narrow space of the nasal cavities, and they can be a useful first experience before training with more expensive models like the cadaveric head [74].

CT-based training models, on the other hand, potentially have a significantly higher level of accuracy related to the design complexity and the background knowledge required. The EggHead represents a brilliant solution as it mimics the sellar region with a chicken or quail egg in an economical and repeatable way [40,77,80,81,88,92]. What needs to be added is a reproduction of blood and CSF [87]; the latter was implemented only in the training model of Mashala et al. [63]. Costs are generally low but cannot be compared to each other due to the different criteria by which they were determined by the authors, as reported in table 4. They can be divided into three categories: cost per model, material cost and production cost.

VR training simulators provide visually the most complete experience to neurosurgeons. Their main advantage is the fact that the simulation can ideally be repeated an infinite number of times [34]. In addition, some of them also have a real-time feedback system that provides information about the position of the instruments, the level of forces reached and the performances of the trainees [23,116,122,127]. However, the lack of a "physical head" where to perform the surgery can be limiting, even if many sensors and haptic

devices have been studied and added [118]. Another defect of some VR systems is the low quality of the visual effects and the fact that the instruments used during training sessions differ from those used in the operating room [111–114,117,118,120,129,152]. The initial costs of VR training simulators are the highest among the different solutions, i.e. the Voxel-Man Sinus training simulator is available for 145,255.95$ [128,129]. However, the fact that surgeries can be simulated an indefinite number of times makes the cost of a single training session low if the system is used frequently.

AR simulators with cadaver heads may be the best solution for residents as they provide the best anatomy from the cadaver head and real-time feedback from the VR environment [133–136,158]. However, they may also be the most expensive solutions: a better trade-off to reduce cost may be an AR simulator based on a multi-material head. The costs available for the training simulators are those of the Phacon, 8910€ [141] or 1870€ [143] and 290€ [144] for the cartridge, and those of the TNS, 599-699€ [147] plus the costs of the disposable cartridge, which is not reported. Similar to CT-based training models, developing VR and AR simulators requires a high level of knowledge.

Finally, this review documents what is missing in most training solutions. Most are dedicated to the phase of the approach in surgery, while only a minority have developed simulators for sellar tumors and suprasellar arachnoid. Except for VR simulators, where the pituitary adenoma was implemented virtually, the sellar tumor has been simulated only in a few models using different materials. In addition, ECH models have been modified to allow training for dealing with ICA intra-operative rupture and CSF leak.

It might be of interest to develop a modular training model that provides a realistic simulation of both sellar tumors and suprasellar arachnoid to provide a cost-efficient way to train future generations not only in the surgical approach but also in the management of sellar tumors of different consistencies and the preservation of the arachnoid.

1.5 Conclusions

The training solutions for endoscopic transsphenoidal surgery are cadaveric (human or animal) or artificial models and virtual reality simulators. Human cadaveric specimens constitute the gold standard, as they provide a realistic environment, which specific modifications for managing ICA rupture, CSF leak, and tumor removal can enhance. Their availability is though relatively low due to relatively high costs. Virtual Reality simulators and artificial models provided an excellent alternative. However, the lack of haptic realism and anatomical fidelity makes them ideal for learning the basics. Augment reality applied to

cadaver-based models is an exciting solution that might be further developed in the near future.

Most artificial models do not provide a realistic and cost-efficient simulation of the most delicate and relatively common phase of surgery, i.e., tumor removal with arachnoid preservation; current research should optimize this to train future neurosurgical generations efficiently and safely.

Chapter 2

Fabrication of the Training Model

This chapter describes the procedures for the fabrication of a novel training model for ETA. The approach used was the reverse engineering. The model was developed starting from CT data of a patient's head. It consists of a modular structure where each of the modules represents an anatomical part of the head of the patient. Any anatomical part outside the "transsphenoidal route" or parts that the surgeon interacts with during surgery, were removed at the design stage, simplifying production, and saving time and materials. To obtain each module, the CT was converted into two different STL files: "skull-base", and "face", named after the anatomical part from which they are taken. STL files were edited using Meshmixer, a software developed by Autodesk for editing the mesh of 3D objects (Autodesk Inc., USA). From the skull base STL file, the sphenoid bone, the nasal septum, the turbinates, and the ethmoid bone modules were obtained; additionally, a non-anatomical module named frame was designed to be the basis for the assembly of the model. From the face model the nose module was obtained. Each module was fabricated with the additive manufacturing (AM) technology fused filament fabrication (FFF) on a Ultimaker 3 Extended, except for the nasal septum, which was printed in TPU and skin and the mucosa, which were produced in silicone. Finally, the chapter concludes with a preliminary validation of the model by an experienced neurosurgeon who provided feedback on it.

The following section is adapted from the paper “Fabrication of a training model for transsphenoidal approach surgery: from CT-data to Silicone casting” which will be submitted on Journal of Manufacturing and Materials Processing

2.1 Design of the model

The production of the CT-based training model started from CT (Computer Tomography) data of the head of a patient. The CT was performed using a 1 × 1 frame with contiguous slices at 1.5 mm and a gantry of angle 0°. The scan window diameter of 225 mm and a pixel size greater than 0.44 × 0.44. Images were then recorded on a CD in DICOM format. The DICOM file was then converted into STL (Standard Triangulation Language) file to be edited with Meshmixer (Autodesk Inc., USA). Using Meshmixer only, it was possible to obtain each module. Fig. 2.1 offers anticipation with an exploded view of the model with each module highlighted. They are, as already mentioned: the upper and lower sphenoid bone, the left and right turbinates, the ethmoid bone, the nose, and the non-anatomical frame. Their development is described in the following sections.

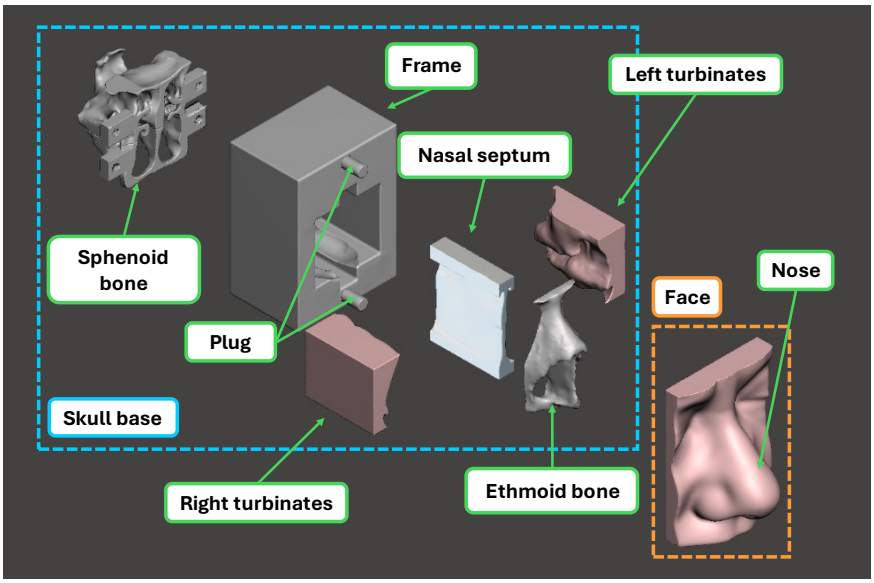

Fig. 2.1 Exploded view of the CT-based training model whit the modules highlighted.

From CT data, two base models were obtained: the Skull-base model, shown in Fig. 2.2 and the Face shown in Fig. 2.3. These models were then converted into STL and edited with Meshmixer, where the modules of the training model were obtained.

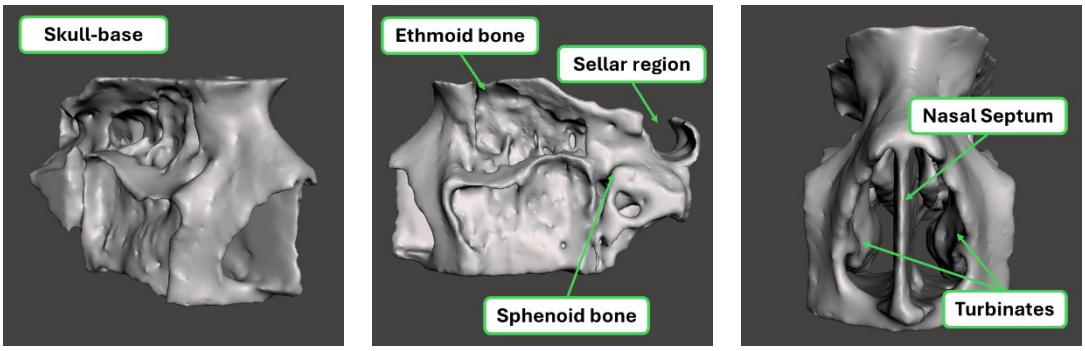

Fig. 2.2 Skull-base model.

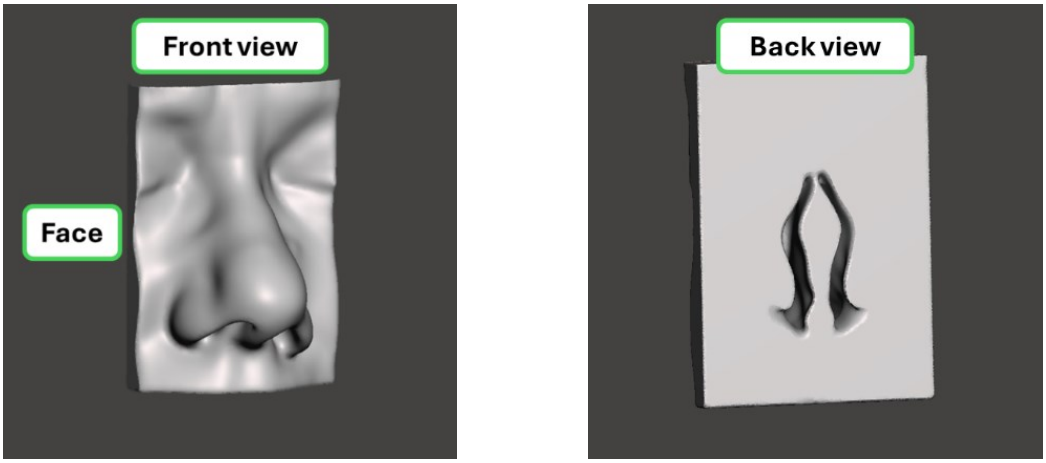

Fig. 2.3 Face model.

2.1.1 Selection of materials and processes

In order to better mimic the mechanical properties of each anatomical part of the model, research of the material typically used was conducted. The tissues of interest for the development of this ETA training model are the bone (i.e. the sphenoid bone), skin (i.e. the nose), the mucosa (turbinates), the arachnoid membrane and the pituitary tumor. The materials used have been selected on the basis of manufacturability. Since this is the first prototype of a model, materials that are easier to manufacture were considered.

The most interesting solutions found are listed in Table 2.1.

Table 2.1 List of the material and the production technology found to produce the different modules of the training model.

Tissue	Material	Production Technology	References
Bone	PLA	FFF/FDM	[165–169]
	PA[a]	SLS	[170–172]
	CAH	BJ	[173,174]
	3DPIC	BJ and Mold Casting	[175]
Skin	Silicone	Mold Casting	[176–178]
	Agar	-	[176]
	Gelatine	-	[176]
	Polyurethane	-	[176,179]
	PVA	-	[176]
Mucosa	Silicone	Mold Casting	[180]
Arachnoid	Polymeric film	-	[181,182]
Tumor	Resin[b]	-	[39,183]
	Boiled Egg	-	[80,184,185]
	Agar	Mold Casting	[186]

Abbreviation: FFF = Fused Filament Fabrication, FDM = Fused Deposition Modeling, SLA = Stereolithography, SLS = Selective Laser Sintering, BJ = Binder Jetting, CAH = Cyanoacrylate with hydroquinone, 3DPIC = 3D polymer-infiltrated composite, ST-504.
[a] = PA with glass beads;
[b] = Stratathane ST-504 Vari-Lok Injection Resin.

Bone – Sphenoid bone and ethmoid bone

To reproduce the sphenoid bone, it was chosen the PLA. Parts were fabricated by FFF technology on a Ultimaker 3 extended (Ultimaker, Netherlands), using the Pearl-white PLA by Ultimaker, whose main properties taken from its technical datasheet [187] are reported in Table 2.3 PLA was chosen over PA with glass beds [170-172] and ceramic materials [173-175] found in literature, which were more promising in terms of mimicking the mechanical properties of bone, because of its ease of manufacture for the production of this first prototype of the model.

Cartilage – Nasal Septum

The lower bending resistance of TPU makes it more suitable for reproducing the flexibility of cartilaginous tissues, as it was found in literature [188]. TPU has a lower flexural modulus and a higher resistance to strain compared to PLA, making TPU more suitable than PLA, for this application. Similarly, the nasal septum was fabricated to FFF technology on a Ultimaker 3 extended, using the TPU 95A, by Ultimaker, whose main properties taken from its datasheet [189] are reported in Table 2.3.

Skin and Mucosa – Nose and turbinates

Silicone was chosen to replicate both the Nose module and the turbinates module. In particular it was used the Dragon Skin™ 30 by Smooth-On, whose main properties are reported in Table 2.3 from its datasheet [190]. In particular, silicone modules were produced with the traditional mold casting technology, since the additive manufacturing process of two-component silicone is not a mature process yet [191]. The skin and mucosa silicone molds were fabricated using PLA print cores of the parts into which the silicone was poured. The fabrication of silicone components is described in the following sections.

Table 2.2 Mechanical properties of Pearl-White PLA and TPU 95A. XY, YZ and Z refer to the orientation of the specimen tested, X-Y is the printing plate, while Z is the printing direction. Data are taken from material datasheets [187,189,190].

Mechanical Property	Material	Value (Orientation)		
		(XY - Flat)	(YZ - Side)	(Z - Up)
Flexural modulus (MPa)	PLA	3019 ± 87	2894 ± 53	2740 ± 47
Flexural strain at break (%)		4.8 ± 0.2	NB	1.9 ± 0.2
Hardness (Shore D scale)		84		
Flexural modulus (MPa)	TPU 95A	62.6 ± 1.7	55.1 ± 2.4	62.6 ± 2.0
Flexural strain at break (%)		NB	NB	NB
Hardness (Shore D scale)		48		
Hardness (Shore A scale)	Silicone	30		
Pot life		45 minutes		
Curing time		16 Hours		

NB= No Break (> 10%)

Arachnoid and Tumor

In the first prototype of the model the dura mater was not added for the sake of simplicity. The arachnoid membrane was reproduced with the polymeric food film as found in literature [181,182], which was considered a good representation in our previous works [192]. The pituitary tumor, as it was found from our systematic review [7], was reproduced following an interesting group of training model, called “Egghead” [185], where the sellar region and its content were reproduced using an egg [75,80,184,185,193,194], in particular both the boiled yolk [185] and the boiled albumen [80,193] were used as a reproduction of the tumor. Together with experienced surgeon we evaluated that the boiled albumen is a good approximation and low-cost solution to mimic the mechanical properties the pituitary tumor [195,196].

Table 2.3 reports an overview of the selected materials and AM processes together with the tissues to be manufactured and hierarchy of the model (groups and modules) that will be further described.

Table 2.3 Module of the training model, the fabrication technologies and the materials used for their production.

Group	Module	Tissue	Process	AM		RC	Disp.
				Material	Technology	Material	
Face	Face	Skin	RC	PLA	FFF (Pattern)	Silicone	no
	Ethmoid bone	Cortical Bone	AM	PLA	FFF	-	no
	Nostril (core)	Cavity	RC	PLA	FFF (Core)	-	no
Nose	Nasal septum	Cartilage	AM	TPU 95A	FFF	-	yes
Nasal cavity	Turbinates	Mucosa	RC	PLA	FFF (Pattern)	Silicone	yes
	Frame	Non-anatomical	AM	PLA	FFF	-	no
Skull-base	Sphenoid bone	Cortical Bone	AM	PLA	FFF	-	yes
	Ethmoid bone	Cortical Bone	AM	PLA	FFF	-	no
	Arachnoid	Arachnoid membrane	-	Polymeric food film	-	-	yes
	Tumor	Pituitary adenoma	-	Egg white	-	-	yes

Abbreviations: AM = Additive Manufacturing, RC = Rapid Casting, Disp. = Disposable

2.1.1.1 Skull-base model

From the Skull-base model shown in Fig. 2.2, using at first the *Plane cut* function, three different components were obtained, as shown in Fig. 2.4: sphenoid bone and ethmoid bone (Fig. 2.4a) and nasal cavity (Fig. 2.4b).

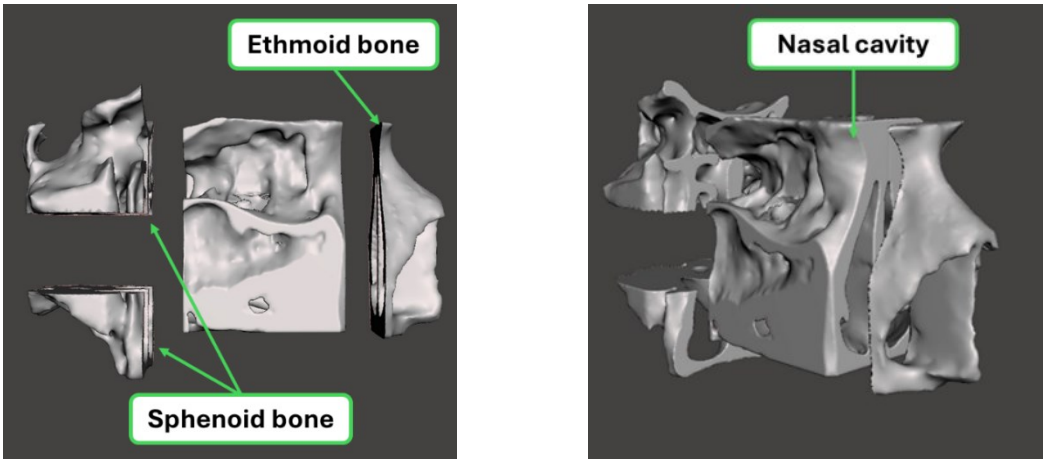

(a) (b)

Fig. 2.4 Modules obtained from the skull-base module. From the skull-base module were obtained the sphenoid bone module, the ethmoid bone module (a) and the nasal cavity module (b) with the *Plane Cut* function.

2.1.1.1.1 Sphenoid bone module

The sphenoid bone was cut into two halves with the *Plane Cut* function, as already anticipated in Fig. 2.4, the Upper sphenoid bone, and the Lower sphenoid bone. The first half, which contains the sella turcica, is the disposable part, which surgeons break during each simulation to expose the pituitary tumor, while the second, the lower sphenoid bone was kept as a support of the upper sphenoid bone. Using the *Boolean Union* function, two parallelepipeds with one hole each were incorporated into the model to mount to the frame with screws, as shown in Fig. 2.5. Additionally, the superior portion of the Upper sphenoid bone was cut and levigated.

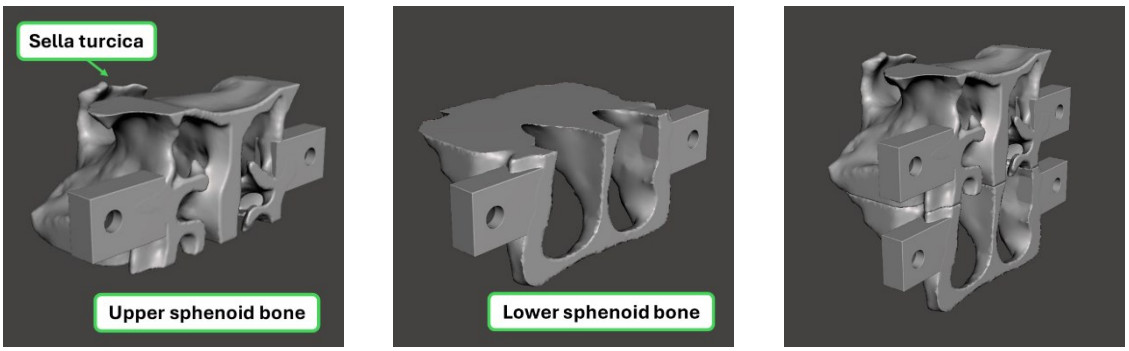

(a) (b) (c)

Fig. 2.5 Sphenoid bone module. Upper sphenoid bone with the sella turcica highlighted (a). Lower sphenoid bone (b) and the two modules combined (c). To the module, two parallelepipeds with one hole each were added to mount them on the frame module.

2.1.1.1.2 Ethmoid Bone module

The ethmoid bone was obtained with the *Plane Cut* function from the skull-base. The function of the ethmoid bone module is to provide rigidity to the nose, which is better described in the following section. Fig. 2.6 shows the ethmoid bone module.

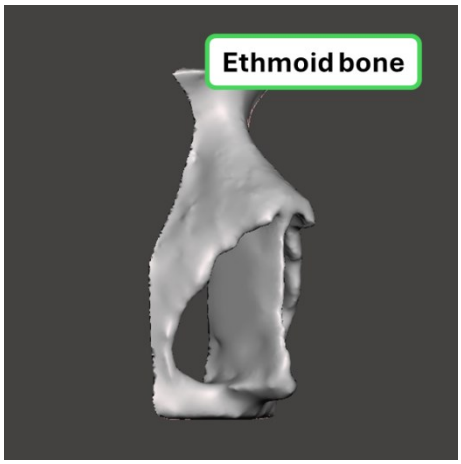

Fig. 2.6 Ethmoid bone module.

2.1.1.1.3 Nasal cavity model

Among each module here described, the nasal cavity model is the one which required more elaborations. From the model shown in Fig. 2.7 three modules of the training model were obtained: nasal septum (Fig. 2.7a), the turbinates (Fig. 2.7b) and the frame, which was designed around the nasal cavity module.

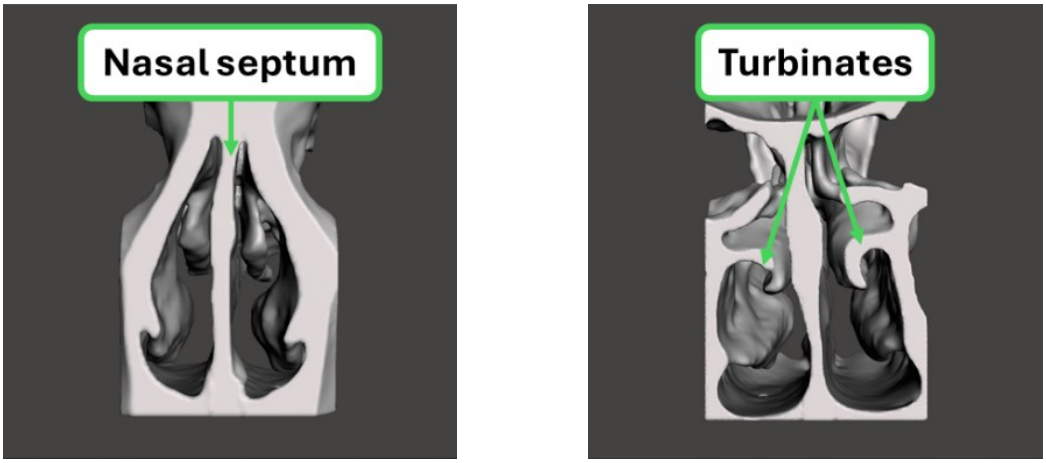

(a) (b)

Fig. 2.7 Nasal cavity models. From this model two anatomical modules were obtained: nasal septum (a) and turbinates (b). The non anatomical frame module was derived from this model.

Since the external parts of the nasal cavity module are not accessed during surgery, they were converted into a parallelepiped's shape, which is easier to fabricated, in a view of 3D printing. Therefore, the frame was designed accordingly. To the nasal cavity model, were added parallelepipeds externally to give the desired shape to the object. Then they were combined with the nasal cavity model into a single object using the *Combine* function. Fig. 2.8 shows the nasal cavity model surrounded by parallelepipeds.

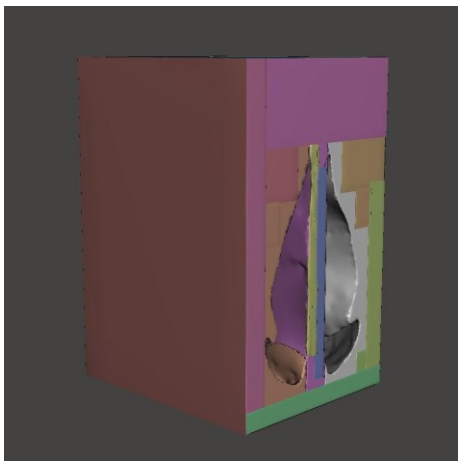

Fig. 2.8 Desing process of the frame module. Outside the nasal cavity model, several parallelepipeds were added to give it a more feasible shape in a view of 3D printing.

Subsequently, the newly constructed 3D model of the nasal cavities was modified using the *Make Solid* function to improve its suitability for the 3D printing stage. However, the new solid required further modifications to its mesh, in fact, several errors and inconsistencies in the mesh emerged both externally and internally, as shown in Fig. 2.9a and Fig. 2.9c. The model was smoothed outside using the *Plane Cut* function. By selecting the "Smoothing surface", i.e. the most internal surface among those generated from the *Make solid* functions, shown in Fig. 2.9a, Meshmixer automatically moves the plane to the selected surfaces. It is possible to delete anything outside by making the *Plane Cut* direction point outward from the model. The result of the manual smoothing process is shown in Fig. 2.9b. Additionally, some artifacts generated from the *Make Solid* function were manually deleted to restore the original aspect of the model. Then to eliminate the unimportant parts inside the model that would inexorably make more difficult the 3D printing phase, a window was opened from the external each of the surfaces. It was made to have a complete view inside the object. At this point, the unnecessary areas were deleted, the remaining cavities, to ensure a correct reconstruction by the software, were softened with the *Smooth Boundaries* function and where necessary, they were edited with the *Sculpt* tool. In this way, it was possible to obtain both internally and externally a homogeneous object free of uncertain edges that could have lowered the quality of the finished product once printed. Then the window was closed with *Inspector* function since the surface on which it is derived is planar. Fig. 2.9c and Fig. 2.9d shows the comparison respectively before and after the cleaning in an x-ray view mode of the model.

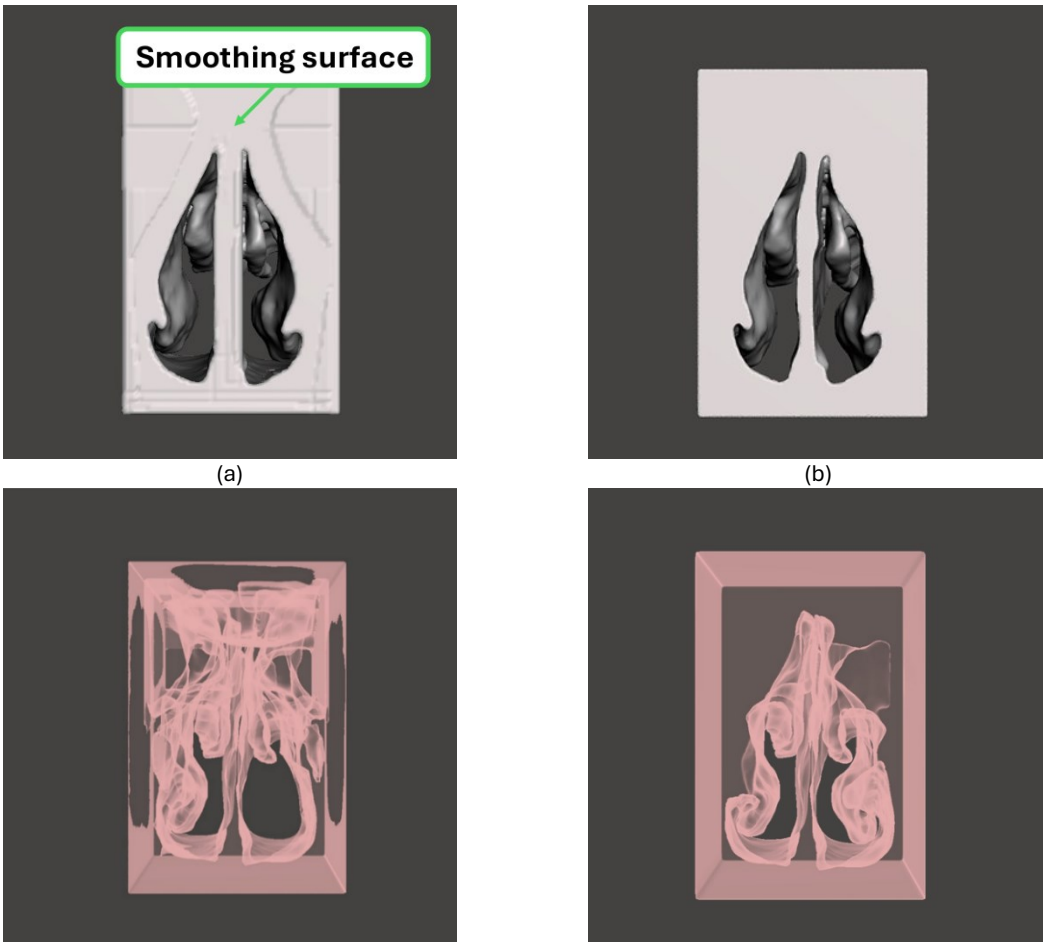

Fig. 2.9 Cleaning process of the nasal cavity model.

With a homogeneous and clean internal structure, the nasal cavity model was divided into three parts: the turbinates, the nasal septum and the remaining part, the frame.

2.1.1.1.4 Turbinates module

In sake of simplicity, only the inferior and middle turbinates were obtained from the edited nasal cavity model, using the *Plane Cut* function. Concerting the upper turbinates (both left and right) they were discarded since they were not faithfully reproduced in the Skull-base model. The turbinate modules were designed with a rectangular shape to facilitate the design phase, the fabrication, and the final assembly. In fact, having a flat rectangular surface was fundamental to facilitate the use of the *Boolean Difference* function from the nasal cavity model, in order to obtain the frame. In Fig. 2.10 are reported the two turbinates module, the left turbinate module, Fig. 2.10a and the right turbinate module Fig. 2.10b.

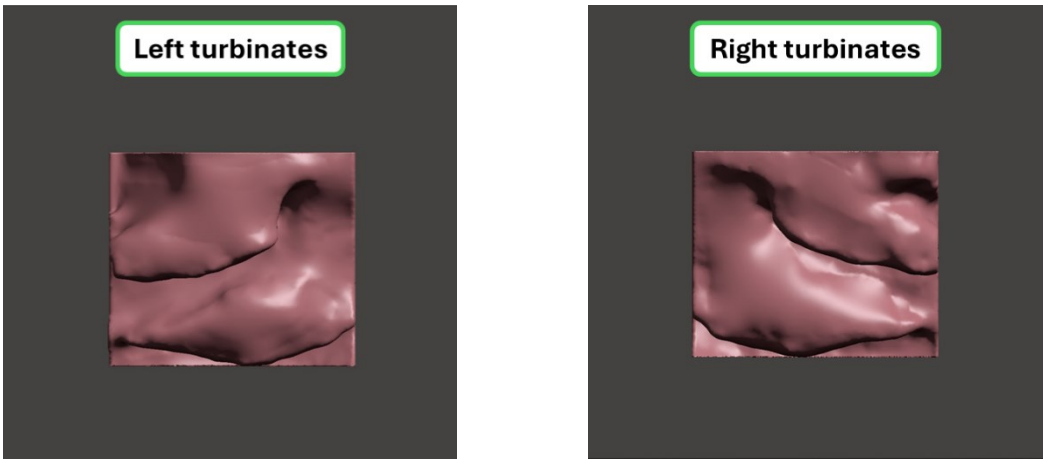

(a) (b)

Fig. 2.10 Turbinates modules. The lower and middle turbinate of both side of the nasal cavity, the left (a) and the right (b). The rectangular shape was given to facilitate not only their fabrication but also the fabrication of the frame module which is obtained with the *Boolean Subtraction* function from both the turbinates modules.

2.1.1.1.5 Nasal septum module

The nasal septum module was obtained using the *Plane Cut* function and it is shown in Fig. 2.10. The module reported here represents the part of the nasal septum within the nasal cavities, the other part remained for fabrication simplicity into the ethmoid bone module. The square-sectioned parts that can be observed on the top and on the bottom of the module reported in Fig. 2.11 were made not only to facilitate the fabrication of the module, but also its insertion into the frame module.

Fig. 2.11 Nasal septum module. The square-section parts on the top and on the bottom were made with *Plane Cut* function to facilitate the fabrication of the module and its insertion in the frame.

2.1.1.1.6 Frame module

This component, as already mentioned, was designed to be the support of the model, i.e. the base to which all the other modules would be connected to, with the respect of the ETA

anatomy. The frame was created starting from the nasal cavity model, by selecting the external surfaces of the object. Using the *Fit Primitive* function, it was possible to generate planes adjacent to the selected area, i.e. each surface of the parallelepiped. The new plane generated were extruded with the *Extrude* function and were then adjusted with *Plane Cut* functions. At this point, the frame was turned into a solid with a homogeneous mesh with the *Make Solid* function and then, with the *Boolean Difference* function the turbinates modules and the septum module were subtracted to allow their insertion once fabricated. To facilitate the insertion, the volume of the modules was expanded through the utilization of the *Transform* function, specifically the *Scale X*, *Scale Y*, and *Scale Z* commands with the *Uniform Scaling* option enabled. It was to guarantee the insertion of the modules within the frame, thus preventing the typical dimensional error that occurs during the 3D printing process. Then, two holes were made into the frame using the *Boolean Difference* function, to attach the nose module via plugs to the frame. Fig 2.12a shows the frame, while Fig. 2.12b shows the frame with the turbinates and nasal septum modules inserted.

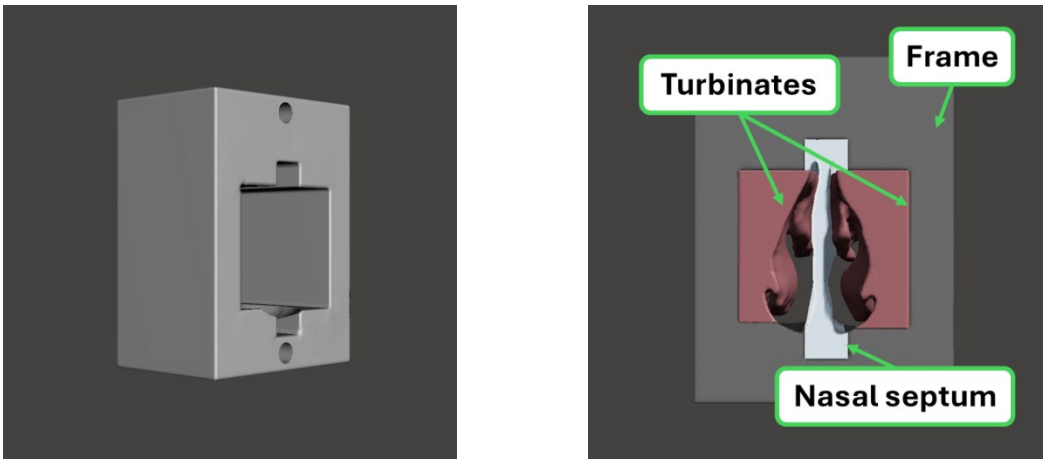

(a) (b)

Fig. 2.12 The frame module. The frame (a) and the frame with the turbinates and nasal septum module inserted (b).

2.1.1.2 Face model

From the face model shown in Fig. 2.3, were obtained the nose module and the nostrils core prints, used to guarantee in the silicone casting phase the reproduction of the nostril's cavities in the nose module.

2.1.1.2.1 Nose module

The nose module was obtained from the head of the patient and required minor modification from the base model shown previously in Fig. 2.1. Using *Plane Cut* function several times and then it was remeshed and smoothed respectively with Meshmixer functions

Remesh and *Smooth* to obtain a more homogeneous mesh. Finally, with the *Make solid* function the nose module was turned into a solid.

2.1.1.2.2 Nostrils core prints

The most challenging aspect was to ensure that the nostril cavities would have been maintained during the molding process. Since ETA starts with surgeons inserting instruments from the nose, reproducing adequately the nostril's cavity was fundamental to have a functional training model.

To guarantee that the nostril's cavity was not covered by silicone during casting, removable nostrils cores were then designed. Nostrils cores were obtained as the complementary of the cavity to reproduce. Using the *Select* instrument, the edge of each cavity was selected, and their boundaries were smoothed with *Smooth Boundaries* function to have a more manageable mesh. Then from the selected nostrils area a new group was generated using the *Create FaceGroup* function, from the *Modify* menu. The mesh outside the nostrils group was deleted, therefore what remained was the inside of the nostril. With the *Flip Normals* function in the *Edit* menu (which appears only after selecting an area of the object), it was possible to flip the mesh, thus inverting the direction of the normal of the triangles composing the mesh. Then the beginning and the end of the model have been closed with *Inspector* function. The nostrils cores obtained are reported in Fig. 2.13a. Furthermore, to guarantee a correct positioning of the cores in the mold, two core prints were designed by extruding the ends of the cores, with the *Extrude* function, in the *Edit* menu. Fig. 2.13b shows the nostril cores with the core prints added.

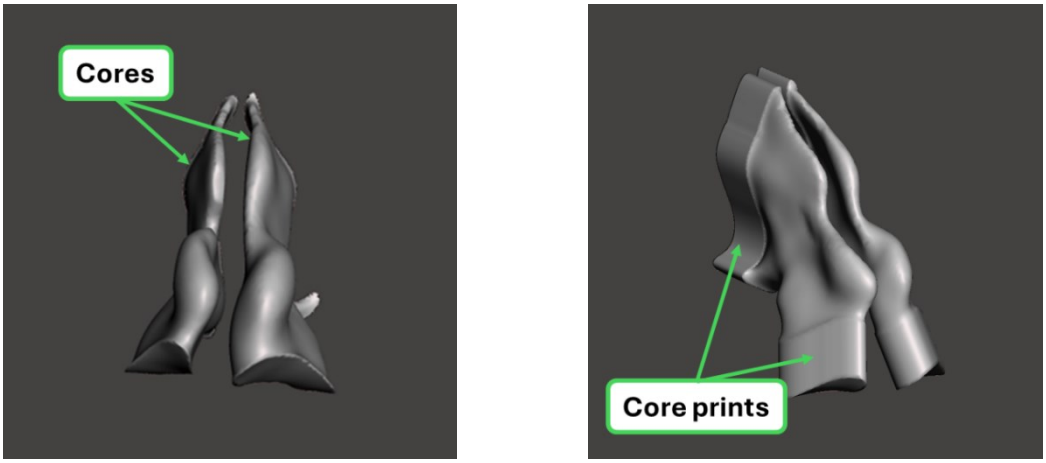

(a) (b)

Fig. 2.13 Nostrils print cores with core prints.

Silicone alone is not enough to correctly represent the mechanical properties of the nose, as it would not be able to guarantee its rigidity. For this reason, the ethmoid bone module has been inserted within the nose module. However, to properly fit within the nose module, the ethmoid bone also had to guarantee the removal of the nostril's cores once silicone cured. Using the *Boolean Difference* function, the interference between the ethmoid bone module and the nostril's cores objects were eliminated, thus allowing the insertion and removal of the nostrils from the ethmoid bone module. Fig. 2.14 shows the results of the ethmoid bone with the nostrils core fitted within.

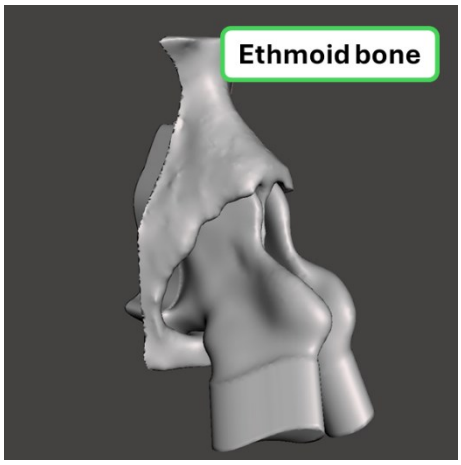

Fig. 2.14 Ethmoid bone with nostrils cores fitted within.

These modules have been combined using the *Combine* function first, and then the *Make Solid* function into a single model, the pattern model, which was then used to fabricate the silicone mold. Fig. 2.15 shows the pattern. In particular, Fig. 2.15a shows the front of the pattern model, while Fig. 2.15b shows the back. Additionally, in Fig. 2.15b it is possible to observe two holes added to the nose module using *Boolean Difference* function with a cylinder. Their function is to allow the connection of the model with plugs to the frame module.

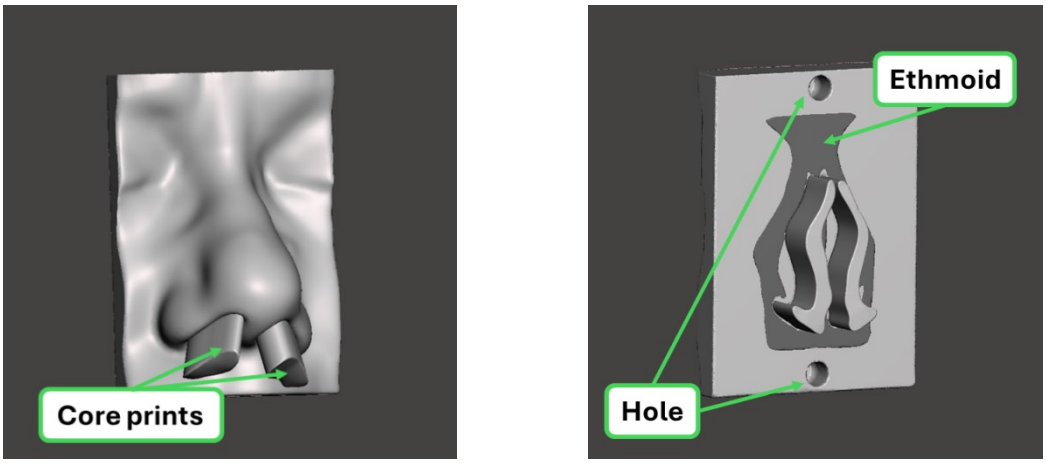

(a) (b)

Fig. 2.15 Pattern for the nose mold. Nose module with the core prints and the ethmoid bone inserted within. Two holes were added to allow the connection of the nose module to the frame module.

2.2 Results and Discussion

2.2.1 3D printing

Each of the components described was 3D printed with PLA on a Ultimaker 3 extended (Ultimaker, Netherlands) using Pearl-White PLA filament with a diameter of 2.85 mm, using the AA04 nozzle. The printing parameters used are the default parameters suggested by Cura, the software for 3D printing developed by Ultimaker. The nasal septum module was 3D printed in TPU, which, as already described, was found in literature to be to be a better alternative for mimicking the consistency of cartilage [188].

In Fig. 2.16 are reported each module printed. The nose pattern, Fig. 2.16a, the left and right turbinates, Fig. 2.16b and Fig. 2.16c, the Frame, Fig. 2.16d, the upper and lower sphenoid bone Fig. 2.16e and Fig. 2.16f and the nasal septum in TPU Fig. 2.16g.

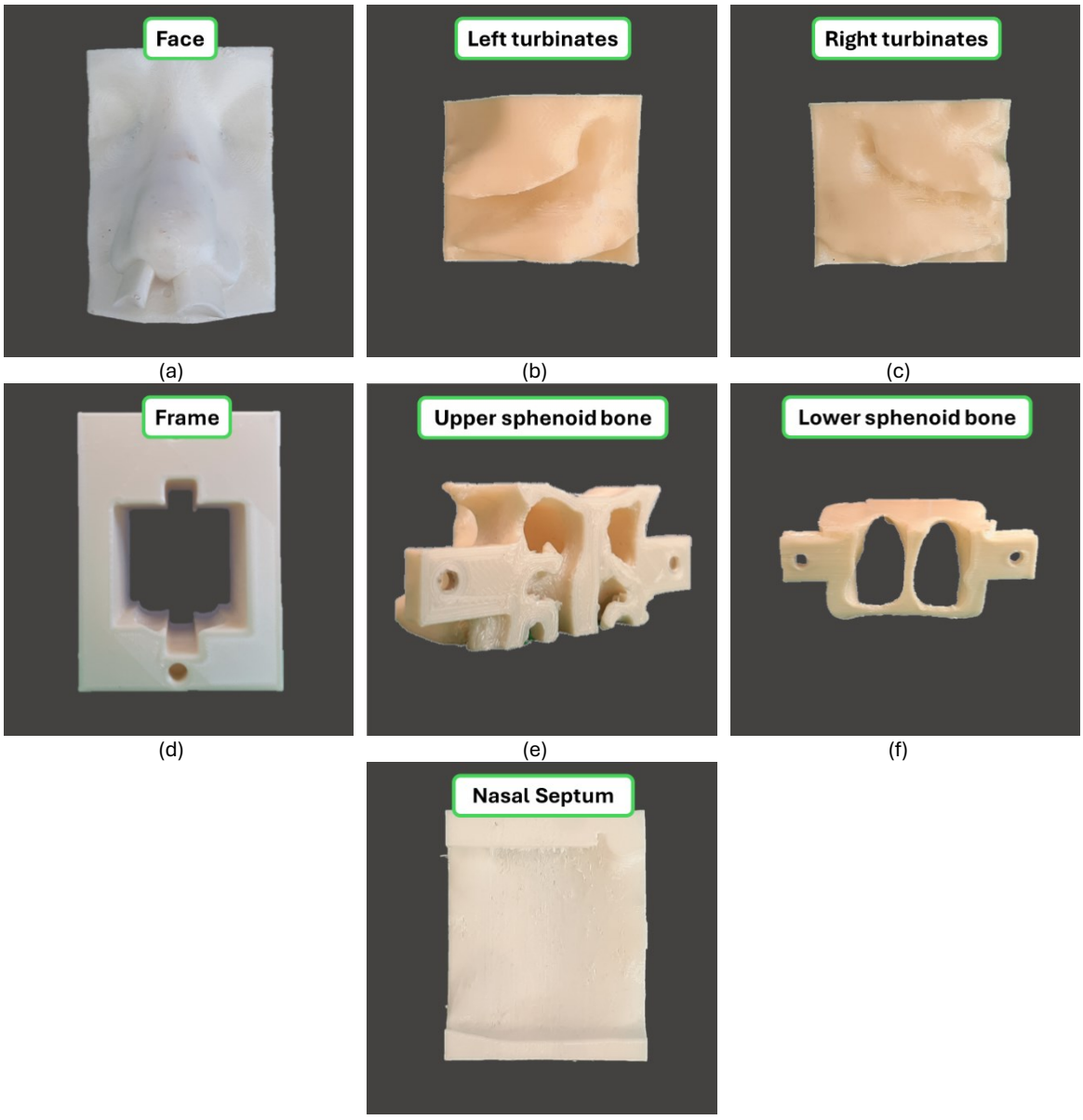

Fig. 2.16 3D printed modules. The nose pattern (a), the left and right turbinates (b) and (c), the Frame (d), the upper and lower sphenoid bone (e) and (f) and the nasal septum in TPU (g).

2.2.2 Fabrication of silicone molds

The choice of using silicone as a material for the molds was made because, thanks to its flexibility, it is possible to overcome the problems related to the extraction of the most complicated pieces and those with many undercuts. For the manufacturing of the molds, “MoldStar™ 15 SLOW” was chosen, a silicone produced by Smooth-On (Smooth-On, Inc., USA), which is suitable to produce molds. The silicone in question has an attested hardness of 15 on the Shore A scale. The “MoldStar™ 15 SLOW” offers a wide pot-life interval of 50 minutes, or the time within which the two components begin to cross-link, and the silicone

starts to cure. Having a wide interval of time for the preparation of the silicone before it hardens means having more time to be able to prepare the material. After mixing the two components, A and B, in a 1:1 ratio the silicone was subsequently degassed inside a vacuum pump, until no more bubbles emerged on the surface.

The production of silicone molds started placing the object to reproduce in a box large enough to leave at least 10 millimeters of thickness of the mold, as indicated by the manufacturers of the material. Then it was covered halfway with a special sulfur-free clay. By blocking the object with the clay, it is ensured that it does not move during the pouring of the liquid silicone. Before pouring the silicone, two screws were placed on the outer edge, to ensure its positioning. Once the clay was arranged, the silicone chosen for the mold was poured. Before pouring silicone, a vacuum pump was used to degas the silicone. The pump reached a pressure of -90 kPa and 15 minutes of degassing were sufficient to ensure complete removal of air bubbles from the silicone before casting.

Once cross-linked, the clay was removed and after adding a pouring channel and one or more holes to ensure the escape of air, the mold silicone was poured to obtain the last part of the mold. Before casting the silicone again, however, as suggested by Smooth-On, the first half-mold was coated with a layer of Ease Release™ 205 release agent to facilitate the separation of the two halves of the mold without damaging them. When the second half of the silicone has also hardened, the mold is opened and the initial object, the casting channel and the air vents are removed.

Ther silicone used for the fabrication of the components was the two-component silicone Dragon Skin™ 30 by Smooth-On (Smooth-On, Inc., USA). It has a Shore 00 scale hardness of 30, softer than the silicone used for the molds. This silicone was chosen because its hardness is close to the one of the mucosa and the skin. Furthermore, it has a wide pot-life interval, which as previously described, guarantees a higher quality of the casting, giving the possibility of degassing it. In addition, this silicone was selected because it is transparent and therefore easily colorable, in fact, together with the silicone, special-colored pigments “Light Flesh” pigment of the Silc Pig™ by Smooth-On. As previously mentioned, the two components A and B were combined in a 1:1 ratio. Together with component A, the colorant was added, a small amount of it is sufficient to give a vivid color to the finished part. Also in this case, before casting, a layer of release agent Ease Release™ 205 was placed, to facilitate the removal of the finished pieces, preventing breakage and at the same time preserving the integrity of the mold.

Fig. 2.17 describes the procedure followed for the fabrication of the silicon parts of the model. First of all, cores and possible inserts are initially printed (Fig. 2.17a). The silicone used for the molds is prepared and degassed to remove air entrapped during pouring and mixing

(Fig. 2.17b). Then, the pattern with landmarks is temporarily fixed on a clay substrate inside a box and a releasing agent is applied on the surfaces that will be in contact with silicone (Fig. 2.17c) during the pouring of the first half of the mold (Fig. 2.17d). Once the silicone is cured, the clay is removed. The half mold and pattern are turned upside-down, lateral embankment and pattern of the pouring channel (made of clay) are added and, finally, the release agent is applied (Fig. 2.17e). The second half mold is then poured on the first one (Fig. 2.17f). After solidification, the pattern is removed, core and inserts are positioned, vents may be cut on the parting plane (if required), and the releasing agent is applied (Fig. 2.17g) to obtain the mold (Fig. 2.17h). To cast the part, silicone is prepared, degassed (Fig. 2.17i) and poured (Fig. 2.17j). If vents are used, the mold should be tilted to facilitate the air release. Once solidified, the core is removed from the part and the pouring channel is cut (Fig. 2.17k) to obtain the final part (Fig. 2.17l).

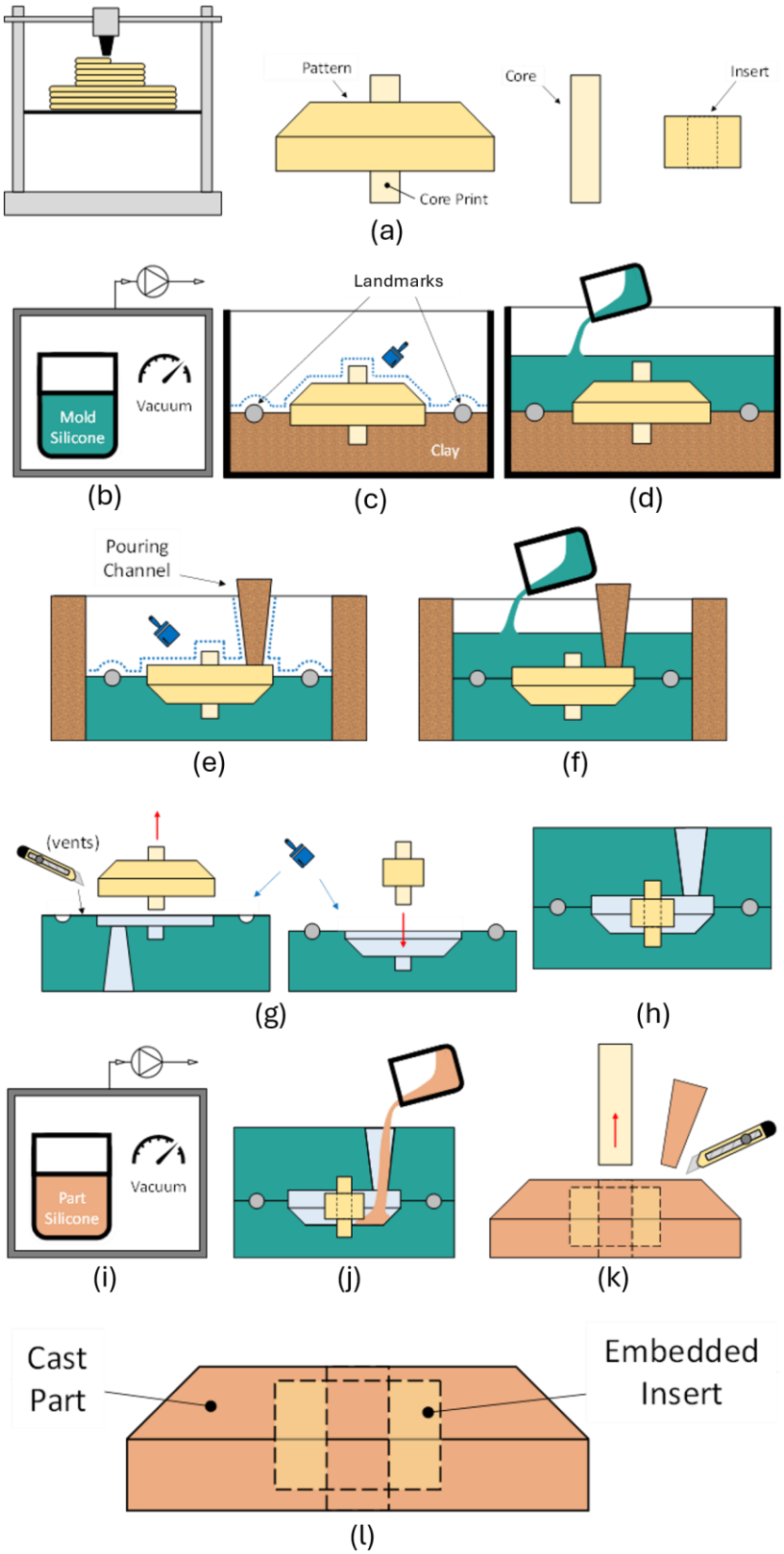

Fig. 2.17 Procedure of the Rapid Casting of silicone parts.

2.2.2.1 Face mold

Fig. 2.18 shows the steps of fabrication of the “Face mold”. Fig. 2.18a shows the preparation of the first half of the mold with the positioning of the nose module inside on a clay base and with two positioning screws. Then the preparation of the second half of the mold is shown in Fig. 2.18b where the ethmoid module and the nostrils print cores are inserted into the first half, to give rigidity to the nose and to guarantee the reproduction of the nostrils cavity. Fig. 2.18c and Fig. 2.18d show the two halves of the mold for the fabrication of the nose module of the training model.

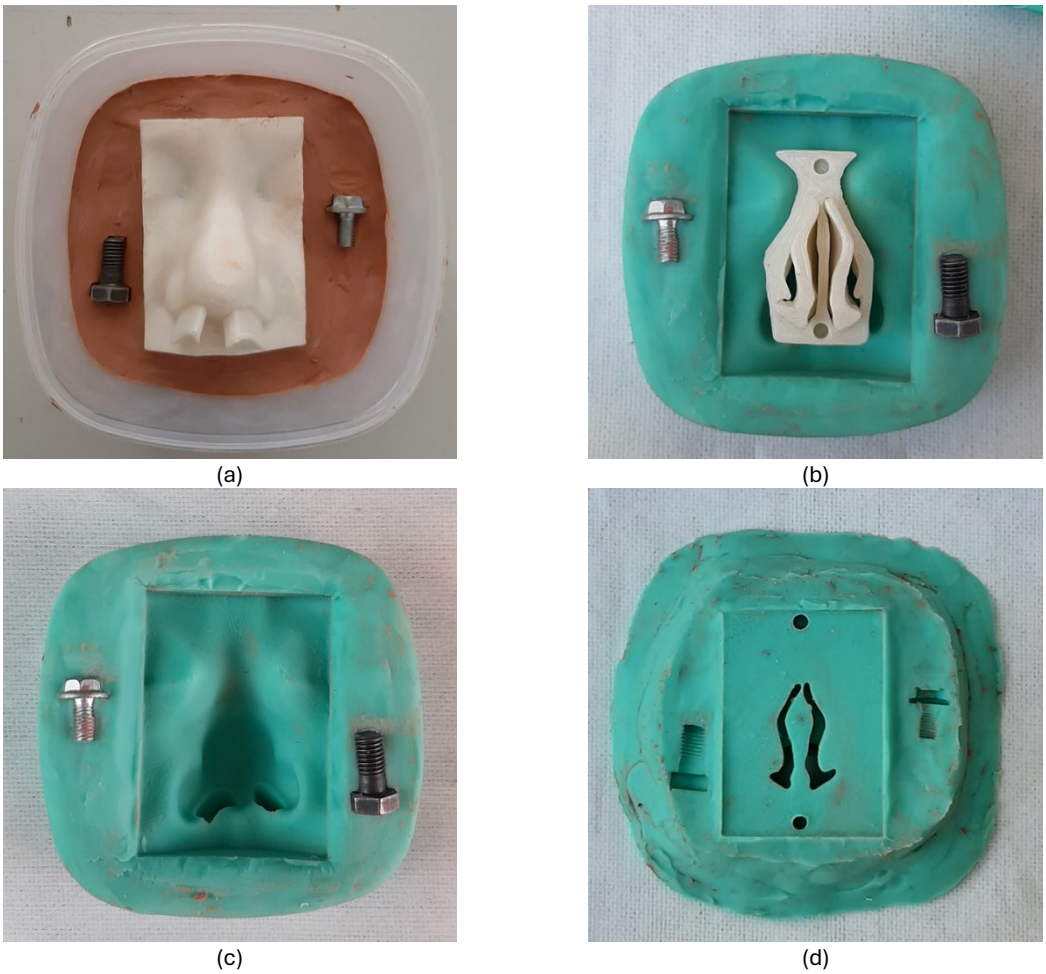

(a) (b)

(c) (d)

Fig. 2.18 Steps of fabrication of the nose mold. Preparation of the first half of the mold with the positioning of the nose module inside on a clay base and with two positioning screws (a). The preparation of the second half of the mold where the ethmoid module and the nostrils print cored are inserted into the first half (b). The two halves of the mold for the fabrication of the nose module (c) and (d).

2.2.2.2 Turbinates mold

Fig. 2.19 shows the steps of fabrication of the Turbinates mold. Fig. 2.19a shows the turbinates placed into the plastic box and held in place by the clay. Fig. 2.19b and Fig. 2.19c show the two halves of the mold.

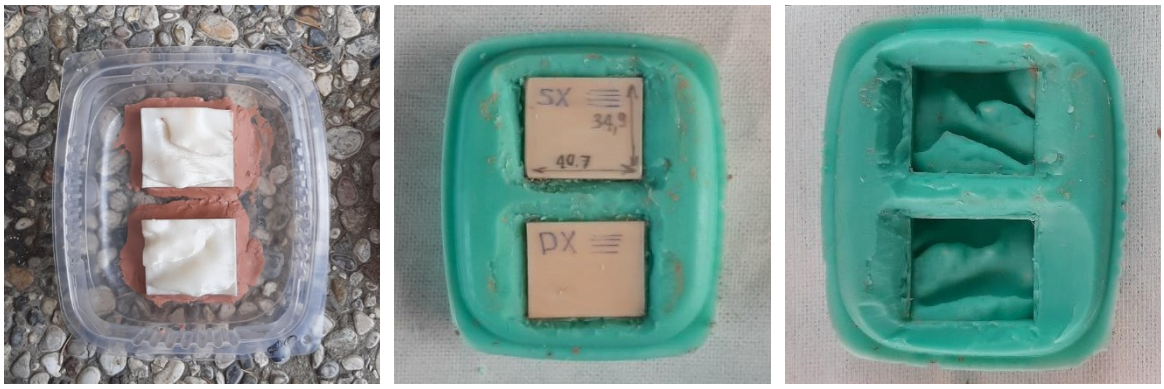

(a) (b) (c)

Fig. 2.19 Steps of fabrication of the Turbinates mold. The turbinates are placed into the plastic box and held in place by the clay (a). The two halves of the mold (b) and (c).

2.2.2.3 Silicone parts

Once the molds were cured, the silicone of the parts was poured into the molds. As already mentioned, before casting the parts, the two halves of each mold were coated with a layer of Ease Release™ 205 release agent by Smooth-On to facilitate the extraction of the parts once the silicone was cured.

2.2.2.3.1 Nose module

Fig. 2.19 shows a comparison between the CAD module of the nose (Fig. 2.19a) and the nose module once extracted from the mold (Fig. 2.19b).

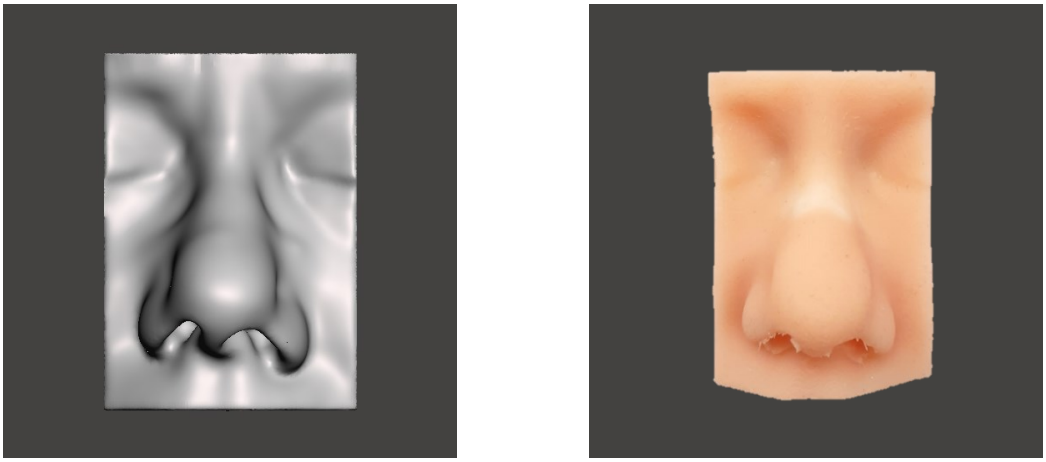

(a) (b)

Fig. 2.19 Comparison of the nose module. CAD model (a) and once extracted from the mold (b).

2.2.2.3.2 Turbinates module

Similarly, Fig. 2.20 shows comparison between the CAD module of the turbinates left turbinates and the right turbinates, Fig. 2.20a and Fig. 2.20c respectively compared to the left

and right turbinates module, Fig. 2.20b and Fig. 2.20d respectively, once extracted from the mold.

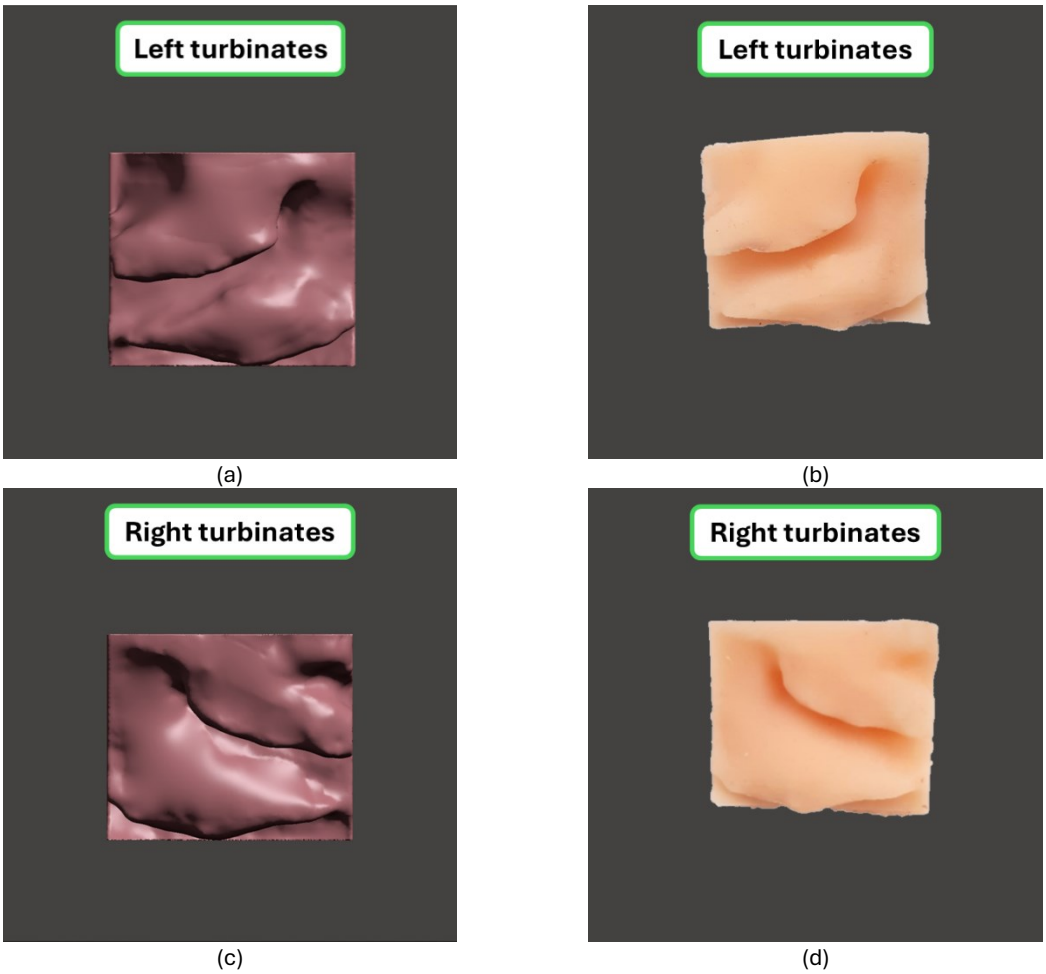

Fig. 2.20 Comparison of the turbinates modules. CAD model of the left turbinate (a) and the right turbinate (c). Left turbinates (b) and right turbinates (d) modules once extracted from the mold.

2.2.3 Training model mounted

The CT-based training model was assembled as shown in Fig. 2.21 where is reported a comparison between the CAD model (Fig. 2.21a, Fig. 2.21b, and Fig. 2.21c) with the model once mounted (Fig. 2.21d, Fig. 2.21e and Fig. 2.21f). In particular Fig. 2.21a and Fig. 2.21d show the inside of the model where the turbinates and the nasal septum modules are mounted.

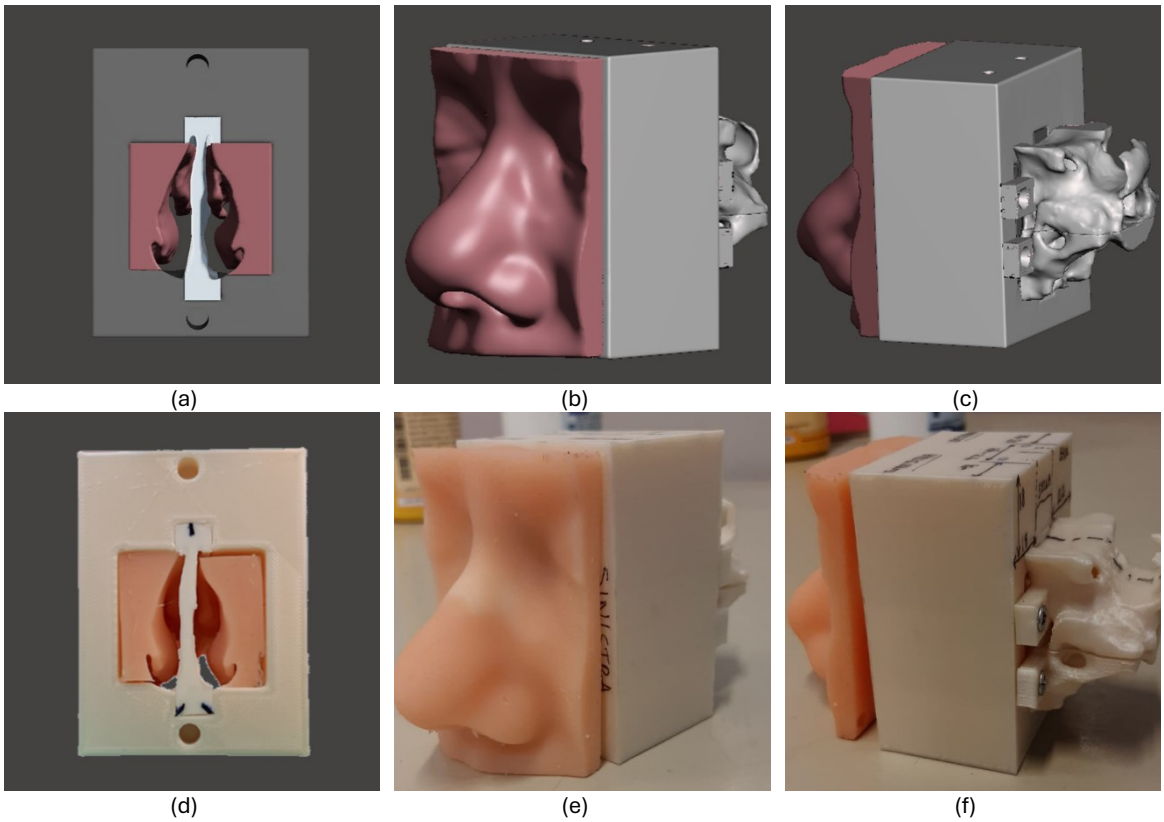

Fig. 2.21 The CT-based anatomical training model. CAD model (a), (b) and (c), and the CT-based model mounted (d), (e) and (f).

2.2.4 Preliminary validation

The training model was tested by an expert neurosurgeon who provided a preliminary validation and feedback on the quality of the training model, using real surgical instruments like the endoscope and the spatula a navigation was performed through the training model as shown in Fig. 2.22. In Fig. 2.22a it is possible to observe the endoscopic view of the left side of the nasal cavity. Fig. 2.22b shows a frame of a simulation of the dissection of the sphenoid bone to expose the sellar region and the pituitary tumor. From a first endoscopic inspection, it appeared that the anatomy of the patient is well reproduced even if the thickness of the sphenoid bone resulted slightly higher. The flexural strength of both the TPU for the nasal septum and the silicone for the mucosa is close to the real one, even if the elastic return of silicone is too high.

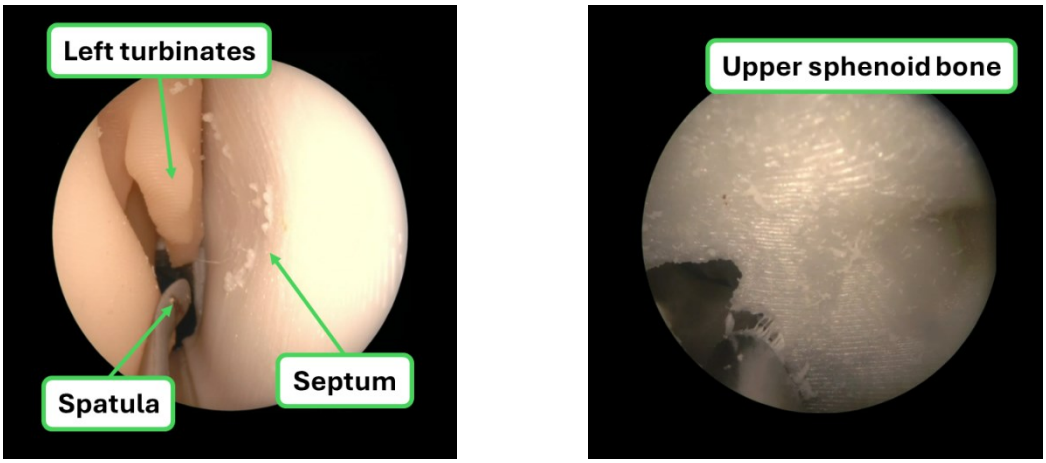

(a) (b)

Fig. 2.22 Endoscopic view of the training model. The nasal cavity (a) and the sphenoid bone (b).

Furthermore, two mechanical tests were performed to validate the material that compose the model, one is the dissection of the sphenoid bone as already anticipated, while the other is a particular maneuver performed sometimes by surgeons that consist in breaking the final part of the nasal septum to make space within the nasal cavities. From those tests emerged the main problem of the thermal resistance of PLA. PLA powders produced during the drilling phase, dissolved, and formed agglomerates that glued to the sphenoid bone module. In fact, from the PLA technical datasheet of Ultimaker [187] it is stated that it has a glass transition temperature of 59°C, which means that above this temperature its mechanical behavior changes drastically, so to overcome the problem of powder agglomerates formation, the temperature during drilling should be kept below 59°C by moistening bone surfaces with water. However, for the future version of the training model, research will be conducted in implementing ceramic materials (such as those listed in Table 2.1), which have more similar mechanical and thermal properties to the sphenoid bone. Fig. 2.23a shows the upper sphenoid bone dissected to expose the sellar region. Concerning the septum, even if it had a great flexural strength, its thickness was too high and together with an elevated resilience of the material it was difficult to cut as performed during the surgery, Fig. 2.23b shows the septum dissected.

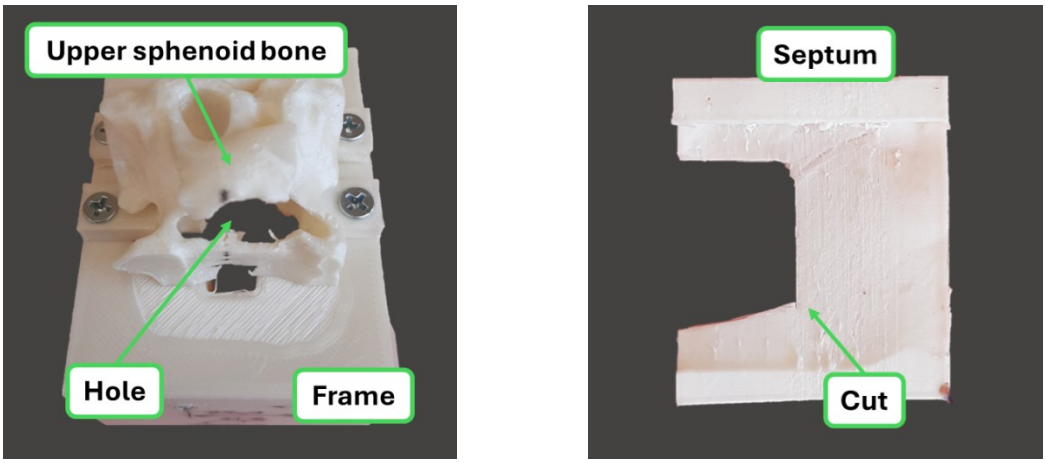

(a) (b)

Fig. 2.23 The validation of the training model. The Upper sphenoid bone dissected (a) and the nasal septum dissected (b).

2.3 Conclusions

In this chapter are reported the steps followed for the fabrication of a modular training model. The development of the training model started from a CT-data of a patient which was converted into an STL model. With Meshmixer, it was possible to obtain two base models: the skull-base and the face. From the skull-base after were obtained the sphenoid bone module (upper and lower), the nasal septum module, the turbinates module (left and right), the ethmoid bone and the frame, which is a non-anatomical addition to the training model designed as a basis for its assembly. From the face model were obtained the nose module, and the nostrils print core, which were used to guarantee the fabrication of the nostril's cavities. The modules were fabricated with the FFF technology, one of the most common AM technologies. Each module was fabricated a Ultimaker 3 Extended in PLA, except for the nasal septum, which was fabricated in TPU which, according to literature, and thanks to its lower flexural modulus, better mimics the mechanical properties of the cartilage. Since this was a first prototype of a model, the first choice was materials that were easier to manufacture, which is why PLA was preferred to the ceramic composites found in the literature, which will be the subject of future studies for a future model for surgical training. The nose and turbinates modules required another step for their fabrication. In fact, to better mimic the skin (nose module) and the mucosa (turbinates module) it was decided to fabricate them in by casting silicone into silicone molds. Using silicone molds allowed easier extraction of the components from the mold. The PLA printed modules of the nose, and the turbinates were used as a pattern to shape silicone molds, which then was poured another silicone to reproduce the mechanical properties of the skin and the mucosa.

Finally, the model was finally validated by an experienced neurosurgeon who provided feedback. From a first endoscopic inspection, it appeared that the anatomy of the model is well reproduced, however the thickness of the sphenoid bone resulted slightly higher. The flexural strength of both the TPU for the nasal septum and the silicone for the mucosa is close to the real one, but the elastic return of silicone was found to be too high. A problem that emerged from testing with surgical instruments is the thermal resistance of PLA. In fact, PLA powders produced during the drilling of the sphenoid bone dissolved and formed agglomerates that glued to the sphenoid bone module. Concerning the septum, even if it had a great flexural strength, its thickness was too high and together with an elevated resilience of the material it was difficult to cut as performed during the surgery. Future studies will focus on the addition of ceramic materials to mimic bone, which, according to the results of the review, promise better results. In addition, the use of a more drillable material to replace TPU would be preferable. In addition, the next prototypes of the model will focus on the suggested aspects. The introduction of other anatomical details that can raise the train complexity (as the presence optic nerves or the carotid artery) will be considered. Moreover, a bleeding system will be introduced to provide a more vivid and realistic experience.

Chapter 3

Development of a sensor-based system to reproduce the fall of the arachnoid

3.1 Introduction

This chapter presents the first aim of the thesis: the development, fabrication and characterization of a sensor-based system that reproduces the fall of the arachnoid membrane and can evaluate the force exerted on it. The system consists of a tank sealed on one side with a polymeric food film to mimic the arachnoid membrane. The tank is filled with distilled water to mimic the cerebrospinal fluid; the pressure of the distilled water is measured with a pressure sensor connected through a PVC tube to the tank, and it measures the variation of pressure of the liquid when a force is exerted on the polymeric film. In this way it is possible to obtain information on the level of force exerted on the membrane.

This chapter is comprised of two parts. The first part, section 3.2.2, is entitled "Prototype 1 - Concept" and it presents a concept prototype of the sensor-based system designed to mimic the arachnoid membrane. The second part, section 3.2.3, is entitled "Prototype 2 – Sensor-based Tank" describes the final product with a more anatomical design, which fits to the previously described model.

The first part describes the initial prototype. The concept prototype consists of a jar filled with distilled water, with a screw cap on, where a 30 mm hole has been drilled. The polymeric film is positioned between the jar and the cap. The system was characterized with laboratory tests, using a load cell to find a correlation between the applied force and the variation of pressure. The results obtained were promising regarding the functioning of the system, but the low repeatability between one test and another, when the polymeric food film was changed, represented a significant problem, covered in the second part presented in this chapter.

The second part describes the final version of the sensor-based tank, which was tested by experienced surgeons. The final version of the tank was designed to specifically fit the anatomy of the patient, so to be easily installed on the training model described in Chapter 2. The tank was designed to fit the upper sphenoid bone module so that the polymeric film fits

within the sella turcica. It consisted of different modules, each of them 3D printed in ABS on a Stratasys Dimension 1200es, except the gasket to guarantee the sealing, which was 3D printed in TPU on a Ultimaker 3 extended. The training model described in Chapter 2 was equipped with the sensor-based tank and was tested by experienced surgeons, in order to find a threshold above which the force exerted on the arachnoid membrane could tear it, exposing the patient to cerebrospinal fluid leakage. The threshold identified is comparable to the level of force exerted in the literature when interacting with soft tissue during a transsphenoidal surgical approach. Furthermore, the innovative features of the model received constructive feedback from surgeons, which demonstrated the functionality of the system and its potential as a valuable tool for evaluating surgeons' skills before entering the operating room.

3.2 The ETA sensor-based training model

3.2.1 The Electronic Setup

The electronic setup used to collect data was the same for both the "Concept prototype" and the "ETA training model prototype", which was derived from a previous one that was suitable for our purposes. The only difference is the pressure sensor used. Initially, for the first prototype it was used a pressure sensor 24PC15SMT by Honeywell (Honeywell, USA) with an operating range from 0 to 15 PSI (103,421 kPa) and, according to its datasheet has a 0.2 mV (0.092 kPa) of repeatability and hysteresis. During the experimental campaign of the ETA training model prototype, it was decided from the data collected with first prototype, to use a pressure sensor 24PCEFA6D by Honeywell with a lower operating range from 0 to 0.5 PSI (3.447 kPa) and a repeatability and hysteresis of 0.5 mV (0.05 kPa). The pressure sensor measures the variation of pressure of the distilled water inside the jar when an indenter presses the film. The indenter is connected to a computer controlled micrometric slide. With the provided software it is possible to control how the slide moves, as well as its speed and acceleration. The minimum displacement that can be imposed on the slide is 0.010 mm, this value was considered as its resolution. A load cell is also used to provide feedback on the applied force and to correlate this data to the fluid pressure. Before starting the experiments, a static characterization of the load cell was carried out to obtain its calibration curve. This resulted linear ($R^2 > 0.99$) with a sensitivity of 4.4 N/mV. The sensor signal is conditioned by a custom electronic module for Wheatstone Bridges at 10 V. A PL330DP power supply by Thurlby Thandar (Thurlby Thandar Instruments Ltd, UK) with dual output with independently adjustable channels. Data from both sensors were elaborated by a conditioning electronic

circuit, the output signals were collected with an HP34401 multimeter (Hewlett-Packard, USA) for each sensor, with a resolution of 6 ½ digits, which, compared to the acquisition boards, have superior metrological characteristics. Furthermore, the two multimeters are linked to the PC via the same GPIB-USB-HS interface, allowing for the simultaneous collection of both sensor signals. This facilitates the immediate correlation of data from the load cell to the pressure sensor. The PC is then interfaced with a LabVIEW program (National Instruments, USA) using 2 Hz as a sampling rate. Data were then analyzed on specifically designed MATLAB (MathWorks, USA) programs. Table 3.1 provides a summary of the electronic setup used and the main specifications of the instruments.

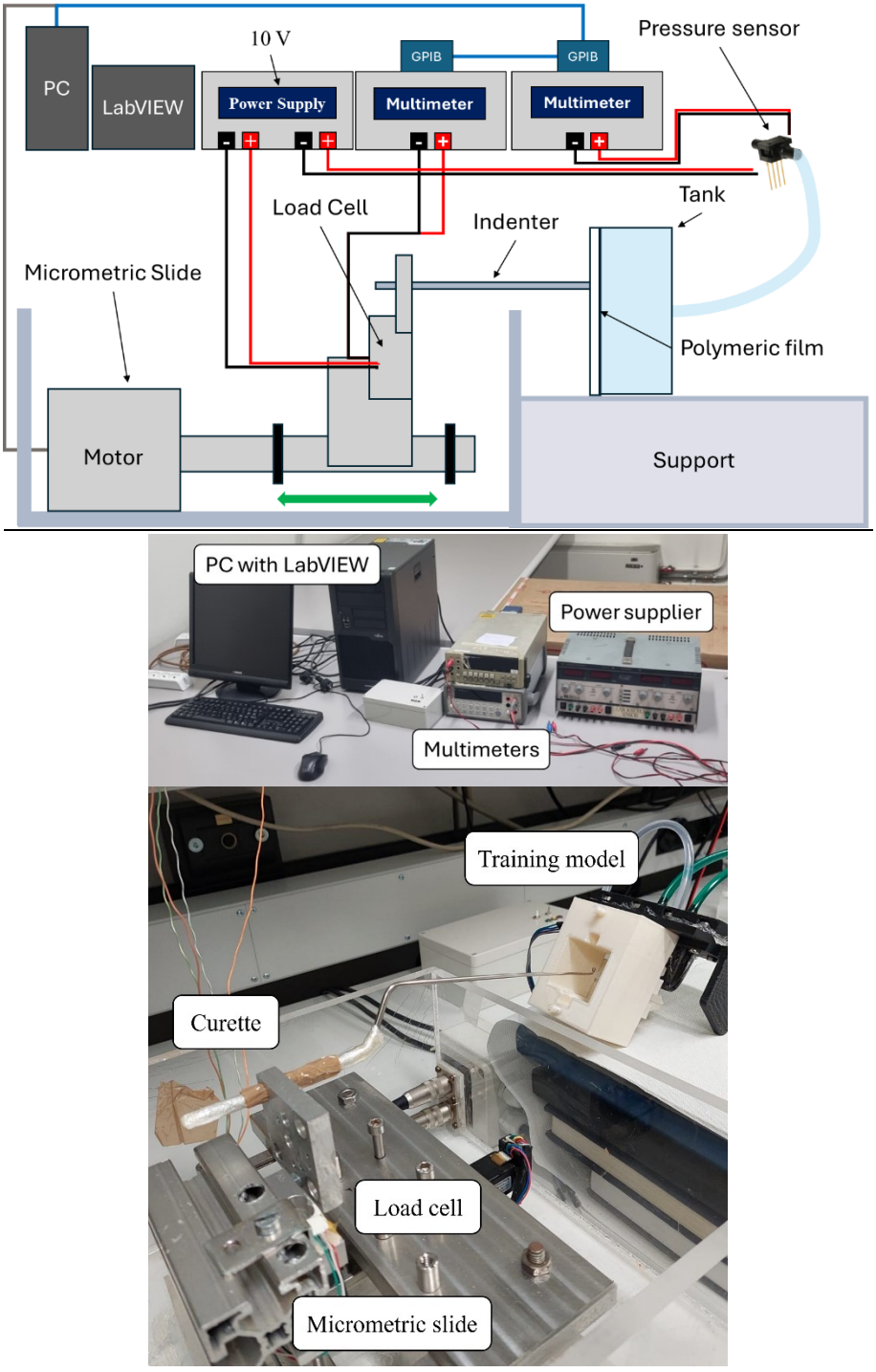

Fig. 3.1 The electronic setup. An indenter is moved by a micrometric slide with a load cell embedded. The indenter presses the membrane of the tank, and the imposed stress causes an increase in the inner pressure of the tank, which is read by the pressure sensor connected to it. Data are then collected by a LabVIEW program and analyzed with the MATLAB software. Both the load cell and the pressure sensor are alimented at 10 V by the power supply.

Table 3.1 Summary of the electronic setup used.

Component	Model	Main Specifications	Use	Notes
Power supply	PL330DP	Dual output with independently adjustable channels	To power both the load cell and the pressure sensor at 10 V	-
Multimeter 1	HP 34401A	Resolution: 6½ digits	To read the load cell data	-
Multimeter 2	HP 34401A	Resolution: 6½ digits	To read the pressure sensor data	-
Micrometric Slide	-	Resolution: 0.010mm	To move the indenter (curette)	-
Load Cell	-	Sensitivity: 4.4 N/mV	To measure contact force	-
Pressure Sensor	24PC15SMT	Operating range: 0 - 103,421 kPa, Repeatability and Hysteresis: 0.092 kPa	To measure the variation of the distilled water	Used for testing with the first prototype
Pressure Sensor	24PCEFA6D	Operating range: 0 –3.447 kPa Repeatability and Hysteresis: 0.05 kPa	To measure the variation of the distilled water	Used for testing with the second prototype
GPIB-USB-HS interface	-	-	To allow simultaneous collection of both sensors data	-
LabVIEW	-	Sampling rate: 2 Hz	To obtain data during tests	-
MATLAB	-	-	To analyze data	-

The following section is adapted from the conference paper entitled “Preliminary study of a sensorized system for real-time feedback for arachnoid collapse during neurosurgical training” published in “2023 IEEE International Workshop on Metrology for Industry 4.0 & IoT (MetroInd4.0&IoT) in July 2023” [7].

3.2.2 Prototype 1 - Concept

3.2.2.1 Materials and methods

3.2.2.1.1 Experimental Setup Description

The concept prototype developed to mimic the arachnoid collapse, consists of a jar filled with distilled water, with a screw cap on, in which a 30 mm hole has been cut. An additional hole was made in the jar to connect a pressure sensor to the system with a silicone tube. A piece of Domopak food film (Cuki Cofresco S.r.l., Italy) was used to mimic the arachnoid external membrane and was placed between the jar and the cap so that when the jar is closed, the film comes out. For this preliminary study, the arachnoid trabeculae were not reproduced. Since the cerebrospinal fluid (CSF) is made of 99% of water, and it has a viscosity that is slightly different from pure water [197] it was reproduced with distilled water, which, for this application is similar to what found in literature where in other training models it was mimicked using saline solution [198,50,49,48,51]. Fig. 3.2 shows the hereby described experimental set-up.

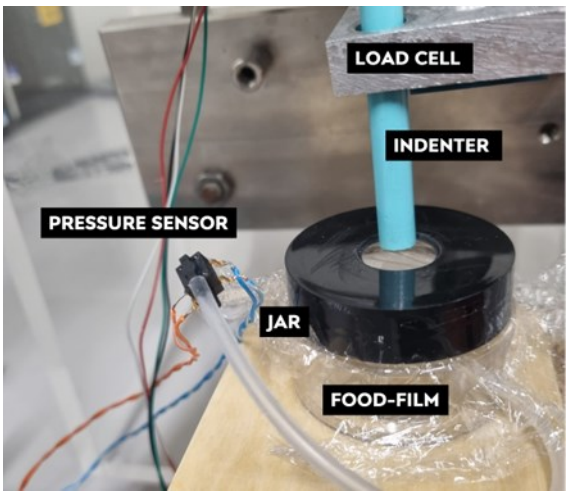

Fig. 3.2. The experimental set up ready. The pressure sensor is connected to the jar via a silicone tube. The indenter is connected to a micrometric slide on which a load cell is mounted.

3.2.2.1.2 Experimental Protocol Description

Two tests were designed to explore the response of the polymeric film to an external load through an indentation cycle. After the first test the polymeric film was changed in order to exclude the influence of any residual deformation that could impact on the results of the following test. Prior to the start of both indentation cycles, an initial pause was made in an unloaded state, to measure the offset of the load cell and the pressure sensor. Then the slide was slowly moved with steps of 0.20 mm until the load cell detected a variation of force. In this way it was possible to determine when the interpreter came into contact with the film. Once finished the preparation, the designed loading cycles started. For the first test a continuous load cycle was performed. The slide was programmed to descend 0.25 mm, from 0 up to 3.0 mm of depth into the polymeric film with a 5 s break after each step. Then, after a 30 s delay the process was inverted and the slide rises of 0.25 mm in 5 s intervals back to the starting position. As second test (stepping load test), the indenter was programmed to perform a series of fourteen alternating descents and ascents with, with the slide movement going from 0 to 7.0 mm in 0.5 mm. After any descents and ascents, a delay of 30 s was performed. Lastly, after the last unloading cycle, a continuous descent was imposed to the slide till the polymeric film broke in order to measure its resistance. The force measured during the tests is comparable to the results of the studies conducted by Bekeny et al. [199], where a load cell was mounted on a curette during a pituitary tumor resection through ETA surgery. And although the lift of the arachnoid membrane is not mentioned, it is reasonable to assume that the force required is similar to the values registered for soft tissues, with a mean value that ranges from 0.1 to 0.5 N.

3.2.2.2 Characterization of the first prototype

Three different graphs are presented for both tests. The first shows a plot of the Load Cell (N) and the Pressure Sensor (kPa) as a function of Time (s), to show the loading-unloading cycle. The second is a diagram of the Pressure Sensor (kPa) vs. the Load Cell (N) where data are divided from “Load” to “Unload”. Lastly, the third graph shows the Load Cell (N) and the Pressure Sensor (kPa) as a function of the Displacement (mm), i.e. the distance set to the slide. The values of the corresponding force and pressure in this graph are chosen at the peak of each descent. During both tests, no water losses were detected.

3.2.2.2.1 Continuous Loading Tests

Fig. 3.3 shows data measured by the load cell and the pressure sensor as a function of time. From the graph emerges a clear correlation between the Load Cell and the Pressure Sensors, especially from t = 50 s. Before that time the pressure sensors value registered are

below its repeatability of 0.092 kPa. Moreover, both sensors present a progressive decrease of their output that is observed during the delay between loading and unloading phase. This effect is related to the viscoelastic nature of the polymer. In fact, when the slide is stationary, the indenter applies a constant strain on the polymer film that generates a stress relaxation phenomenon. The correlation between these two physical entities is shown in Fig. 3.4. From the plot emerges that there is a hysteresis phenomenon, underlining a difference of the output measured during the loading and the unloading phase. The hysteresis phenomenon is related to the limit of the pressure sensors. Beside the point at 1.6 N during the loading phase, both cycles show a linear trend. In fact, the coefficient of determination during the loading cycle (LC) resulted R^2 = 0.98 and the RMSE = 0.050 based on a sample size of 97, while during the unloading cycle (UC), the linear model resulted R^2 > 0.99, with an RMSE of 0.016 and a sample size of 116, thus suggesting a linear correlation. The displacement graph in Fig. 3.5 shows an initial non-linear correlation (below 1.5 kPa) that converges towards a better linear correlation at higher pressures , data were interpolated using a 2nd degree linear model, the first degree term was removed as it had a p-value greater than 0.05. The RMSE of load cell data (F) is 0.038, while for pressure sensor data (P) the RMSE is 0.024. For both model, the R^2 obtained is > 0.99 and the sample size is 12.

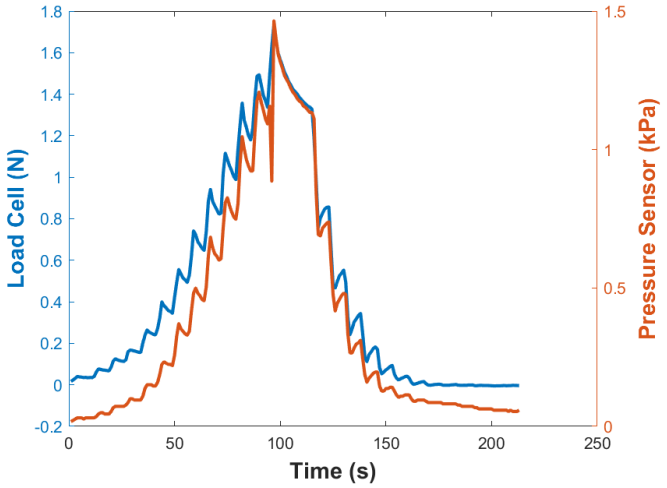

Fig. 3.3 Load Cell (N) and Pressure Sensor (kPa) reported as a function of Time (s) for the first test: load-unload cycle of 12 progressive movements of the slide, from 0 to 3 mm depth.

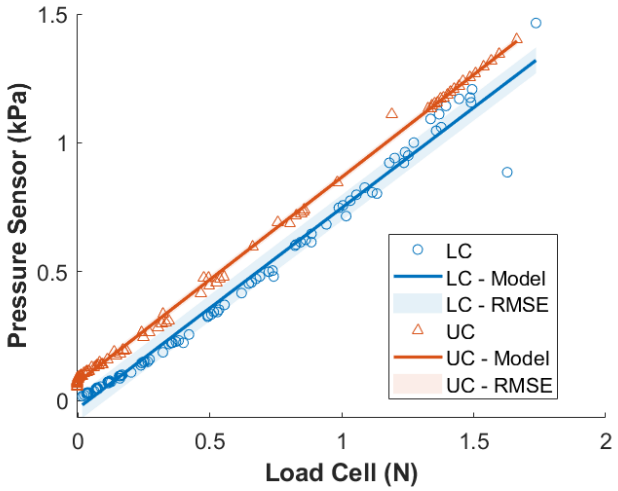

Fig. 3.4. Pressure Sensor (kPa) vs. Load Cell (N), the blue curve represents the loading phase, while the orange represents the unloading phase. The presence of a hysteresis loop is clear. the coefficient of determination during the loading cycle (LC) resulted $R^2 = 0.98$, an RMSE of 0.050 and a sample size of 97, while during the unloading cycle (UC), the linear model resulted $R^2 > 0.99$, with an RMSE of 0.0162 and a sample size of 116, thus suggesting a linear correlation for both curves.

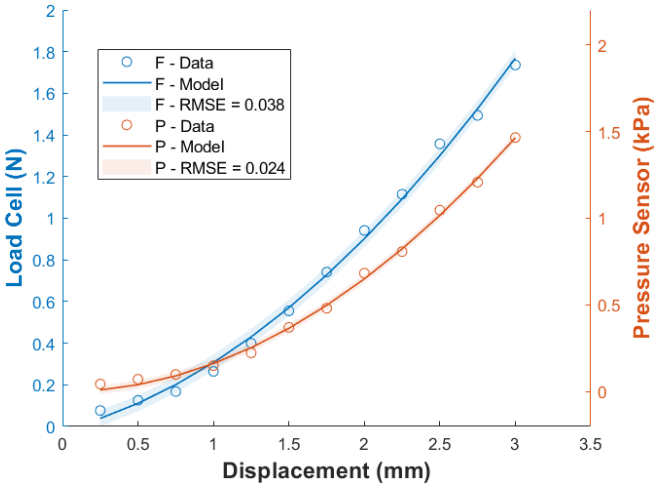

Fig. 3.5 Load Cell (N) and Pressure Sensor (kPa) as a function of the displacement (mm) during the loading phase. The first part of the pressure sensor curve (below 1.5 kPa) is non-linear. Data were interpolated using a 2nd degree linear model, the RMSE of load cell data (F) is 0.038, while for pressure sensor data (P) the RMSE is 0.024. For both model, the R^2 is > 0.99 and the sample size is 12.

3.2.2.2.2 Stepping Load Test

Fig. 3.6 reports the loading cycle and the obtained pressures on the fluid. As shown in the previous test, the correspondence between the two values is clear after the sixth loading/unloading cycle since before it the pressure measured is below the repeatability of the sensor. The effect of stress relaxation is evident immediately after each loading phase, as seen in the previous test. In Fig. 3.7 is reported the Pressure Sensor (kPa) vs. the Load Cell (N) of only the thirteenth cycle is reported to better understand the different behavior of the

polymeric film between the loading phase and the unloading phase, and it was evaluated as the standard deviation of the values in the range between 0 and 0.5 N, common to all replicates. In Fig. 3.8a are reported the even-numbered test cycles from the sixth through the fourteenth plus the one to failure. Furthermore, a linear interpolation of data, for the common points among each loading cycle curve (excluding the first five, as these were below the repeatability of the sensor) during the loading cycle of these tests, was made. Additionally, data below 0.1 N were cut, in accordance with the results obtained by Bekeny et al. [199] where the minimum force reported on soft tissue was 0.1 N. Data were then interpolated with a second-degree polynomial. The R^2 is 0.90 while the RMSE is 0.028 for a total of 199 samples (Fig. 3.8b). The graph shows that the shape of each repetition is similar, even though it presents hysteresis, as already noted in the previous test. In addition, for force values greater than 1 N, the slope of the load cycle, including the failure, tends to be linear, with an R^2 = 0.99 and an RMSE of 0.067 based on a sample size of 230 points. In fact, below 1.5 N of the load cell, the corresponding pressure sensor data are close to 0.092 kPa, the repeatability of the sensor, which affects the measures. Regarding the unloading cycle, it has a linear slope for force value with an R^2 = 0.93 and an RMSE of 0.075 based on a sample size of 291 points. Fig. 3.9 shows the displacement plot which shows a linear trend for the load cell (F), from a 1st degree linear interpolation, it resulted an RMSE of 0.10 and an R^2 of 0.99, while data from the pressure sensor (P) were interpolated using a 2nd degree linear regression, the first degree term was removed as it had a p-value greater than 0.05. It resulted an RMSE of 0.080 and an R^2 of 0.99. The sample size for each model is 14.

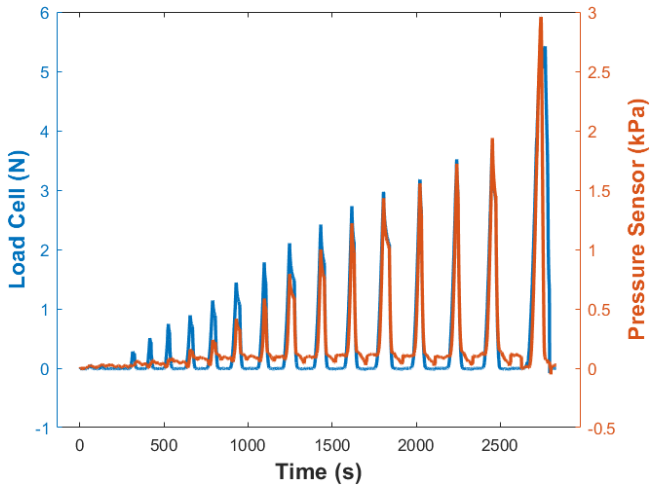

Fig. 3.6 Load Cell (N) and Pressure Sensor (kPa) reported as a function of Time (s) for the second test. A stepping load test from 0 to 7 mm depth plus the final rupture of the polymeric film.

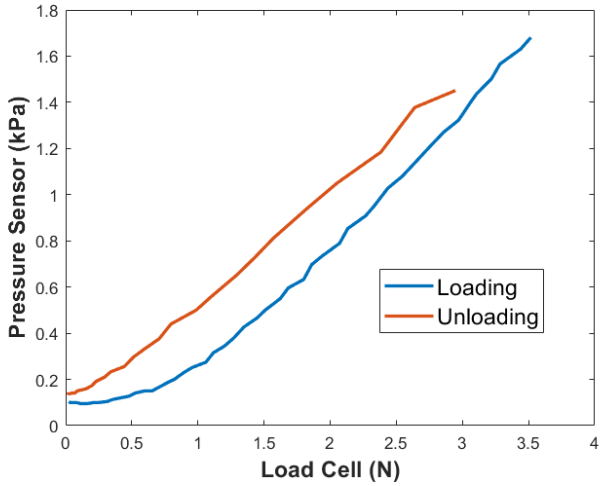

Fig. 3.7 Pressure Sensors (kPa) vs Load Cell (N) example of the second test. The lower part is the loading phase while the upper and more linear one is the unloading phase. The measurement uncertainty of the sensor is 0.092 kPa.

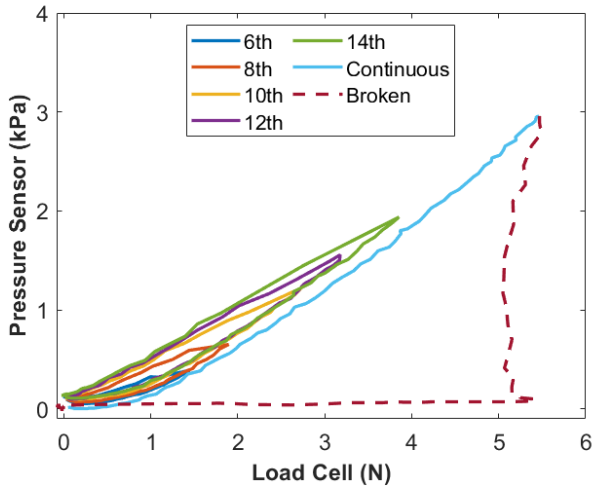

(a)

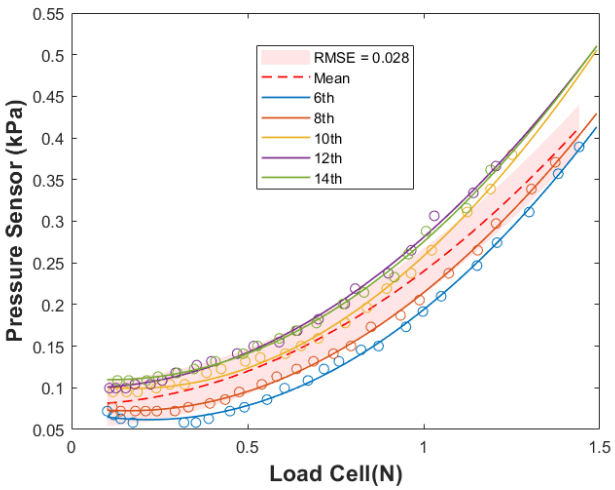

(b)

Fig. 3.8 Pressure Sensors (kPa) vs Load Cell (N) for the second test. Data show a clear hysteresis phenomenon. The “Continuous” and “Broken” curves show the last cycle where the film was broken by the indenter (a).

Furthermore, it was determined that the standard deviation for the common points among each loading cycle curve (excluding the first five, as these were below the repeatability of the sensor) during the loading cycle of these tests. Each curve was then interpolated with a second-degree polynomial. The R^2 is 0.90 and the RMSE is 0.028 with a sample size of 199 kPa (b).

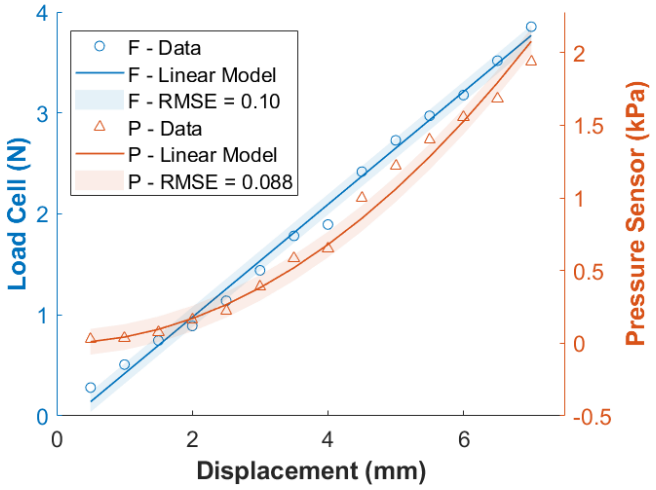

Fig. 3.9 Load Cell (F) and Pressure Sensor (P) as a function of the displacement during the loading phase. Data from the Load Cell (F) were interpolated using a 1st degree linear regression, it resulted an RMSE of 0.10 and an R^2 of 0.99, while data from the pressure sensor (P) were interpolated using a 2nd degree linear regression, the it resulted an RMSE of 0.080 and an R^2 of 0.99. The sample size for each model is 14.

3.2.2.2.3 Test Comparison

By comparing the tests emerges a limited repeatability between similar applied loads that can be observed in Fig. 3.10. The initial condition of the film changes between tests, and this can cause the indenter's descent resistance to vary, which explains the low repeatability that emerges when comparing the two curves, both for the load cell data, reported (Fig.3.11a) and especially for the pressure sensor in (Fig. 3.11b). To improve the signal, it is planned to change the pressure sensor to one with a lower full scale. In addition, the low values measured by the pressure sensor could be due to pressure losses in the experimental setup. The force measured are higher than those found in literature for soft tissue during an EETA surgery, because it is strictly linked to the non-anatomical design of the system where the food film is stretched. However, the repeatability evaluated during a load-unload cycle is high, meaning that this is a promising system capable of providing real-time feedback on the levels of force applied to the polymeric film.

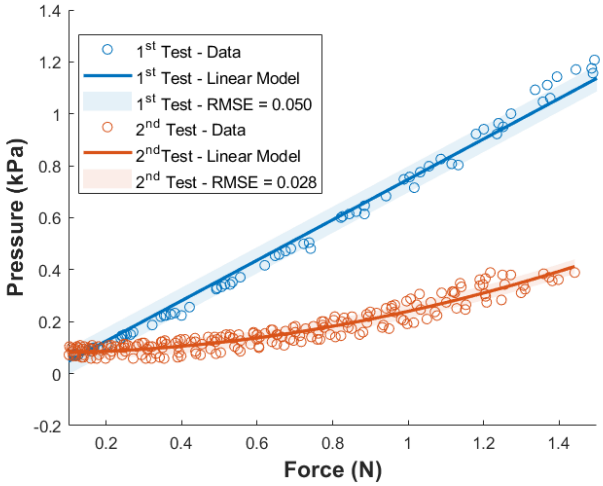

Fig. 3.10 Pressure Sensor (kPa) vs. Load Cell (N) of both tests (Loading cycle only). For the same applied force, the pressure increases faster in the first test.

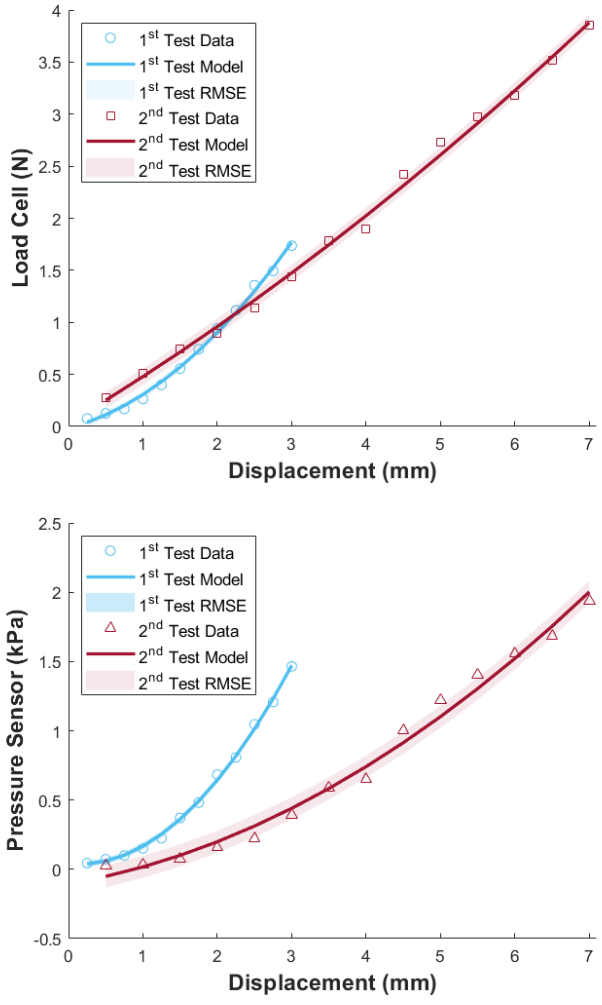

Fig. 3.11 (a) Load Cell (N) and (b) Pressure Sensor (kPa) as a function of the Displacement (mm) during the loading phase, a comparison between the two tests. The initial condition of the film changes between tests, and this can cause the indenter's descent resistance to vary, which explains the low repeatability that emerges when comparing the two curves, both for the load cell data, reported (Fig.3.11a) and especially for the pressure sensor in (Fig. 3.11b).

The following section is adapted from the paper entitled “3D printed training model with sensorized arachnoid for endoscopic transsphenoidal surgery: development and initial validation”, submitted to Heliyon in March 2023.

3.2.3 Prototype 2 – Sensor-based Tank

3.2.3.1. Materials and Methods

3.2.3.1.1 Sensorized tank module

The second prototype is designed to be mounted on the training model described in Chapter 2. In particular it is screwed to the frame module of the training model presented in Chapter 2 (Fig.3.12).

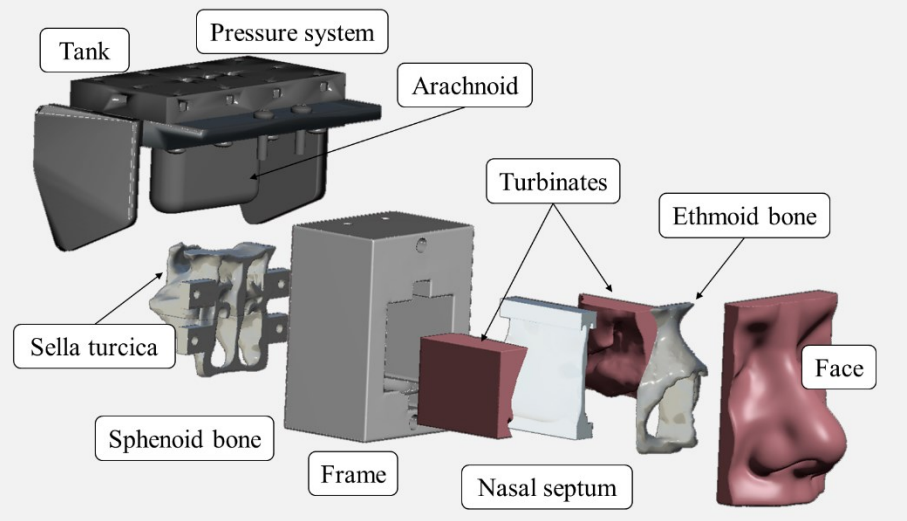

Fig. 3.12 Exploded view of the CT-based anatomical model.

In Fig. 3.13a is reported an exploded view of the system where each of its components are shown: the baseplate, the two columns, the polymeric film, the gasket, the sealing plate, and the pressure sensor, while Figure 3.13b and Figure 3.13c show the CAD of the assembled system and the printed and assembled system ready for testing, respectively. The polymeric film is folded onto the U-shaped structure formed by the baseplate and the columns to shape to ensure sealing. The two lateral supports were added to hold the training model at an angle of about 30 degrees, as in a real ETA [200]. The sensor is connected to the sealing plate with a PVC tube to one of the lateral supports, which is held by the two clips, to hold the sensor at a constant height during tests. Finally, two additional tubes were added to insert the liquid and let the air out (Fig. 3.13c).

The tank was printed in ABS on a Stratasys Dimension 1200es (Stratasys, Inc., USA), except for the TPU gasket, which was printed on an Ultimaker 3 Extended. Indeed, the mechanical properties of TPU make it a more suitable material for use as a gasket. Additionally, the two columns were covered with shrinkable thermoplastic strips to prevent the polymeric film from tearing by friction. Furthermore, to improve the airtightness of the sealing plate, it was painted with three layers of liquid rubber.

The pressure sensor integrated into the sealing plate between the two tubes measures the variation of the differential pressure between inside and outside the tank. When a force is applied to the membrane, a deformation of the membrane itself is generated, and a variation in the pressure difference can be measured. As already mentioned, from the results obtained with the first prototype, it was decided to use a different pressure sensor, the 24PCEFA6D by Honeywell (Honeywell International, Inc. USA), which has a lower full-scale value of 3.447 kPa, a sensitivity of 0.100 kPa/mV and ± 0.050 kPa of repeatability and hysteresis.

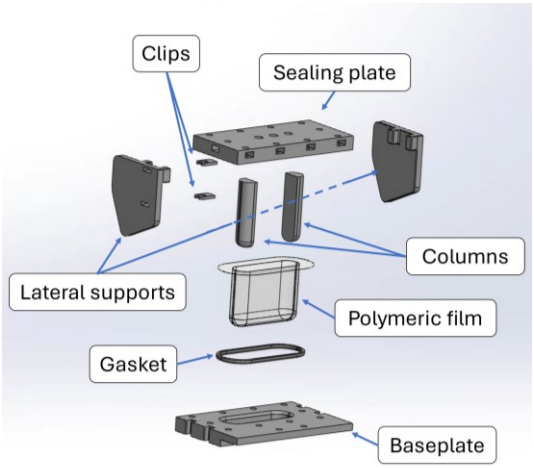

(a)

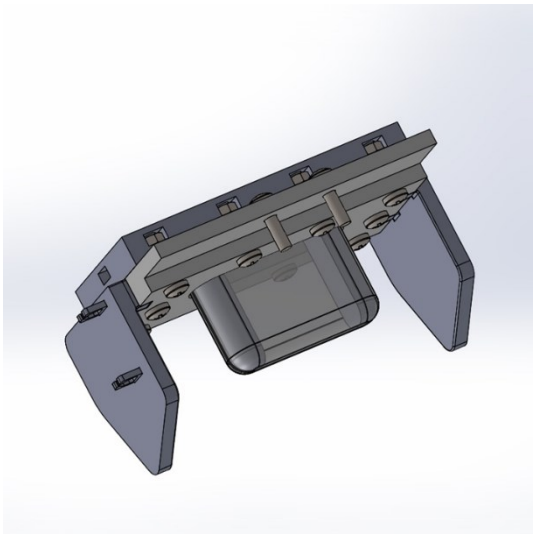

(b)

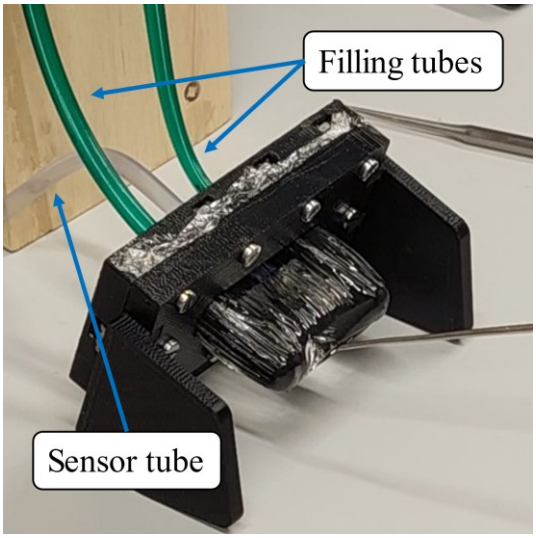

(c)

Fig. 3.13 CAD model of the tank. Exploded view of the tank system (a), the CAD of the assembled tank (b) and the tank assembled (c).

3.2.3.1.2 Characterization of the sensorized tank

The described tank was characterized with the same electronic setup described previously. To enhance the realism, as an indenter it was chosen a curette. Preliminary tests performed on the system indicated that the measured pressure changes with the configuration of the tank. Indeed, it was observed that the quantity of liquid, in conjunction with the presence of air within the tank, can influence the haptic sensation of the membrane, and so its resistance to indentation. This has an impact on the variation of the inner pressure during indentation, which in consequence affects the outcome of the tests. Accordingly, a filling protocol was established with an experienced surgeon to emulate the desired membrane rigidity. The sensorized tank is filled with distilled water via a single PVC tube until the total volume of water reaches 30 grams. Any excess water and entrapped air are then

removed through a second tube. This configuration ensures that the system is similar to the arachnoid membrane. Once the filling protocol was established, tests were conducted at a constant depth of penetration in the membrane. A total of 8 indentations with a displacement ranging from 1 to 15 mm (only odd numbers) were performed. These tests were repeated 3 times on 3 different days. Each of these replications was performed by changing the membrane, thus eliminating any potential alteration of the results due to membrane damage and also to test the repeatability of the system from one test to another.

3.2.3.1.3 Surgical simulation with expert surgeons

A pool of 11 international surgeons (3 neurosurgeons and 8 otolaryngologists) with experience in ETA ranging from 3 to 20 years, tested the model (Table 3.2). Surgeons were invited to participate in an in-field test of the training model, simulating the resection of a pituitary adenoma. During these simulations, boiled egg white was used to mimic the consistency of a pituitary adenoma. The idea came from the "EggHead" training models [75,77,80,88,92,185] mentioned in Chapter 1.

Table 3.2 Surgeons participating in field testing. (YoE = Years of Experience).

#	Country	Specialty	Years of experience
1	Italy	Otolaryngologist	15
2	Albania	Otolaryngologist	12
3	France	Neurosurgeon	20
4	Italy	Otolaryngologist	15
5	France	Otolaryngologist	3
6	Argentina	Otolaryngologist	15
7	Italy	Otolaryngologist	13
8	Italy	Neurosurgeon	14
9	Türkiye	Otolaryngologist	10
10	Italy	Otolaryngologist	15
11	Italy	Neurosurgeon	20

Surgeons performed the simulation using an endoscope, an aspirator to remove the egg white, and a curette to lift the polymeric film. An additional test was conducted using an alternative technique, which involved the use of a cotton gauze between the curette and the arachnoid membrane. This test was performed to compare the effects of the different techniques. Data on pressure and force applied to the membrane during the surgery were

collected and then analyzed using MATLAB. During tests, each interaction between the surgeon and the arachnoid membrane was registered as a peak. Data were initially filtered to remove noise, according to a threshold value of 0.1 N in accordance with the results obtained by Bekeny et al. [199]. The prominence of each peak was calculated using the MATLAB function *findpeaks*. Prominence is defined as the difference between the height of the peak and the lowest point in the nearest valley separating that peak from another higher peak. Results were used to define a threshold value above which the force applied is statistically likely to result in the tearing of the membrane.

At the end of the simulation, a questionnaire was surveyed to the surgeons to collect their feedback on the realism and usefulness of the training model. The questionnaire is shown in Table 3.3. The answers of the questionnaire are discussed in Section 3.2.3.2.3.1 Questionnaire results.

Table 3.3 The questionnaire submitted to surgeons.

Topic	Question					Answer type
Arachnoid	Q1	How do you evaluate the deformability of the arachnoid compared to the real one?				Type 1
	Q2	How do you evaluate the force resistance of the arachnoid compared to the real one?				Type 1
	Q3	Overall, how much do you think that the haptic feedback of the arachnoid is similar to the real one?				Type 2
Tumor	Q4	How do you evaluate the removability of the pituitary adenoma compared to the real one?				Type 1
	Q5	How do you evaluate the (consistency) deformability of the pituitary adenoma compared to the real one?				Type 1
	Q6	How do you evaluate the force resistance of the pituitary adenoma compared to the real one?				Type 1
	Q7	Overall, how much do you think that the pituitary adenoma is similar to the real one?				Type 2
General	Q8	Do you think that an instrumented training model for endoscopic transsphenoidal surgery could be useful?				Open-ended
	Q9	Do you have any suggestions?				Open-ended
Answer Type 1	-2 Lower		-1 Slightly lower	0 Neutral (goal)	+1 Slightly higher	+2 Higher
Answer Type 2	1/5 Strongly Disagree		2/5 Disagree	3/5 Neutral	4/5 Agree	5/5 Strongly Agree

3.2.3.2 Results

3.2.3.2.1 Development of the training model

Fig. 3.14 compares the CAD model (Fig. 3.14a) with the assembled ETA sensorized training model (Fig. 3.14b), which is ready to be used for surgical simulation.

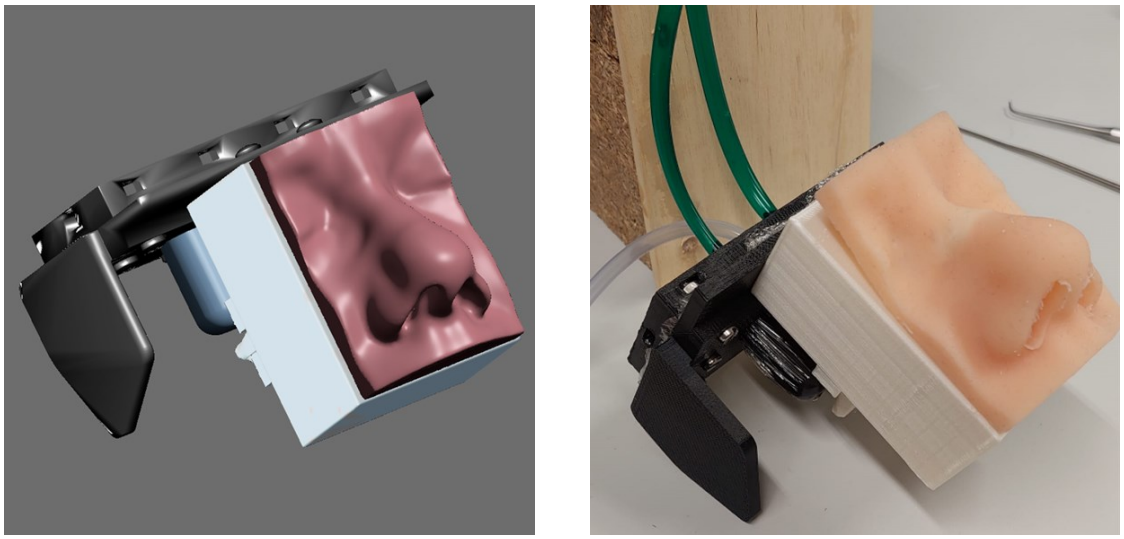

(a) (b)

Fig. 3.14 CT-based training model. Comparison between the CAD model (a) and the CT-based anatomical model ready for surgical simulation (b).

3.2.3.2.2 Characterization of the sensorized tank

For each repetition, the values of the peak prominence of force and pressure were recorded. The overall data shows a linear correlation between Force and Pressure derived from a linear regression model. The R^2 is 0.97 (sample size 161), with a measuring system sensitivity of 1.3 N/kPa. With the linear correlation found (Fig. 3.15), pressure data from the pressure sensor were converted into force, to evaluate the force applied to the membrane.

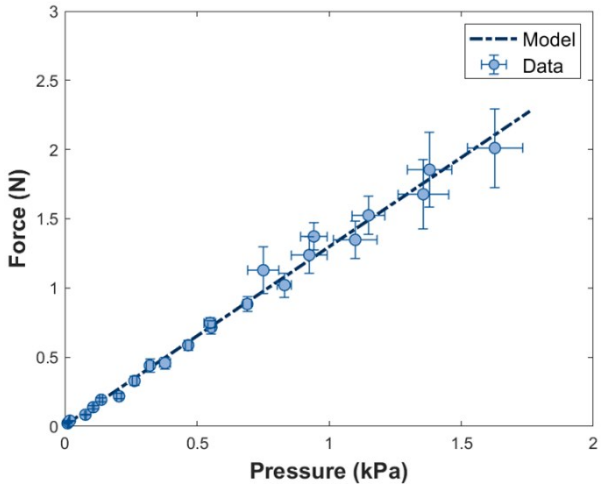

Fig. 3.15. Results of the characterization tests. Correlation between force (N) and pressure (kPa) values obtained through the characterization tests conducted on the tank (sample size 161). The resulting model was found to be linear and R^2 = 0.97 and a sensitivity of 1.3 N/kPa.

3.2.3.2.3 Surgical simulation with expert surgeons

Before testing with experienced surgeons, the upper sphenoid bone module of the training model was drilled to expose the arachnoid membrane. In addition, for simplicity, the turbinates and nasal septum modules were removed from the training model. Figure 3.16 shows the laboratory simulation with expert surgeons. Figure 3.17 shows the results of a single surgeon's performance. The blue line represents the simulation, while the orange line depicts the average trend. The black circles indicate the peaks in pressure observed during each interaction with the arachnoid. The introduction of the egg white specimen into the sella turica resulted in an initial compression of the membrane, followed by an increase in pressure as measured by the pressure sensor. As the resection of the tumor progressed, the average trend demonstrated a decline, indicating a reduction in pressure. Fig. 3.18 shows two images taken with the endoscope for both techniques: stand-alone curette (Fig. 3.18a) and curette with cotton gauze (Fig. 3.18b).

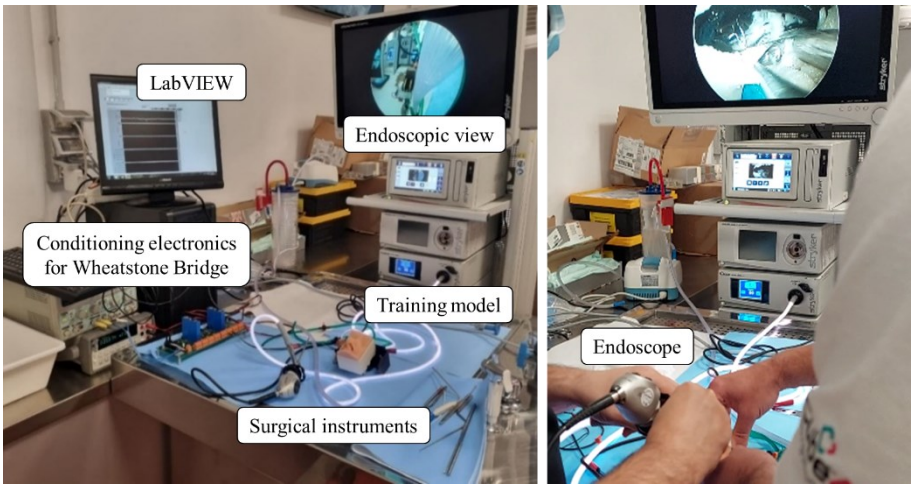

Fig. 3.16. The experimental setup during the field testing with experienced surgeons.

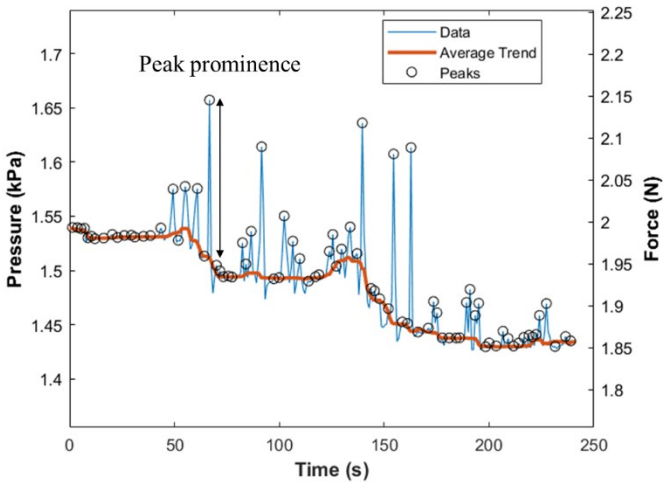

Fig. 3.17. Example of a tumor removal performed by an experienced surgeon. The tumor removal is measured and reported (blue line). Removing the tumor causes here an average decreasing trend (red line). Local peaks are a consequence of the compression of the membrane by the curette (black circles). The peak prominence was calculated using the MATLAB function *findpeaks*.

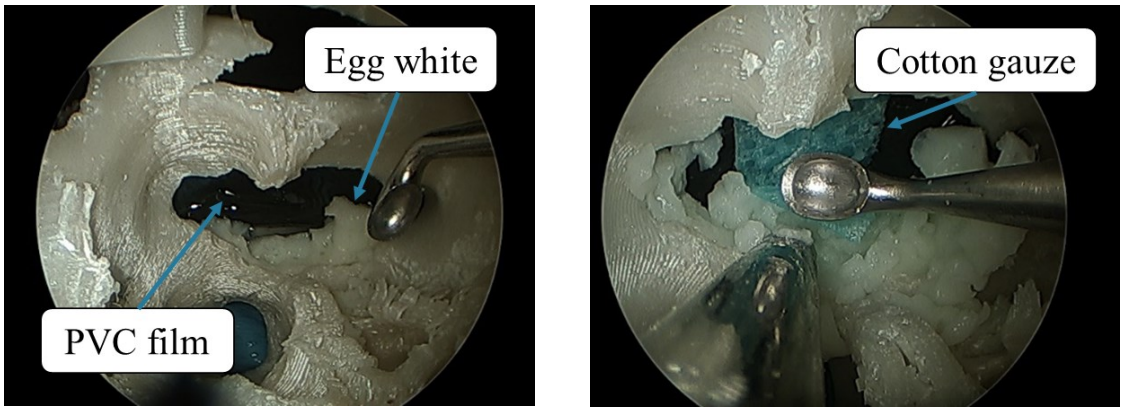

(a) (b)

Fig. 3.18. Endoscopic view of the field tests with experienced surgeons. Removal of the tumor with a curette with the arachnoid partially falling and covering the adenoma (a). The same procedure was performed, but a cotton gauze was placed between the curette and the membrane (b).

To evaluate the stresses acting on the membrane during the surgical procedure, peak prominence values were considered and analyzed for every surgeon combined. Then, their mean and standard deviation values were estimated, $\mu = 0.23$ N and $\sigma = 0.099$ N, respectively. These values were used to define three areas (Fig. 3.19a). Similarly, the results of the test performed using the cotton gauze between the curette (Fig. 3.19b) and the membrane were elaborated. Their average and standard deviation are $\mu = 0.28$ N and $\sigma = 0.17$ N, respectively. A summary of the results can be found in Table 3.4.

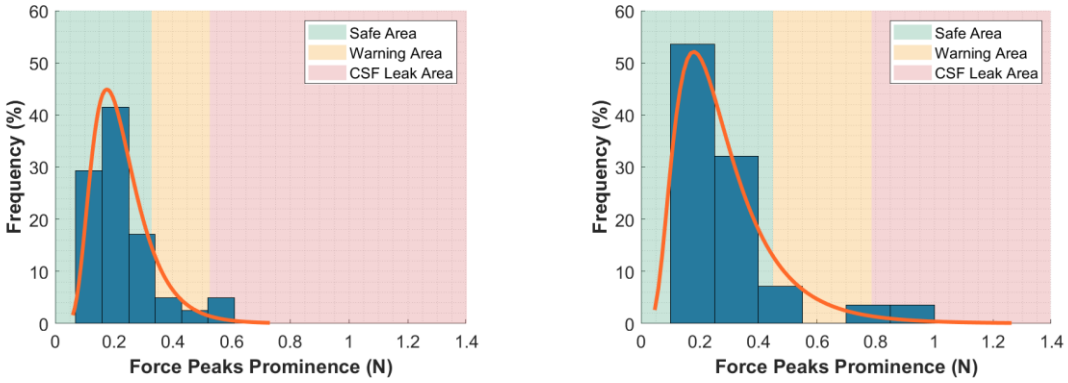

Fig. 3.19. Histograms of the force peak prominence values. Without the cotton gauze (a) and with the cotton gauze (b). Three working areas were defined based on the surgical risk: the Safe Area (up to μ + σ), the Warning Area (between μ + σ and μ + 3 σ), and the CSF Leak Area (over μ + 3 σ). The safe area was found to be wider when using cotton gauze. In particular the mean value and the standard deviation obtained from tests without the cotton gauze are 0.23 N and 0.099 N respectively. Thus, resulting in a Safe area range from 0.10 to 0.33 N, while the Warning area range from 0.33 to 0.53 N, while the CSF Leak Area for value above 0.53 N (a). Regarding the tests conducted with the cotton gauze the mean and the standard deviation obtained are 0.280 N and σ = 0.17 N respectively. Thus, resulting in a Safe area range from 0.10 to 0.45 N, while the Warning area range from 0.45 to 0.62 N, while the CSF Leak Area for value above 0.62 N (b).

Table 3.4 Ranges of the Safe, Warning, and CSF Leak Areas for the Force applied on the membrane, compared with data available in the literature [199].

Data	Unit	Technique	Safe Area	Warning Area	CSF Leak Area
Bekeny et al. [199]	N	Sensorized Curette	0.10 ÷ 0.50	-	-
Force (our results)	N	Curette	0.10 ÷ 0.33	0.33 ÷ 0.53	> 0.53
Force (our results)	N	Curette and Cotton Gauze	0.10 ÷ 0.45	0.45 ÷ 0.62	> 0.79

3.2.3.2.3.1 Questionnaire results

Fig. 3.20 shows the results of the questionnaire, divided by medical surgeon's specialty: Neurosurgery (Ns) and Otolaryngology (Ot). The mechanical behavior of the membrane (Q1 and Q2) and the tumor (Q4, Q5, and Q6) are close to the goal (neutrality to actual tissues), as illustrated in Fig. 3.20a. Overall, Q3 and Q7 suggest that some aspects of the model should be improved to get closer to reality, as illustrated in Fig. 3.20b. In particular, the open-ended answers Q8 and Q9 explain that the improvements should involve the following aspects:

- The arachnoid could be looser and thinner.
- The tactile feedback of the adenoma is optimal, but different consistencies should be provided (softer and harder). Moreover, its fragility-deformability when curetting is different as the tissue breaks into larger parts. Its "liquidity" should be increased.
- Colors in the model and bleeding should be included.

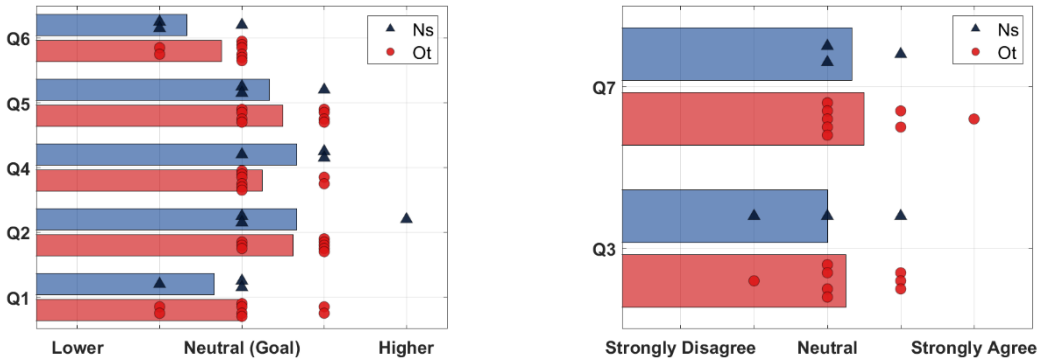

Fig. 3.20 Results of the questionnaire. Answers are divided by medical specialty, Neurosurgery (Ns), and Otolaryngology (Ot). The mechanical behavior of the membrane (Q1 and Q2) and the tumor (Q4, Q5, and Q6) are close to the goal (neutrality to actual tissues) (a). Q3 and Q7 suggest that some aspects of the model should be improved to get closer to reality (b).

3.2.2.3 Discussions

The characterization of the pressure sensor reported in Fig. 3.9 reveals a clear linear correlation between force and pressure, although the dispersion of data increases for values of pressure exceeding 1 kPa. The resulting characterization model was used to convert the data from pressure to force to verify that they were consistent with the work found in the literature. The standard deviation of pressure values ranges from < 0.0010 at 0.010 kPa to 0.11 at 1.6 kPa, while the standard deviation of the force ranges from 0.001 at 0.032 N, to 0.28 at 2.011 N. With the sensorized tank mounted on the training model as shown in Fig. 3.14, tests were performed with experienced surgeons in the anatomical laboratory as shown in Fig. 3.16. A removal of PA with ETA was simulated using an egg white sample used to mimic the pituitary adenoma as suggested by literature [75,77,80,88,92,185]. Surgeons were asked to remove the egg white as in real ETA surgery while the force exerted on the polymeric film was measured. From results, an initial compression is evident: it is caused by the egg white sample inserted into the model which compresses the arachnoid membrane. Subsequently, the trend of the surgical test shown is decreasing, since the removal of the egg white specimen slowly decompresses the membrane thus reducing the overall internal pressure in the tank (Fig. 3.17). Two different techniques were tested: one using a stand-alone curette and the other employing cotton gauze, as illustrated in Fig. 3.19. From the results emerged that both tests configuration: stand-alone curette and with the cotton gauze, follow a log-normal distribution with a p-value of 0.97 and 0.55 respectively. The three different areas, according to the surgical risks were defined: the Safe Area (green) for force values lower than $\mu + \sigma$, the Warning Area (yellow) for forces between $\mu + \sigma$ and $\mu + 3\sigma$, and the CSF Leak Area (red) for forces greater than $\mu + 3\sigma$. The Safe Area represents those values of force that were considered safe during the

simulation. The Warning Area represents those values that are close to the breaking of the membrane. The CSF Leak Area contains the highest force values, which are associated with the rupture of the arachnoid membrane for the patient. The force limits of the three areas were compared with the ones present in the literature (Table 3.3). Bekeny et al. [199] measured the force exerted by surgeons during a transsphenoidal surgical approach using a custom-made curette with an embedded load cell. The resulting force exerted on the soft tissues is in the range of 0.1 ÷ 0.5 N, which corresponds to the maximum value of the Warning area. Even though there is no experimental validation of the limit values found here, they are reasonable. Further investigation will define their values better. The gauze, when inserted over the arachnoid membrane, allows the surgeon to distribute the pressure exerted by the surgical instrument to a wider area, thereby increasing the range of forces that can be applied, and the force limit of the CSF Leak Area is 49% higher (Table 3.3). Hence, a higher force is permitted during the surgical procedure without increasing the risk of arachnoid damage. The preliminary threshold value is of interest, but a critical aspect must be considered: the reduced sample size of surgeons (n = 11) with which the study was conducted. This is a statistically limited result. In order to validate the sensor-based model, the aim for the future is to produce several training models and to design specific training sessions. In this way it will be possible to better evaluate a critical threshold value that can be used as a parameter to assess whether a less experienced surgeon/resident is able to perform simulated tumor mass removal without exceeding this threshold value. Training sessions will be conducted during specific neurosurgical summer schools and/or workshops to teach participants how to handle the arachnoid membrane before the operating room.

Nowadays the gold standard of training is still training with cadaver head models, and the prototype of this training is not yet ready to effectively substitute them. However, it could be a fundamental tool in preparing surgeons to gain the necessary dexterity to perform a transsphenoidal approach surgery safely before training on the cadaver head models. This training is therefore carried out with low-cost and reusable tools, such as the training model presented in this thesis, before training on a non-reusable cadaver head in an anatomical laboratory, which is an expensive solution given the low availability of human cadaver heads and the high maintenance costs of the laboratory.

Compared to similar commercially available training model found in the state of the art review presented in Chapter 1: the training model SIMONT (Pro Delphus, Brazil) [95] and the Kezlex (JMC (Japan) [99,105] and the training simulator with augmented reality: the PHACON (Phacon GmbH, Germany) [139] and the TNS (UpSurgeOn S.r.l., Italy) [145] the

developed model present several strengths and several weakness, which are reported in following table 3.5

Table 3.5 Comparison between the training model presented in this thesis with the commercially available training model presented in the state of the art analysis in chapter 1.

Strengths	Weakness
- Representation of the arachnoid membrane and the CSF fluid - Real time feedback about the force exerted with a threshold value marking the maximum value that can be safely exercised - Low cost in terms materials, fabrication technology and sensors used.	- Lower anatomical fidelity - The model is still a prototype - Lacks augmented reality

3.3 Conclusions

The concept prototype showed a low repeatability from one test to another; however, data show interesting inter-test repeatability, meaning that such system can measure the force applied on the polymeric membrane. The low repeatability of the first prototype was increased with the final development of the improved version of the sensor-based tank if compared to one test to another. This was possible for the increased design and also for the usage of a specific filling protocol for the system. Once the ETA training model was characterized, it was tested by 11 experienced international surgeons, who simulated a pituitary adenoma resection procedure, using pieces of boiled egg white to emulate the tumor. During the session, force values and surgeon's feedback were collected. Results on force are in with the literature and allowed the identification of three working areas (Safe, Warning, and CSF Leak), which can be used to evaluate the trainee's performance. The innovative features of the model received valuable feedback from the surgeons, in particular, the arachnoid and the consistency of the pituitary tumor were well mimicked. Future studies will be conducted more systematically with a greater number of surgeons with different levels of experience, especially with residents, to ascertain whether the training with the ETA training model has had a positive impact by comparing their force outcomes with more experienced surgeons during multiple simulations, and to provide a more robust value of the maximum force that can be exerted on the polymeric film. In addition, once the threshold value will be determined, it will be used as a tool to evaluate whether a surgeon is able to safely remove the pituitary tumor without damaging the arachnoid membrane, making the model a parameter to determine whether the surgeon is ready to enter the operating room.

Chapter 4

Sensor-based instrument to measure the hardness of pituitary adenomas

This chapter describes the second aim of the thesis: the development of a novel surgical instrument for an in-vivo measure of the hardness of a pituitary adenoma. As already mentioned, one difficult aspect of this surgery is determined by the fact that, depending on the hardness of the tumor, the surgeon must choose the best strategy for the resection of the tumor. In the literature are listed a total of 5 categories of pituitary tumor, according to its hardness, as pointed out by Rutkowski et al., from “cystic/hemorrhagic”, the softest, to “calcified”, the hardest [201]. The different hardness is related to the histological characteristics of the tumor [202]. Usually, softer PAs, which are the most common [203,204], can be easily aspirated, while the harder ones require prior fragmentation [205,206]. It is important that surgeons can recognize the consistency intraoperatively and then decide which is the best strategy for the resection. However, knowing the hardness of the tumor before the surgery would allow surgeons to plan the most effective removal technique for the specific case, thereby reducing the risks to the patient. In the literature, different methods are available to preoperatively investigate the consistency of PAs, however, none of them has sufficient reliability in clinical use [207,208]. MRI images only are not sufficient to preoperatively predict the hardness of pituitary adenomas. Nevertheless, the integration of radiomics analysis with artificial intelligence is emerging as a highly effective approach for predicting tumor hardness [209,210].

What is missing is an evaluation of the mechanical properties of PAs, due to the position of the tumor. Bekeny et al. [199], in their analysis of the forces registered during the resection of a pituitary adenoma with a transsphenoidal approach, stated that the level of forces applied during the surgery ranged from 0.1 to 0.5 N during the excision of pituitary lesions [199]. In addition, Stewart et al. [211] propose a mechanical characterization performed with a sensorized indenter to determine the consistency of brain tumors with a steady-state modulus parameter defined by the authors themselves.

The designed instrument consists of two parts, both fabricated with 3D printing technologies: a rigid case with and a highly deformable tip. The main challenge of this project

is to develop an instrument with a diameter small enough to fit within the nasal cavities and to perform in future, in-vivo tests.

This chapter is set into three parts, each of which describes a prototype of the instrument. From the first prototype to the last one, the instrument design was improved and optimized, to fit the size limitations given by the anatomy and the position of the tumor, and also to be sensitive to the hardness of softer tumors. The goal of this instrument will be to test intraoperatively the hardness of PAs.

The first part describes the first version of the probe, in which preliminary tests were performed on the system, regardless of its external diameter of 8.4 mm, which was definitely too high to access the pituitary adenoma – however results were promising.

The second part presents an optimization in terms of design of the probe. The external diameter, from 8.4 mm in the previous part, was reduced to 5.6 mm, which is closer to the diameter of the endoscope used. In addition, two tips thickness were tested to verify the best solution in terms of sensitivity and repeatability of the instrument. Tests were also performed using silicone samples and a sample of egg white. As mentioned in Chapter 3, the egg white is a good representation of the pituitary tumor, as emerged from the literature [7,75,80,184,185,193,194] and from surgical experience. From the tests performed, a preliminary value of the hardness of the egg white was found, which is related to the real hardness of the pituitary adenoma.

The last part reports the process for the optimization of the tip, in order to find the best configuration. In particular, the effect of the main printing parameters on the printed width of the beams (i.e., the elements of the tip that undergo deformation) was investigated. Additionally, the hardness of the sample was measured with a Shore 000 durometer. From data emerged that the regression model obtained from the relation between the Shore 000 hardness and the deformation of the tip predicted with accuracy the hardness of the egg. The results achieved are very promising and the probe will be further developed by testing real biological tissue to evaluate its performance and validate it in the surgical field. Then, tip designs different in beam width and number were fabricated and tested using samples with a hardness in the range from 51 to 83 on the Shore 000 scale, and a sample of egg white.

4.1 The Concept

The sensorized probe is designed to calculate the deformation of a highly deformable tip through the variation of the magnetic field generated by the displacement of a magnet glued to the tip and measured by the magnetoresistive sensor.

The concept is that the degree of deformation is contingent upon the hardness of the surface to which the tip is pressed. This behavior can be modeled as two springs in series with different stiffness, in accordance with Hooke's law. To exemplify, the probe is pressed against the surface with an imposed indentation of 1 mm. If the hardness of the surface is significantly greater than that of the tip, the displacement of the tip, or the magnet glued to it, is equal to the imposed distance, which is 1 mm. This results in a maximum deformation of the tip. Conversely, when the tip is pressed against a surface with a comparable hardness, the total displacement of the magnet is less than 1 mm due to the partial deformation of the surface. This allows for the comparison of the hardness of different materials undergoing the same experimental procedure. The deformation is expressed as a parameter, defined as $h_{\%}$ and used to represent the percentage variation in the distance between the initial magnet-to-sensor distance, d_0, and the final magnet-to-sensor distance, d_p (Fig. 4.1). The expression of this parameter is provided below in equation (1).

$$h_{\%} = \frac{d_0 - d_p}{d_0} \cdot 100 \qquad (1)$$

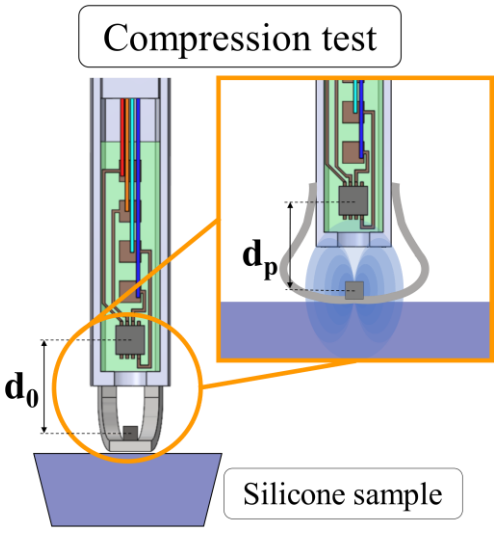

Fig. 4.1 (a) The TMR sensor measures the variation of magnetic field during compression tests which is related to the deformation of the tip, depending on the hardness of the specimen tested.

4.2 Design of the Probe and Fabrication

The probe consists of three parts: a rigid and hollow structure named rigid case, a tunnelling magneto-resistive (TMR) sensor and a highly deformable tip with a magnet glued. (Fig. 4.2).

4.2.1 The rigid case

The rigid case consists of a hollow cylinder in which the PCB with TMR sensor is inserted (Fig. 2).

4.2.2 The TMR sensor

The TMR sensor used is an Ultra High Sensitivity TMR linear sensor model TMR2905S (MultiDimension Technology Co., Ltd., China). The main advantage of TMR sensors is that they can be sealed inside a magneto-transparent material thus eliminating the risk of contact with biological liquids. The TMR sensor, with dimensions of 3 x 3 mm, is soldered onto a printed circuit board (PCB) with dimensions of 4.2 x 22 mm (Fig. 4.2) and it measures the variation of the magnetic field caused by the displacement of the magnet attached to the tip. Accordingly, the TMR sensor was characterized. The choice of a TMR sensor was given by the fact that it can be encapsulated, meaning that it eliminates the contact with anatomical tissues, and it overcomes the problem of biocompatibility [212].

4.2.3 The highly deformable tip

The tip represents the core element of the probe. The tip consists of a flat circular plate from which several beams extend radially, the tip is folded and glued to the rigid case, so that the flat circular plate is the contact point with the tested surface. A 1x1x1 mm cubic magnet is glued to the circular plate. The main advantage of this design is the fact that the measurement of hardness is performed without friction because no relative movement of the parts of the probe occurs.

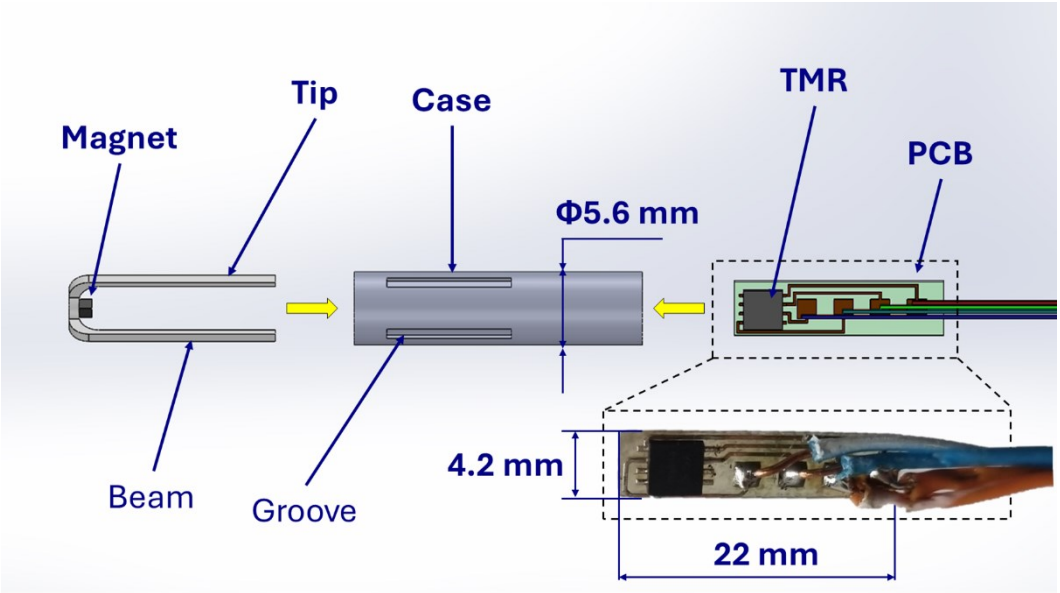

Fig. 4.2 Exploded view of the concept design of the probe.

4.2.4 Fabrication of the Probe: 3D printing process and materials

Two different materials were chosen for the fabrication of the probe parts: the rigid case and the highly deformable tip. To provide the required stiffness to the rigid case, it was chosen PLA, one of the most common 3D printing materials and therefore one of the least expensive: it was used the Pearl - White PLA filament, one of the PLA produced by Ultimaker. The filament used has a diameter of 2.85 mm and it was printed using the AA025 print-core to reproduce both the small details of the rigid case and its overall size. To print the highly deformable tip, a different material was found to be the best solution in terms of lower rigidity of the printed parts. The material chosen was the TPU 95A by Ultimaker, another common and low-cost 3D printing material, which is suitable for printing flexible components, i.e. the tip. The TPU 95A filament used has a diameter of 2.85 mm and it was printed using the AA04 print-core, a print-core with a diameter of 0.4 mm. Concerning the choice of materials TPU has a flexural strength, and a flexural strain lower compared to PLA, which means that it is more suitable to produce highly deformable parts as the tip. A more detailed comparison between these two materials is shown in Table 4.1 (similar to Table 2.2), where are reported data from the technical datasheet of the materials [187,189]. Datasheets report data considering the orientation of the specimen during printing, in particular: XY refers to the plane of the printing plate, while Z is the direction of the printing (perpendicular to the printing plate).

Table 4.1 Mechanical properties of Pearl-White PLA and TPU 95A. XY, YZ and Z refer to the orientation of the specimen tested, X-Y is the printing plate, while Z t is the printing direction. Data are taken from material datasheets [187,189]. As mentioned in the datasheet, tests are performed following the ISO 178 regulations. NB= No Break (> 10%)

Material	Hardness (Shore D scale)	Flexural modulus (MPa)			Flexural strain at break (%)		
		XY (Flat)	YZ (Side)	Z (Up)	XY (Flat)	YZ (Side)	Z (Up)
PLA	84.0	3019 ± 87.0	2894 ± 53.0	2740 ± 47.0	4.8 ± 0.2	NB	1.9 ± 0.2
TPU 95A	48.0	62.6 ± 1.7	55.1 ± 2.4	62.6 ± 2.0	NB	NB	NB

4.3 The electronic setup

The electronic setup is the same presented in Chapter 3 for characterization tests with the sensorized training model. The probe is mounted on a load cell in turn fixed on a micrometric slide which can be controlled in position and speed. The probe is moved against a sample by a micrometric slide whose position and speed are computer controlled. The TMR sensor has a supply voltage of 1 V while the load cell of 10 V. A multimeter collects the signal from the TMR sensor, which is related to the deformation of the tip, while a second multimeter

collects the signal from the load cell, which is related to the force applied to the tip. Data are acquired with a LabVIEW program at a sampling rate of 2 Hz and then analyzed using MATLAB software (Fig. 4.3). A summary of the electronic setup used is reported in Table 4.2.

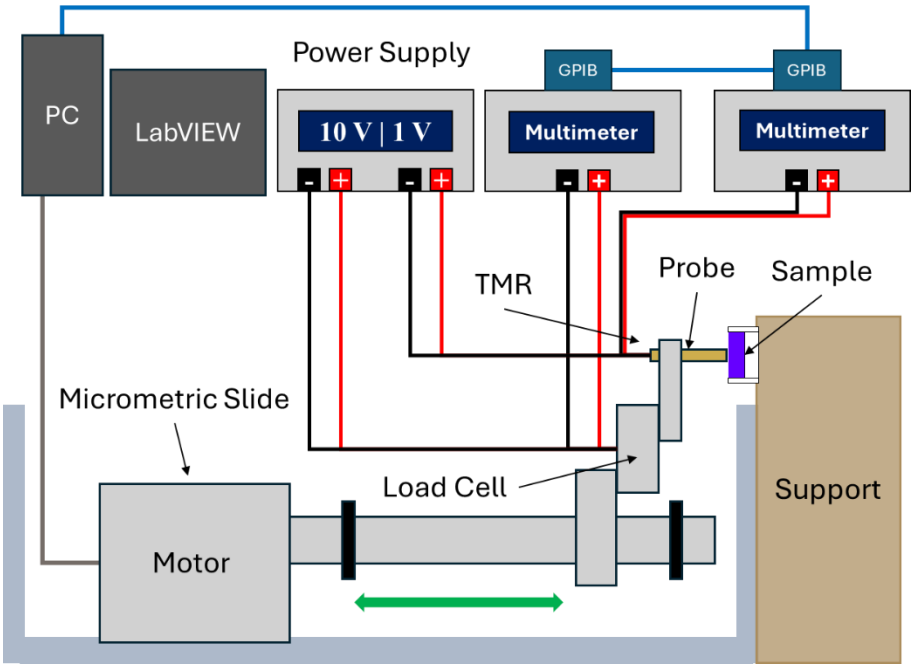

Fig. 4.3 The electronic setup. The probe is moved against a sample by a micrometric slide whose position and speed are computer controlled. The TMR sensor has a supply voltage of 1 V and the load cell of 10 V with a sensitivity of 4.4 (N/mV). A multimeter collects the signal from the TMR sensor, which is related to the deformation of the tip, while a second multimeter collects the signal from the load cell, which is related to the force applied to the tip. Data are acquired with a LabVIEW program at a sampling rate of 2 Hz and then analyzed using MATLAB software.

Table 4.2 The electronic setup used for testing.

Component	Model	Specifications	Use	Notes
Power supply	PL330DP	Independent channels	To power the load cell at 10V and the TMR sensor at 1V	-
Multimeter 1	HP 34401A	Resolution: 6½ digits	To read the load cell data	-
Multimeter 2	HP 34401A	Resolution: 6½ digits	To read the pressure sensor data	-
Micrometric Slide	-	Resolution: 0.010 mm	To move the probe	Computer controlled
Load Cell	-	Sensitivity: 4.4 N/mV	To measure contact force	-

TMR Sensor	TMR2905S	Dimensions: 3 x 3 mm U: 4.7E-04 V	To measure the variation of the magnetic field generated by a magnet glued to the tip	Soldered on a PCB of 4.2 x 22 mm
GPIB-USB-HS interface	-	-	To allow simultaneous collection of both sensors	-
LabVIEW	-	Sample rate: 2 Hz	To obtain data during tests	-
MATLAB	-	.	To analyze data	-

4.3.1 Sensor Characterization

In order to determine the deformation of the tip, it was necessary to know the distance between the magnet and the sensor at any given instant. To do so, the TMR sensor was characterized in terms of displacement. The magnetoresistive sensor was therefore characterized as a function of distance in a specifically designed test. The board was positioned inside the probe, which was mounted on the micrometric slide. The tip was positioned on a flat surface right below the micrometric slide with the magnet attached to it. In this chapter are reported different sensor characterizations that were performed each time with a new probe design and different TMR sensors.

4.3.2 Probe Characterization – Indentation Tests

Each probe, as presented in this chapter, was tested using the same procedure, designated as the Indentation Test. This entailed a repetitive compression of the tip against the surface of the selected sample. The movement of the probe was generated by the micrometric slide to which it was mounted. The Indentation test was conducted as follows:

- *First contact*. The tip is moved against the sample using a 0.10 mm step motion. First contact is detected through the axial force measured by the load cell.
- *Indentation*. The probe moves 1.00 mm towards the sample at 1.00 mm/s and holds for 1 minute, then returns. The first indentation is used to settle the tip and therefore discharged. Then, indentation is repeated 3 times on the tested sample.
- *Data acquisition*. During indentation, signals from load cells and TMR are collected and converted respectively in contact Force and distance of the tip (i.e. magnet) from the sensor.

4.4 Sensor-based Tissue Probe Prototypes

In the following section it is presented the first design of the probe, which was then tested to verify the functioning of the system and its capability to discern the hardness of different soft materials, i.e. soft silicones.

The following section is adapted from the conference paper entitled “Preliminary Study on a 3D Printed Sensorized Probe to Characterize Pituitary Adenoma Hardness” published in “2023 IEEE International Workshop on Metrology for Industry 4.0 & IoT (MetroInd4.0&IoT) in July 2023 [195].

4.4.1 Prototype 1 - Concept

The rigid case of the first prototype is a 50 mm long hollow cylinder with an inner diameter is 4.6 mm while its thickness is 1.9 mm, thus giving a total of 8.4 mm. The rigid case presents external grooves which are designed to allow better coupling between the body and the tip. The tip is a five-armed thin structure with a circular plate in the middle to allow placement of the magnet. The thickness of the tip is 0.70 mm while the length and the width of its arms are respectively 30 mm and 1.4 mm. The model of the tip is shown in Fig. 4.4 (a). The tip is folded and glued to the body as shown in Fig. 4.4 (b). Fig. 4.4 (c) shows the probe mounted on the computer-controlled micrometric slide ready to perform a test.

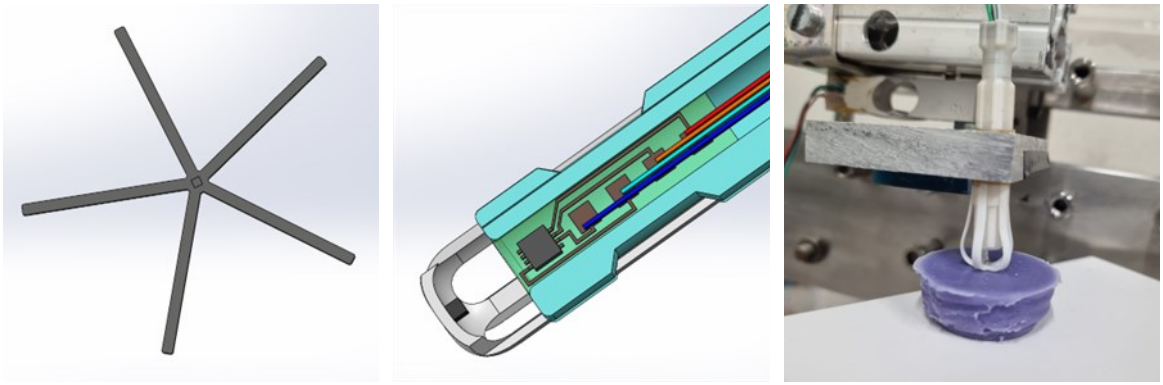

(a) (b) (c)

Fig. 4.4 The tip (a) is a five-armed thin structure with a circular plate in the middle to allow placement of the magnet. A section of the sensorized probe (b) shows the relative position of the TMR2905S and the magnet. The probe consists of two parts: the body whose function is to provide stability to the whole probe and a five-armed tip. The body is a 50-millimeter-long hollow cylinder with 5 grooves all over it. The inner diameter is 4.6 mm while its thickness is 1.9 mm. The thickness of the tip is 0.70 mm while the length and the width of its arms are respectively 30 mm and 1.4 mm. The probe is mounted on a computer-controlled micrometric slide, and it is ready to perform a test (c).

4.4.1.1 TMR Characterization

A preliminary characterization of the magnet-sensor distance curve was performed, from a maximum distance of 20 mm to contact, 0 mm distance, with the sensor in 300 µm steps. After reaching the minimum distance, the device was raised in 600 µm steps. The achieved results produced the calibration curve shown in Fig. 4.5. The calibration test was performed without the tip, in the sense that the magnet was glued on a flat surface and while

the sensor was moved with the micrometric slide, in this way it was possible to measure a wider range of the sensors, from 0, i.e. the contact between magnet and sensors, to “infinite”, i.e. that distance above which the magnetic field variation generated by the relative movement of the magnet was no longer sensed by the sensor, in this case for a distance greater than 15 mm as shown in Fig. 4.5 where it is evident a saturation plateau. As expected from the sensor specifications it presents a non-linear behavior with saturation on both the measurement limits. From other previous tests it resulted that the sensor has a measurement uncertainty of 4. 7E-04 V. It was defined as the standard deviation of the sensor output in V of the peaks reached through ten repeated cycles from 0 to 10 mm of the micrometric slide, using the characterization setup of the sensor.

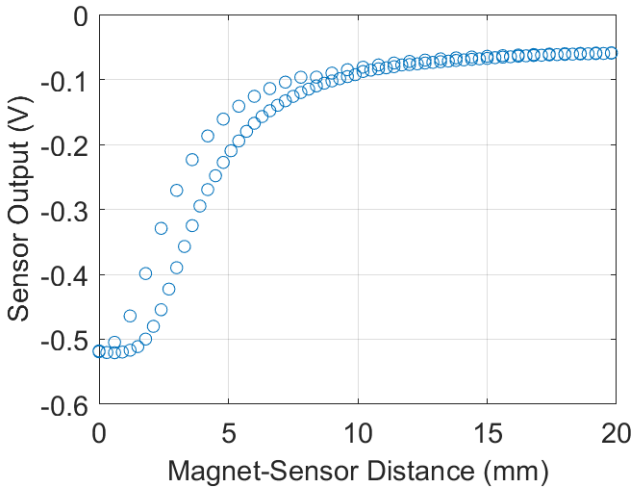

Fig. 4.5. Sensor calibration curve achieved with the selected magnet. As emerged from previous tests the sensor has a measurement uncertainty of 4.7E-04 (V).

The sensitivity of the achieved device is always negative and with a magnitude variable between $-1.1 \cdot 10^{-3}$ V/µm and $-5.1 \cdot 10^{-6}$ V/µm, as shown in Fig. 4.6. Moreover, Fig. 4.5 and Fig. 4.6 show a hysteresis in the measurements which is related to the magnetic field variation that is exploited for the displacement measurement. In order to overcome the problem, only compression experiments will be considered for the next evaluations. Tests were then carried out to obtain the displacement-voltage characteristics shown in Fig. 4.7. The curve was obtained with a 3rd degree linear interpolation based on a sample size of 17, using the MATLAB function *fitlm*, the obtained RMSE of the model is 0.058 and the R^2 is > 0.99.

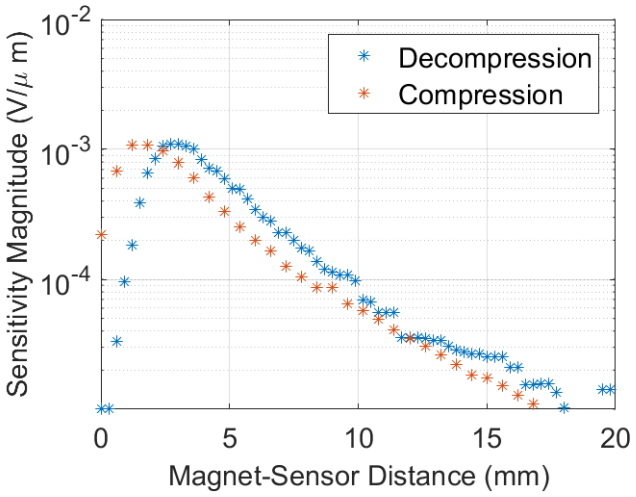

Fig. 4.6. Sensitivity of the device at different magnet-sensor distances.

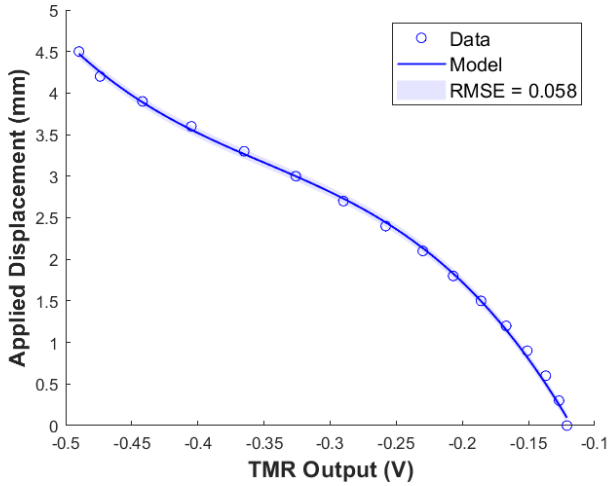

Fig. 4.7 Device calibration curve. Data were fitted using a 3rd degree linear regression model, the RMSE is 0.058 (highlighted area) while the R^2 is > 0.99 based on a sample size of 17. As already mentioned, from previous tests it was found that the TMR sensor has a measurement uncertainty of 4.7E-04 (V), while the resolution of the micrometric slide is 0.010 mm.

Regarding the tests performed on the silicone specimen, the probe was mounted as in Fig. 4.4 (c), so the relative movement of the magnet and the sensor was limited to a 1.00 mm range. In the chosen configuration, the selected maximum distance is the one that provides a 0.10 V output bias to improve the sensitivity of the overall system to compression.

4.4.1.2 Sample Preparation

The first probe prototype is tested with three silicone samples of different hardness. Samples were produced using Shamrock Elite Double 8, Zhermack Elite Double 16 (Zhermack Spa, Badia Polesine, Italy) and Silicon Mix SH A 12 Orange (ITALGESSI SRL, Castigliano, Italy) with nominal Shore A 8, 16 and 12 respectively. All the sample materials were mixed 1:1 in

volume as suggested by the manufacturer and poured in a cylindric mold with a radius of 15 mm and a height of 15 mm. After pouring, the molds were placed in vacuum to avoid trapped air bubbles and left curing overnight at room temperature. The experimental setup was set as before, controlling the movement by means of a computer-controlled micrometric slide and measuring the output of the sensor with the above-mentioned digital multimeter. The probe was at first placed in contact with the sample under test (SUT). Then the measurement starts, and the probe is pressed 1 mm towards the SUT, and the actual displacement was measured. The position was maintained for 60 s to consider the elastic return of the material and then the probe was risen to its starting position. This test cycle was repeated three times.

4.4.1.3 Prototype 1 - Results

The first probe was tested with the three samples described previously, and the results are provided in Fig. 4.8. In particular, in Fig. 4.8a, which reports the signals in time domain for three samples, is evident the high repeatability of the tests, the mean variation from one repetition to another for the three SUTs is < 1%. In Fig. 4.8b is reported the calculated displacement and the difference of the output voltage of the probe. The mean values of the differences between the compression and the initial offset (Fig. 4.8a) for the 8, 12 and 16 shore A hardness specimen are 532 ± 9.2 µm, 600 ± 9.2 µm and 609 ± 9.7 µm respectively for the displacement data, while 45 ± 4.4 V, 57 ± 4.7 V and 59 ± 5.4 V respectively for sensor's output data. Fig. 4.8c shows the calculated $h_{\%}$ for the three SUTs, in particular $h_{\%}$ values found are: 53 ± 0.92, 60 ± 0.92 and 61 ± 0.70 respectively. Finally in Fig. 4.8d, is reported as reference, the force applied by the indenter, the values found for the three SUTs are: 0.26 ± 0.075 N, 0.39 ± 0.076 N and 0.43 ± 0.086 N, respectively. As expected, the achieved displacement resulted in less than the applied one (1 mm) since the sample deformed and reduced it.

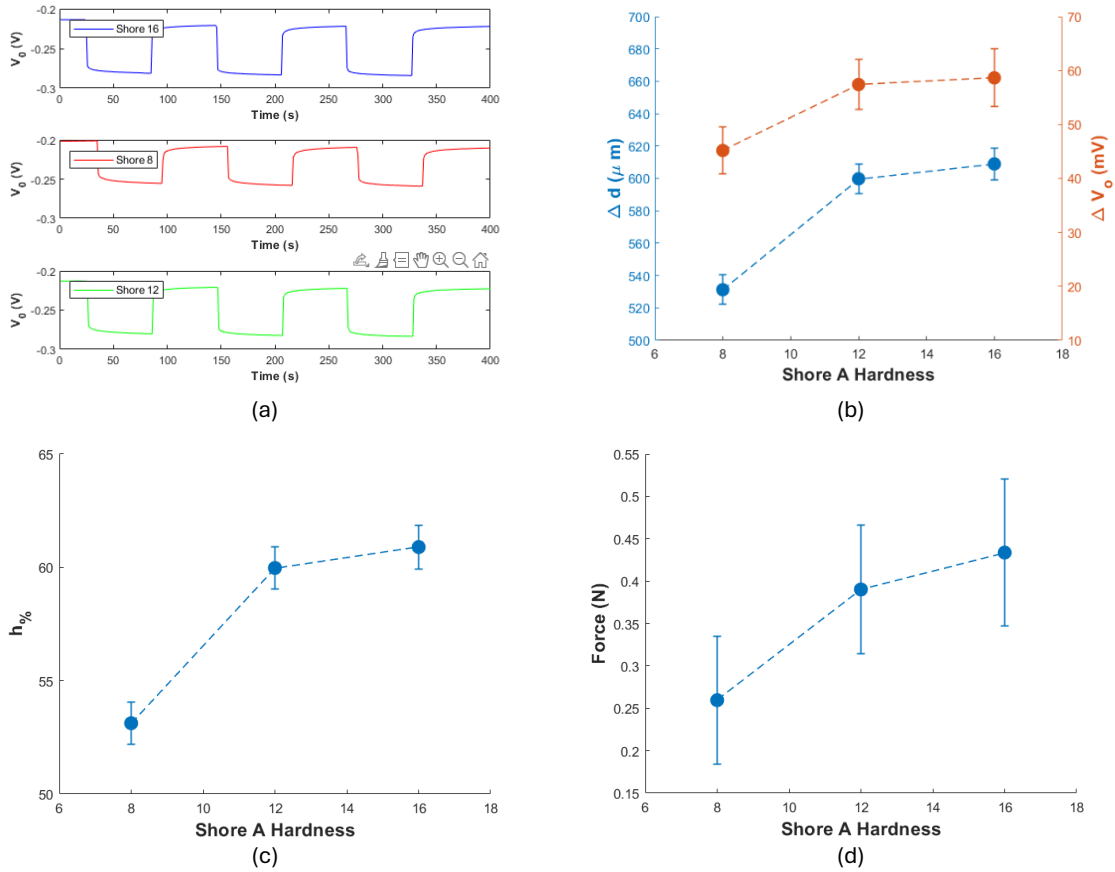

Fig. 4.8 Data acquired during the characterization. Signals in time domain for three samples with Shore 16, 8 and 12 (a). Calibration points in terms of the measured displacement and the output voltage of the sensor (b), the measured $h_{\%}$ (c) and the force measured with the above-mentioned force sensor (d). As already mentioned, from previous tests it was found that the TMR sensor has a measurement uncertainty of 4.7E-04 (V).The mean values for the 8, 12 and 16 shore A hardness specimen are 532 ± 9.2 µm, 600 ± 9.2 and 609 ± 9.7 respectively for the displacement data, while 45 ± 4.4 V 57 ± 4.7 V and 59 ± 5.4 V respectively for sensor's output data. Fig. 4.8c shows the calculated $h_{\%}$ for the three SUTs, in particular $h_{\%}$ values found are: 53 ± 0.9, 60 ± 0.9 and 61 ± 0.70 respectively. Finally in Fig. 4.8d, is reported as reference, the force applied by the indenter, the values found for the three SUTs are: 0.26 ± 0.075 N, 0.39 ± 0.076 N and 0.43 ± 0.086 N, respectively.

The following section is adapted from the conference paper entitled “A Novel 3D Printed Sensorized Surgical Instrument to Characterize Pituitary Adenoma: Development and Initial Validation” published in *2024 IEEE International Workshop on Metrology for Industry 4.0 & IoT (MetroInd4.0 & IoT)* in July 2024 [196].

4.4.2 Prototype 2 – Working probe

The innovative aspect of the second prototype is a reduction of the external diameter of 33%, from 8.4 mm to 5.6 mm. Additionally, to hold the PCB in place, an oval eyelet of 4.6 mm was designed inside the rigid case to fit diagonally the sensor. On the top of the body a 3 mm cap was added to prevent the sensor from moving. The tip has been designed with 4 arms as a compromise between reducing the overall volume of the probe and the stability of the system to avoid structural instability when pressed. In the middle there is a circular base with a diameter of 2.5 mm to facilitate the positioning of the magnet and, once the tip is folded around the body it will be the contact point with the specimens. The length of the tip is 28 mm and the width of its four arms is 1.25 mm. Two tips were designed, one 0.45 mm and the other 0.75 mm in thickness. In addition, the tip was designed so that once folded and attached to the body, the initial distance between the magnet and the sensor d_0 is in the higher sensitivity trait, so to increase the sensitivity of the system during compression test. Fig. 4.9 shows the design of the new tip.

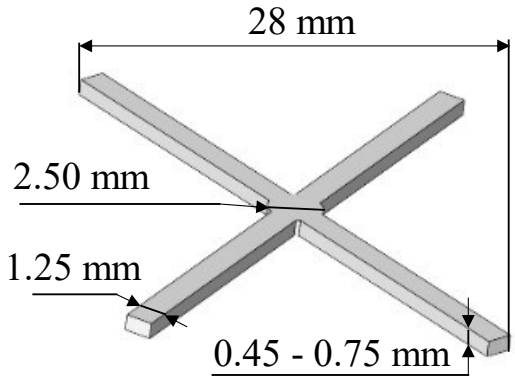

Fig. 4.9 Tip design. The tip has 4 arms, with a width of 1.25 mm and a thickness of 0.45 mm (P1, P2) and 0.75 mm (P3, P4). In the middle there is a circular base with a diameter of 2.50 mm and a total length of 28 mm.

4.4.2.1 TMR Characterization

With the new design of the probe, the magnetoresistive sensor was again characterized as a function of distance in a specific designed test. The board was positioned

inside the probe which was mounted on the micrometric slide. The tip was positioned on a flat surface right below the micrometric slide with the magnet attached to it (Fig. 4.10). The characterization consisted of a movement between the magnet and the probe from 0 to 7.2 mm, Distancing phase (DP), with steps of 100 µm, 300 µm and 600 µm and then back to 0 mm, Approaching phase (AP). The resulting curves are shown in Fig. 4.11. Both the DP and AP curves show an approximate linear trend from 0.5 mm to 3.0 mm, which tends to flatten out at the outer intervals. As already mentioned, from previous tests it was found that the TMR sensor has a measurement uncertainty of 4.7E-04 V. Data were interpolated using a 3rd degree linear model, DP model has an RMSE of 0.064 and an $R^2 > 0.99$ based on a sample size of 43, while AP model has an RMSE of 0.072, an $R^2 > 0.99$ based on a sample size of 41.Similarly to the previous results, only the AP curve was considered for its congruence with compression tests, to cope with the hysteresis of the sensor.

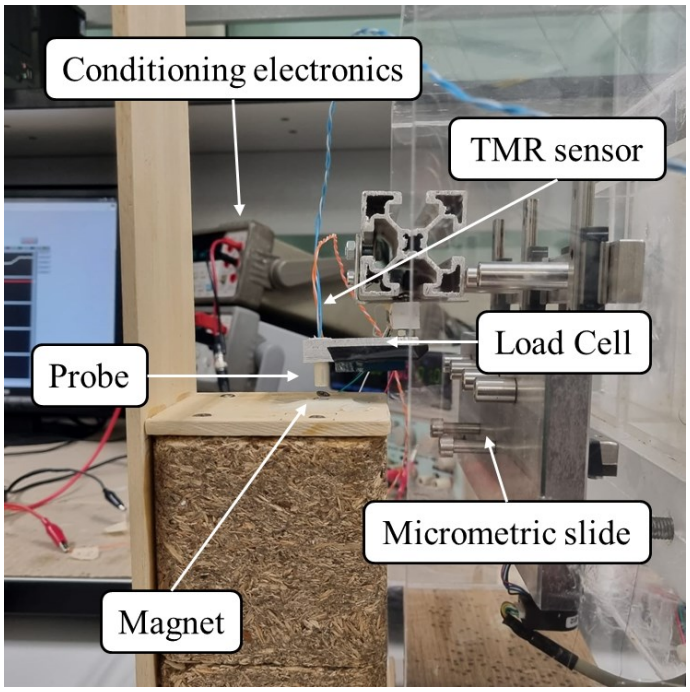

Fig. 4.10 The electronic setup. A Load cell is embedded in a displacement controlled micrometric slide and it measures the resistance of the specimen to compression, while the TMR sensor measures the variation of magnetic field as a function of the displacement.

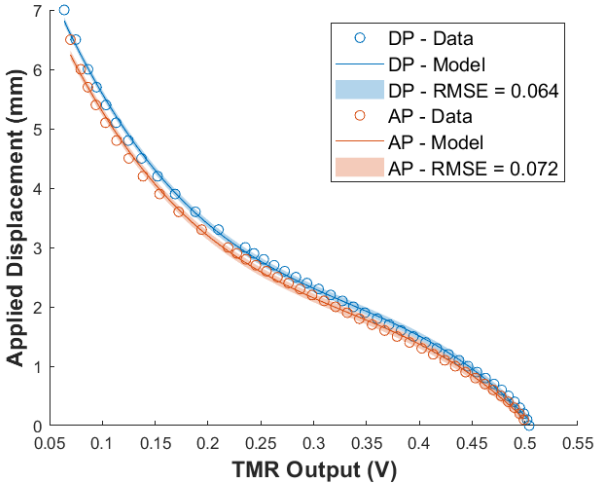

Fig. 4.11 TMR characterization. The characterization consisted of a movement between the magnet and the probe from 0 to 7.2 mm, Distancing phase (DP), with steps of 100 µm, 300 µm and 600 µm and then back to 0 mm, Approaching phase (AP). As already mentioned, from previous tests it was found that the TMR sensor has a measurement uncertainty of 4. 7E-04 V. Data were interpolated using a 3rd degree linear model, DP model has an RMSE of 0.064 and an $R^2 > 0.99$ based on a sample size of 43, while AP model has an RMSE of 0.072, an $R^2 > 0.99$ based on a sample size of 41.

4.4.2.2 Sample tested

The samples used in this work are the already mentioned three silicones, additionally, two softer samples were added: silicone Dragon Skin™ 30 (Smooth-On, Inc., USA) with a hardness of 30 Shore 00 and a specimen with a Shore 00 hardness of 10. The Shore A values of the first three silicone samples were experimentally converted to Shore 00 hardness using a 3rd degree linear regression model from two different data sets: C1[1]and C2[2]. The model has an RMSE of 2.6 (area highlighted in blue, Fig. 4.12). Specimen were converted for comparison purposes only for the sake of simplicity. The values of Shore 00 hardness of 45, 55 and 61 for the Shore A samples 8, 12 and 16 respectively. Fig. 4.12 shows the 3rd degree linear regression model used to determine the shore 00 hardness.

[1] https://www.apstpe.com/media/pdf/Shore-Hardness-Scales.pdf
[2] https://plantech.com/convert-different-durometer-shore-types/

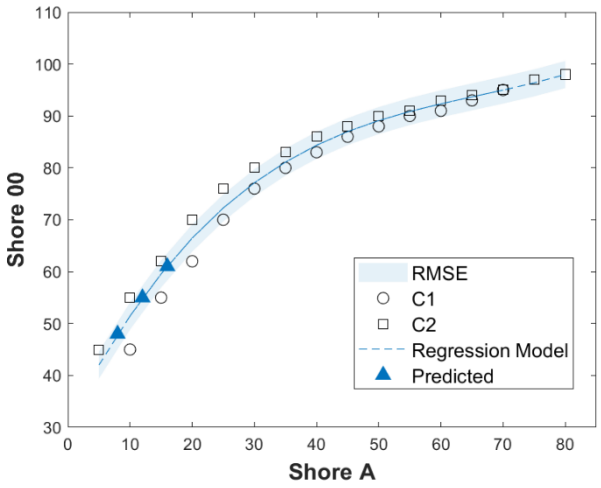

Fig. 4.12 Shore A to Shore 00 Calibration Curve. To compare results, the values of the Shore A samples were preliminary converted into Shore 00 hardness using a 3rd degree linear regression model with an RMSE of 2.6 (area highlighted in blue) using two different data set found: C1[1] and C2[2]. The values of Shore 00 hardness of 45, 55 and 61 for the Shore A samples 8, 12 and 16, respectively.

4.4.2.3 Results – Prototype 2

Indentation tests were performed to explore a correlation between different Shore 00 hardness materials with the deformation of the four tips. Fig. 4.13a and Fig. 4.13b show Shore 00 data as a function of Force (N) for P1 - P2 (0.45 mm tips) and P3 - P4 (0.75 mm tips) respectively, what emerges is that 0.45 mm tip has a lower scattering, especially when testing materials with a lower hardness. Indentation tests were performed twice for each combination of tip – specimen, for a total of 10 sets of data for each probe. Fig. 4.13c and Fig. 4.13d show Shore 00 data as a function of $h_{\%}$ for P1 - P2 and P3 - P4 respectively. Data confirm that the thinner tips have a lower scattering, in addition they have a greater sensitivity which makes them more suitable for the measurement of soft anatomical tissues, like PAs.

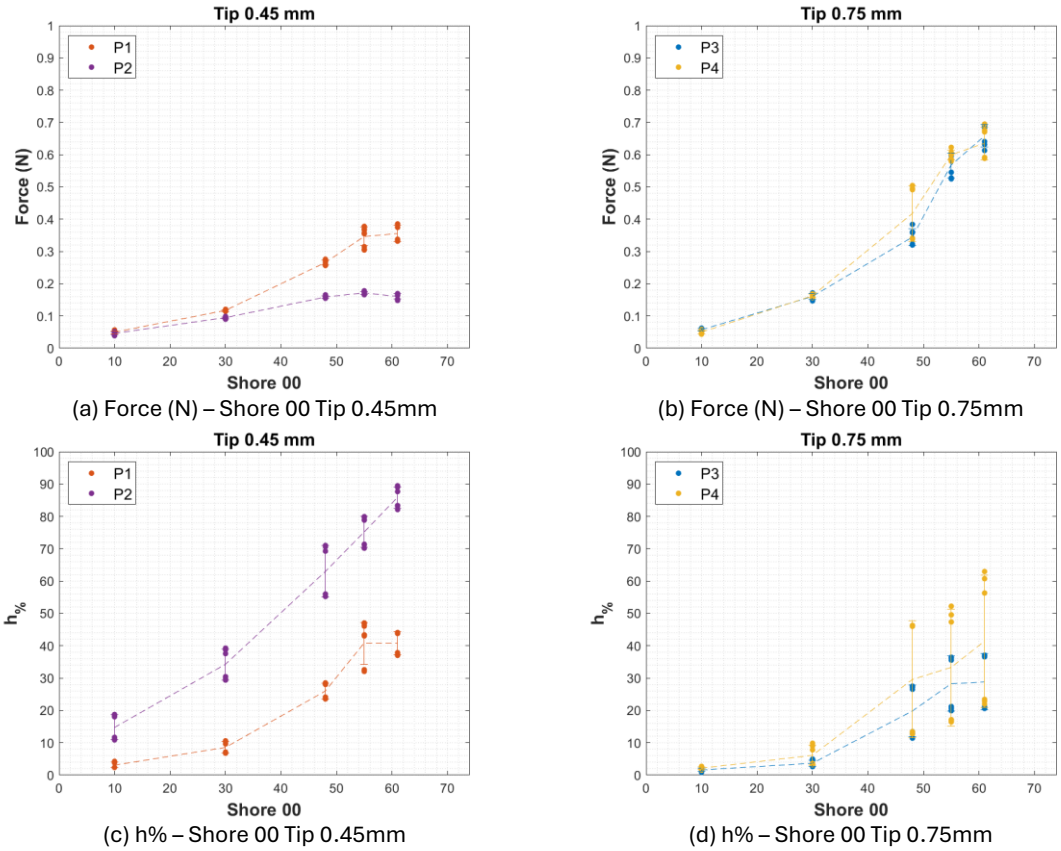

(a) Force (N) – Shore 00 Tip 0.45mm

(b) Force (N) – Shore 00 Tip 0.75mm

(c) h% – Shore 00 Tip 0.45mm

(d) h% – Shore 00 Tip 0.75mm

Fig. 4.13 The result obtained for the four probes: (a) and (c) report the result of P1 and P2 (probe with a 0.45 mm tip) for Force (N) and $h_{\%}$ respectively, analogously (b) and (d) for P3 and P4 (probes with a 0.75 mm tip). As a result, 0.45mm tips are more sensitive to lower values of hardness and their trend is closer to linearity than 0.75 mm tips, making the former more suitable for the measurement of pituitary adenoma hardness.

The same indentation test was conducted with a boiled egg white specimen for each of the four probes, both the force, and the $h_{\%}$ values were determined for each test as well. By fitting a linear regression model between the Force (N) and the Shore 00 and analogously between $h_{\%}$ and Shore 00 hardness, it was possible to determine the Shore 00 values for the boiled egg white specimen measured with each probe. Force data present a better repeatability from P1 – P2 and P3 – P4, especially for lower hardness. Preliminary Shore 00 values of the egg sample were calculated from the regression models obtained for each probe. Specifically, the MATLAB function *fitlm* was used to find a 3rd degree linear model for each probe to fit the data. In particular, an RMSE of 2.7 and R^2 of 0.98 were found for P1, an RMSE of 4.5 and R^2 of 0.95 for P2, an RMSE of 1.5 and R^2 of 0.99 for P3, and an RMSE of 2.6 and an R^2 of 0.98 for P4. Then, with the *predict* function, the value of the egg hardnesses were taken as the mean value for the tip with the same thickness P1-P2 and P3-P4, together with the standard deviation. The hardnesses obtained are 17 ± 3.0 for P1-P2 combined and 16 ± 6.4 for P3-P4 combined. The level of force reached while testing egg white specimen are similar to the forces found in literature reached when interacting with pituitary adenomas during a real

transsphenoidal surgery in the range of 0.1 to 0.5 N when interacting with soft tissues [199], while a mean values of 0.68 N for neurosurgical approaches [213]. This may indicate that the boiled egg white consistency is like the one of PAs. For the TMR sensor, the Shore 00 hardness values are obtained. Similarly, for TMR data linear model were fitted. In this case for P1 and P2 a 2nd degree linear regression with an RMSE of 4.0 and an R^2 of 0.96 for P1 and an RMSE of 3.4 and an R^2 of 0.97 for P2, while for P3 and P4 a 3rd degree polynomial regression with an RMSE of 5.2 and an R^2 of 0.93 for P3 and RMSE of 5.61 and an R^2 of 0.92 for P4. The combined egg hardnesses are 16.1 ± 2.02 Shore 00 hardness for P1-P2 16 ± 4.4 Shore 00 hardness for P3-P4. Fig. 4.14 shows the results for both the force data (circles) and TMR data (triangles). In addition, egg data measured during the first replicate with P4 were removed since they were considered outliers.

The low repeatability when comparing probes with the same tip thickness can be attributed to how the system was mounted, in fact, as shown in the TMR sensor characterization in Fig. 4.14, a minimal variation in d_0 corresponds to a large variation in sensor output. This variation is more visible with 0.75 mm. In fact, there is a variation of 23% between P3 and P4 while a variation of 10% between P1 and P2 when comparing force data while a variation of 47% between P3 and P4 while a variation of 11% between P1 and P2 when comparing $h_{\%}$ data.

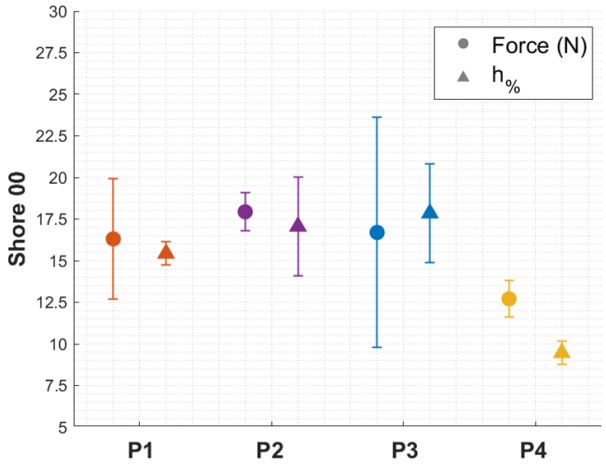

Fig. 4.14 Shore 00 Hardness of egg white specimen. The plot displays the Shore 00 of the egg specimen measured with the four probes. With the circles are reported the value obtained from the load cell, while with the triangles the values of the TMR sensor.

The following section is adapted from the paper entitled “Additive manufacturing of a mini sensor-based instrument to measure the hardness of pituitary adenomas” which will be submitted on IEEE Sensors Journal.

4.4.3 Prototype 3 – Optimized Probe

To further improve the design of the probe, a process characterization was carried out. In particular, in the following section it is described an optimization of the tip, which is the core of the sensorized instruments. The aim is to increase its sensitivity and repeatability.

4.4.3.1 The new highly deformable tip

The new design of the tip has the number of beams (N) varying, they are 15.00 mm in length and with varying width (w). The plate has a diameter of 3.20 mm, and the overall thickness of the tip (t) is uniform and equal to 0.45 mm as the best value in terms of sensitivity found in previous section of this chapter, the geometry of the new tip is shown in Fig 4.15a. In particular, to enhance the deformability of the beams, they are printed as a single line of material extruded by the nozzle (Fig. 4.15b). This print was obtained by studying the interaction of three different printing parameters: print speed (v_0), line width (w_0), and layer height (h_0), which is reported in the following sections.

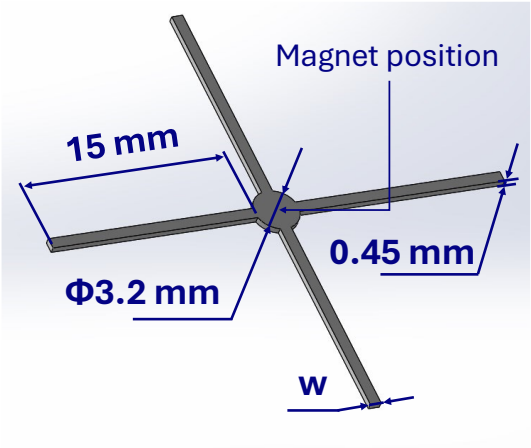

(a)

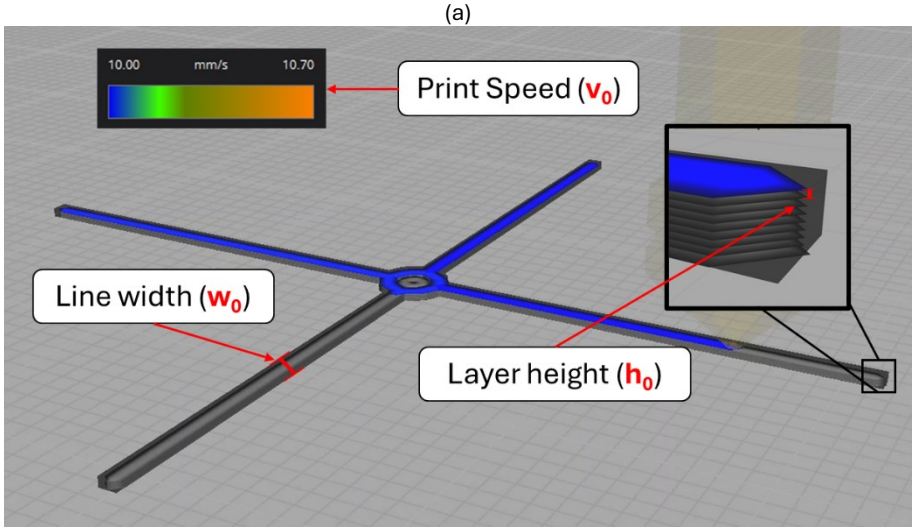

(b)

Fig. 4.15 The diameter of the circular base is 3.2 mm, the length of a single beam is 15 mm, while the overall thickness is 0.45 mm. The magnet is positioned in the middle of the circular base (a). To enhance the sensitivity of the tip, its beams are printed as a single line of material extruded by the nozzle (b).

4.4.3.2 Process Characterization of the tip

The beams of the tip represent the key features of the probe since the response of the sensor mostly depends on their flexibility. Accordingly, two experimental campaigns were conducted to properly design the probe. The first campaign aims at characterizing the printing process to identify how the process parameters influence the cross-section of the beams, and, in particular, the width (w) of the printed lines. The width was measured using an optical microscope by Mitutoyo (Fig. 4.16a), with its integrated software (Fig. 4.16b). The second campaign aims at the optimization of the tip geometry by investigating the correlation between width (w) and the number of beams (N) and the behavior of the probe in terms of sensitivity, linearity and uniformity amongst the fabricated probes.

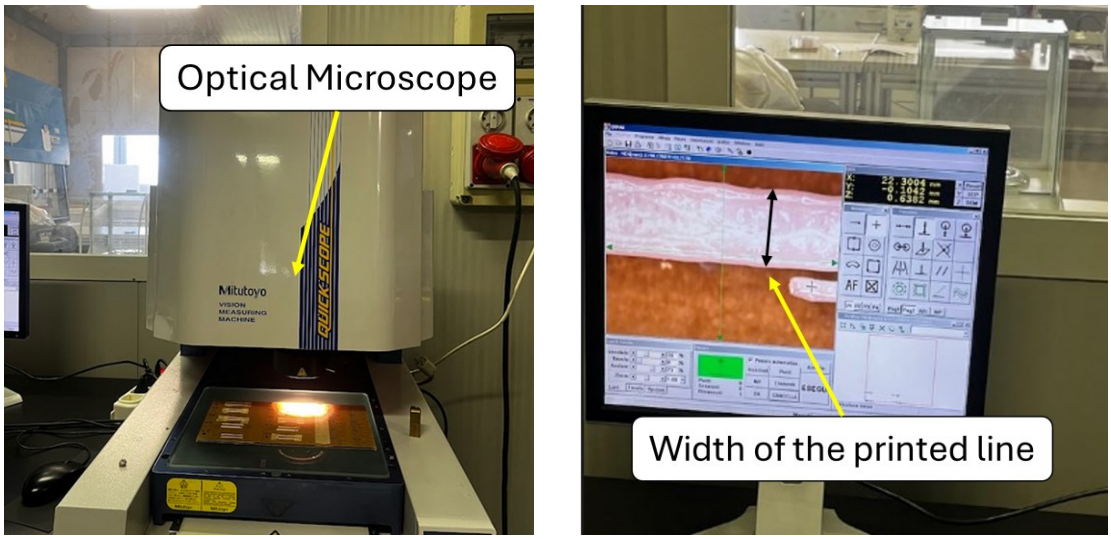

(a) (b)

Fig. 4.16 Each width of the printed lines was measured with the Quick Scope optical microscope by Mitutoyo (Mitutoyo Corporation, Japan) (a), the measurements were performed using its embedded software (b).

4.4.3.2.1 Process characterization

Three process parameters were considered to characterize the process: layer height (h_0), nominal line width (w_0) and print speed (v_0). Their values were chosen based on default print settings (w_0 = 0.40 mm, v_0 = 25 mm/s) and preliminary tests. In particular, they showed that w_0 should vary in the range of 0.20 ÷ 0.80 mm (approximation of the values suggested by the slicing software). Moreover, printing becomes unstable (i.e. discontinuous extrusion) for v_0 > 50 mm/s in every combination of the other process parameters.

Accordingly, different combinations of the parameters were progressively tested to print single lines 30 mm in length and w_0 in nominal width (Table 4.3 and Fig. 4.17). For handling reasons, multiple layers of lines were printed to a height of 0.90 mm and then measured in width. Results were evaluated in terms of process feasibility, line width and material flow through the nozzle. In particular, the process feasibility was evaluated in terms of material extruded from the nozzle and, in the case of discontinuous extrusion, the process was considered failed. Moreover, the widths of the sample were measured in three different positions and mean value (w) and standard deviation ($w_{st.dev}$) were calculated.

Results showed the feasibility limits of the process and its repeatability. Moreover, they were used to characterize the effects of the process parameters (h_0, w_0, v_0) on the width (w) of the printed line.

Table 4.3 Characterization tests. Summary of the tested parameters.

Printing parameter	Values	Units
Layer height (h_0)	0.05 – 0.10 – 0.15	mm
Line width (w_0)	0.20 – 0.26 – 0.30 – 0.40 – 0.50 – 0.60 – 0.70 – 0.80	mm
Print speed (v_0)	2 – 5 – 15 – 25 – 37.5 – 50	mm/s

Fig. 4.17 shows that, in general, a higher print speed (v_0) leads to a discontinuous extrusion of material for mid or low values of nominal line width (w_0). Given the not feasibility of the process in those conditions, failed tests were excluded in the following analysis.

The ratio w/w_0 in Fig. 4.18 shows that the width of the printed line (w) is different from the nominal one (w_0) as other process parameters change. In particular, the higher the print speed (v_0), the lower the ratio w/w_0. This shows that w_0 does not control, completely nor partially, the actual line width (w) of the printed line. Moreover, it can explain the effect of the print speed (v_0) on material extrusion in Fig. 4.17. In fact, as the print speed increases, the 3D printer does not successfully compensate for the line width (w) which, at the highest speed, becomes too low so compromising the adhesion of the material on the underlying layer. Hence, discontinuous extrusion occurs.

For these reasons, the results were analyzed to determine how to effectively control the width of the printed lines which are directly correlated to the actual 3D printed geometry of the tip beams. Then, a regression model of the process able to predict the line width (w) as a function of the process parameters was developed.

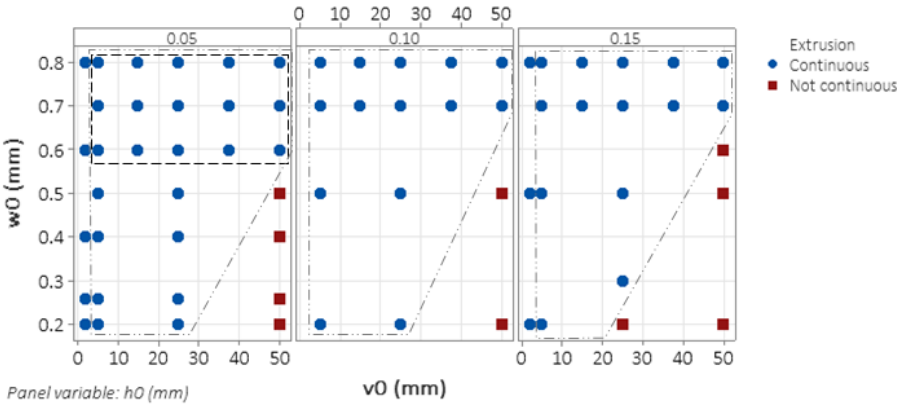

Fig. 4.17 Characterization tests. Summary of the tests conducted to characterize the process on the variation of the layer height (h_0), line width (w_0) and print speed (v_0). The polygonal and rectangular boxes represent respectively the domains of the general and local regression models for line width control.

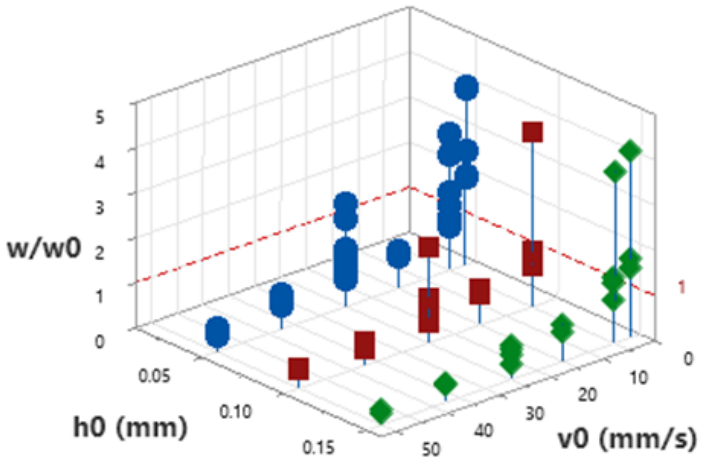

Fig. 4.18 Ratio w/w_0. Comparison between nominal (w) and experimental (w_0) width values as layer height (h_0) and print speed (v_0) changes.

To identify the process window of the regression (i.e. the dataset to be used), some preliminary considerations were drawn on the behavior of the width of the printed lines. Fig. 10 reports the average width value (w) and its standard deviation ($w_{st.dev}$) in each line printed. In particular, it shows that a lower sprint speed (v_0) leads to less uniform lines (Fig. 19), especially for v_0 = 2 mm/s. Therefore, these tests were excluded from the regression analysis. Moreover, when the process is limited to h_0 = 0.05 mm and v_0 = 5 to 50 mm/s, the width w_0 has a lower or negligible influence on w (Fig. 4.19a) and $w_{st.dev}$ is the lowest (Fig. 4.19b). Hence, the process is more robust, and printed lines are more uniform in this range of parameters.

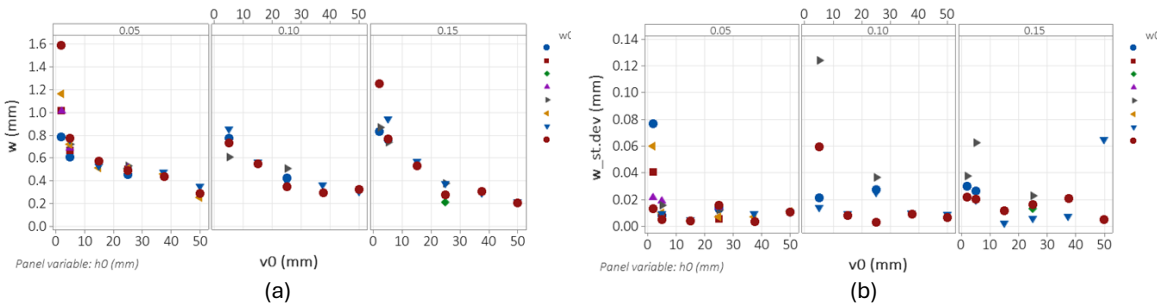

Fig. 4.19 Line average width (w) and variability ($w_{st.dev}$). a) Average width (w) and b) Standard deviation ($w_{st.dev}$) of the width of the 3D printed lines as other the process parameters nominal width (w_0), layer height (h_0) and print speed (v_0) change. Standard deviation is estimated on the repeated measures of each single line printed.

Based on previous considerations, two regression models were developed using two different subsets of data. The first dataset is wider (Fig. 4.17, dot-dashed boxes) and contains all feasible tests where the process is sufficiently uniform, that is all tests conducted at v_0 = 5 to 50 mm/s, failed test excluded. The second one is local (Fig. 4.17, dashed box) and contains the tests where the process is more uniform and robust, that is h_0 = 0.05 mm, w_0 =

0.60 to 0.80 mm and v_0 = 5 to 50 mm/s. For each domain, a regression model was identified, named general and local models. An initial polynomial model including grade 3 terms and grade 2 interactions was considered. Then, the corrected Akaike information criterion (AICc) was used to exclude the non-significant terms (alpha-value = 0.05) and to develop the final regression models.

The general regression model (w_G) is reported in (2) and in Fig. 4.20 and has an R^2 = 0.89. It is a grade 3 polynomial function in v_0 and includes all other tested parameters as interactions between h_0 and both v_0 and w_0. Moreover, print speed (v_0) mostly influences the final width (w) while other parameters have a minor influence (Fig. 4.20a and Fig. 4.20b). This is in accordance with what was previously discussed about the influence of the process parameters (Fig. 4.19 and Fig. 4.20).

$$w_G = 0.86 - 0.0328*v_0 + 0.00098*v_0^2 - 0.054*h_0 v_0 + 0.94*h_0 w_0 - 0.000010*v_0^3 \quad (2)$$

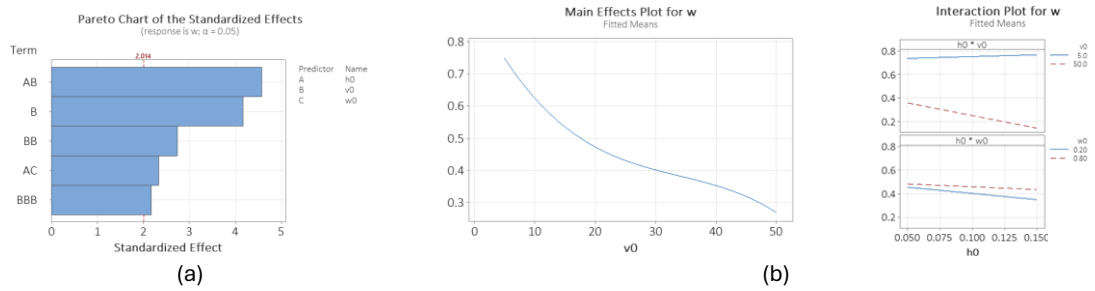

(a) (b)

Fig. 4.20 Global regression model. Characterization of the influence of the process parameters on the line width (w) in the process window: h0 = 0.05 ÷ 0.15 mm, w0 = 0.2 ÷ 0.8 mm, v0 = 5 ÷ 50 mm/s, failed test excluded. a) Pareto chart and b) Main effects and interaction plots of the regression model.

The local regression model (w_L) is reported in (3) and in Fig. 4.21, has an R^2 = 0.97. Differently from the general regression model, the local model is a 3rd degree polynomial function in v_0 only (Fig. 4.21a). Therefore, print speed (v_0) is the only parameter that influences the final width (w) while other parameters have no effects (Fig. 4.21b). This is compliant with the robustness of the process that was previously observed when h_0 = 0.05 mm (Fig. 4.20a and Fig. 4.21a).

$$w_L = 0.94 - 0.0455 \cdot v_0 + 0.00153 \cdot v_0^2 - 0.000018 \cdot v_0^3 \quad (3)$$

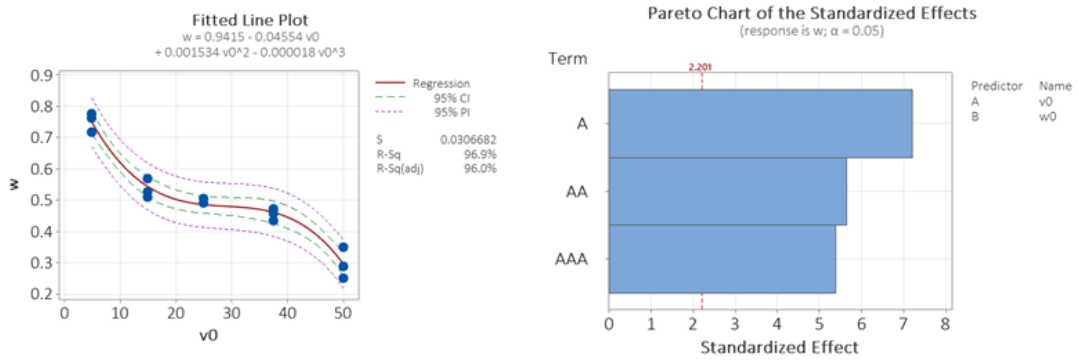

(a) (b)

Fig. 4.21 Local regression model. Characterization of the influence of the process parameters on the line width (w) in the process window: h0 = 0.05 mm, w0 = 0.60 ÷ 0.80 mm, v0 = 5 ÷ 50 mm/s. Plots of the regression model (a) and Pareto chart (b).

The regression models were validated by 3D printing a set of tips using 5 different print speeds (v_0 = 5, 10, 25, 37.5 and 50 mm/s) with constant nominal line width (w_0 = 0.80 mm) and layer height (v_0 = 0.05 mm). According to the design of the tip described previously, the thickness (t) of the tips is equal to 0.45 mm and 3 different numbers of beams (N = 3, 4 and 5) were considered.

The width of the printed tips was measured three times for each beam and the mean value (w) and its standard deviation ($w_{st.dev}$) were estimated. Results were compared with the values predicted by the global (w_G) and local (w_L) regression models. In particular, $w \pm 3 \cdot w_{st.dev}$ was adopted to consider the 99.7% of variability. Tests at v_0 = 37.5 mm/s and 50 mm/s were excluded because it was not possible to successfully remove them from the build plate. In fact, the smaller width (w) and thickness of the part (t) resulted in a part cross-section too weak to handle. Results (Table 4.4) show that the prediction of both models falls within 99.7% of the measure variability, even though they show an overestimation tendency. This could be related to the lower thickness of the part (0.45 mm) than the one used to collect the data for the model (0.90 mm). In fact, a greater height increases the number of misaligned layers leading to a greater width of the part and, thus, to an overestimation of the line width (w).

Table 4.4 Models validation. Width of the printed tips (w) compared with the prevision of the global (w_G) and local (w_L) regression models.

v0	Tips (mm)	Prediction (mm)		Difference (mm)	
(mm/s)	w ± 3·wst.dev	wG	wL	wG – w	wL – w
5	0.63 ± 0.18	0.74	0.75	0.12	0.12
10	0.50 ± 0.12	0.63	0.62	0.13	0.12
25	0.41 ± 0.05	0.47	0.48	0.05	0.06

Accordingly, the previous discussion and considerations can be summarized as follows:

- The sprint speed (v_0) is the parameter that most influences the width of the printed lines (w). A speed range of 5 ÷ 50 mm/s can be adopted for a layer height h_0 = 0.05 mm and nominal line width w_0 of 0.60 ÷ 0.80 mm. As h_0 increases or w_0 decreases, the maximum print speed (v_0) should be lowered.
- The nominal line width (w_0) parameter marginally controls the width of the printed line (w). Moreover, if a layer height h_0 = 0.05 mm is adopted, the influence of w_0 is not statistically significant.
- At higher print speed (v_0), the lower width (w) of the lines could limit the handling of the part (in particular, its removal from the build plate). Hence the number of layers (i.e. thickness of the part) should be increased to enhance its resistance.
- A lower layer height (h_0) leads to more uniform printed lines. Moreover, when h_0 = 0.05 mm and v_0 = 5 ÷ 50 mm/s, the process is more robust (i.e. independent from w_0), and the line width can be controlled through the print speed (v_0) only.
- The local regression model developed is more accurate and robust and it should be preferred to model the influence of print speed (v_0) on the line width (w) of the 3D printed lines.
- As the number of layers increases, the misalignment of the printed lines may lead to greater overall part width (w). Therefore, when the part thickness is different to the one used to develop the regression model, a final measurement should be performed to verify the actual part width. Otherwise, the regression model could be extended including the influence of the part height.

4.4.3.2.2 Tip optimization

The optimization of the tip design was performed using the tips printed to validate the regression models. Accordingly, 3 values of print speed (v_0) with 3 numbers of beam (N) and 2 replicates for each design were tested (Table 4.5 and Fig. 4.22) for a total of 18 tips. Fig. 4.23 shows the assembled tips.

Table 4.5 Tip design tests. Parameters adopted to test and optimize the design of the tip.

Tip design	Values	Units
Print speed (v_0)	5 – 10 – 25	mm/s
Beams (N)	3 – 4 – 5	-
Thickness	0.45	mm
Layer height (h_0)	0.05	mm
Line width (w_0)	0.80	mm

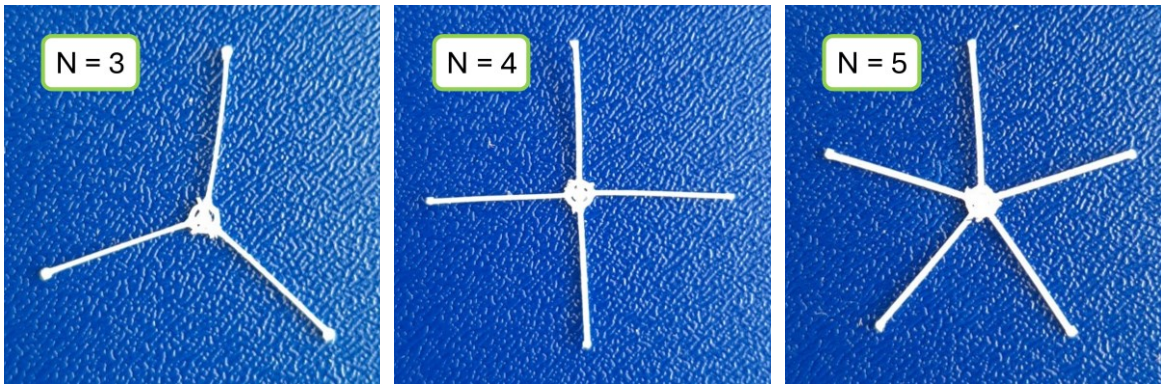

(a) (b) (c)

Fig. 4.22 Examples of Printed tips. Printed tips with different number of beams (N), N = 3 (a), N = 4 (b) and N = 5 (c).

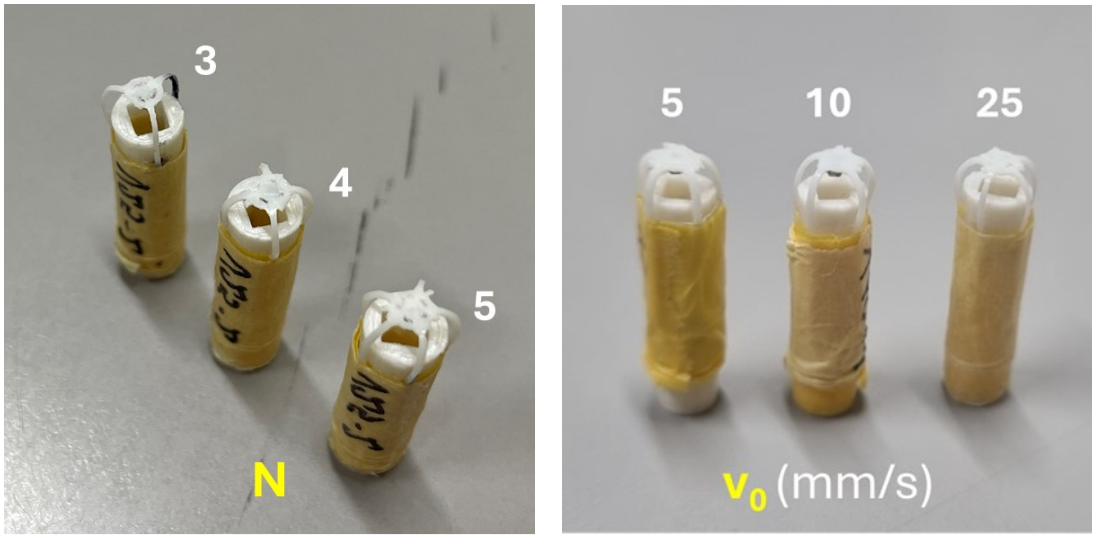

(a) (b)

Fig. 4.23 Probes assembled. Probe with different number of beams N = 3,4 and 5 (a). Probes with N = 5 printed with different print speed v_0 = 5, 10 and 25 mm/s (b).

4.4.3.3 Indentation tests

4.4.3.3.1 The assembly equipment

Previous tip prototypes revealed how the small sizes of the device make it difficult to correctly position the magnet on the tip. Therefore, equipment to align and position the magnet on the tip was designed and 3D printed in PLA on Ultimaker 3 extended with a 0.4 mm nozzle. The device uses a magnetic field to orientate the small cubical magnet with the center tip. In

particular, the equipment (Fig. 4.24) consists of a base which holds 3 cylindrical magnets with a diameter of 5.6 mm and a height of 9 mm (Fig. 4.24a and Fig. 4.24b), and a tip holder which aligns the tip with the axis of the cylindrical magnets. The tip holder can be customized according to the dimensions and the number of beams (N) of the tip. The assembly procedure involves placing the tip on the holder and applying a drop of acrylic glue onto the circular base and, finally, dropping the small cubic magnet. By gravity and magnetic fields, the cubic magnet self-aligns at the center of the circular plate.

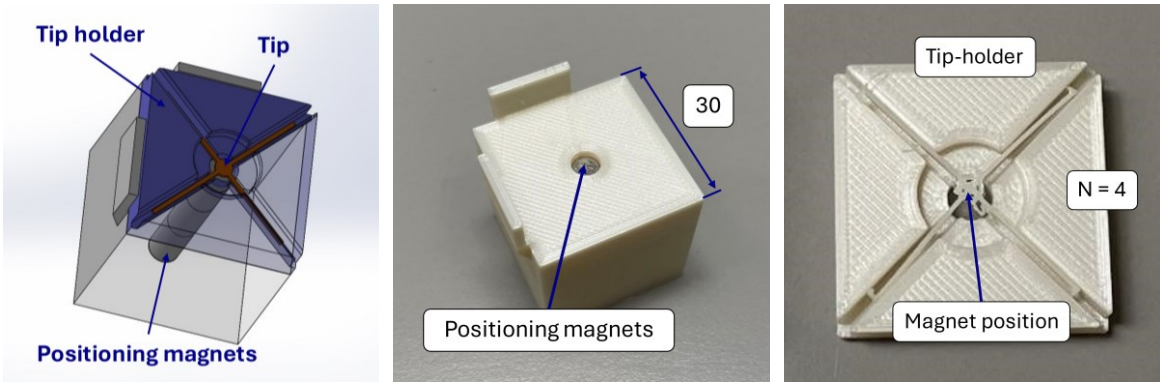

(a) (b) (c)

Fig. 4.24 Positioning equipment. The equipment is designed to guarantee a repeatable positioning of the magnet in the middle of the tip, on the left the CAD design (a) on the right the instrument printed (b and c).

4.4.3.3.2 TMR Characterization

Before the experimental campaign, four new TMR sensors were characterized to find a correlation between the sensor output, expressed in volts, and the magnet-to-sensor distance, expressed in millimeters. In particular, the PCB with TMR was mounted in the rigid case without the tip. Frontally, a cubic magnet was mounted with the negative polarity facing the sensor, as shown in Fig. 4.25. The characterization procedure consists of positioning the rigid case in contact with the magnet; then the magnet moves at its initial position at a distance of 10 mm from the contact point. Then a stepped displacement is imposed on the slides so that the magnet moves towards the magnet of 0.10 mm each step until contact occurs again. The couple TMR output and distance were recorded at each to characterize the sensor. In this study, 4 different TMR sensors were characterized and used in the tests (Fig. 4.26). As already mentioned, from our previous tests, the measurement uncertainty for the TMR sensor is 4.7E-04 V and was considered to be the same for each TMR sensors tested.

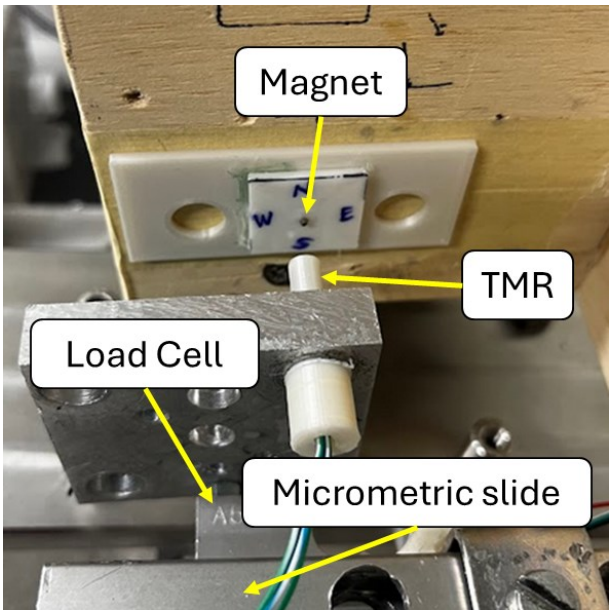

Fig. 4.25 TMR characterization setup. Equipment for the characterization test on the TMR sensor.

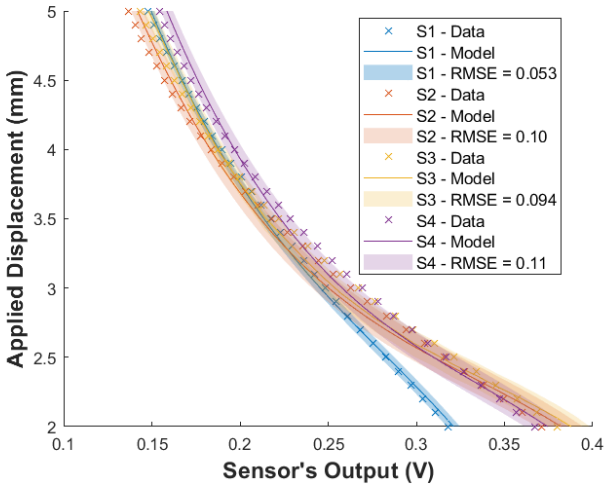

Fig. 4.26 TMR characterization curve. Results of the characterization tests performed on the TMR sensors. As already mentioned, from our preliminary tests, the TMR sensor used has a measurement uncertainty of 4.7E- 04 V, while the resolution of the micrometric slide is 0.010 mm. The four TMR sensors data (S1, S2, S3 and S4) were interpolated using a 3rd degree linear model. S1 has an RMSE of 0.053, S2 has an RMSE of 0.10, S3 has an RMSE of 0.094 while S4 has an RMSE of 0.11, the R^2 for each model is > 0.99. Regression models were performed based on a sample size of 71 for each sensor.

4.4.3.3.3 Samples preparation

Similar to what was presented earlier in the second prototype section, to facilitate a comparison between the samples, it was necessary to bring them onto the same hardness scale, specifically, in this case it was used the Shore 000 scale, which differently from the Shore 00, is more suitable for softer materials.

The samples were then measured with a Shore 000 durometer by Axiotek (Axiotek S.r.l., Italy), as shown in Fig. 4.27a. The instrument has a measurement uncertainty of 1 Shore 000 hardness point.

Silicone samples having different hardness from 66 ± 1 to 83 ± 1 Shore 000 hardness (Fig. 4.27a) together with a Marshmallow with a measured Shore 000 hardness of 51 ± 1, and a boiled egg white sample with a hardness of 52 ± 1 Shore 000 hardness (Fig. 4.27b) were used to characterize the probes during indentation tests. The egg white was obtained by cooking in 113 g of raw egg white in microwave at 800 W for 70 seconds, then the sample was obtained by manually cutting a square in the center of the boiled egg white.

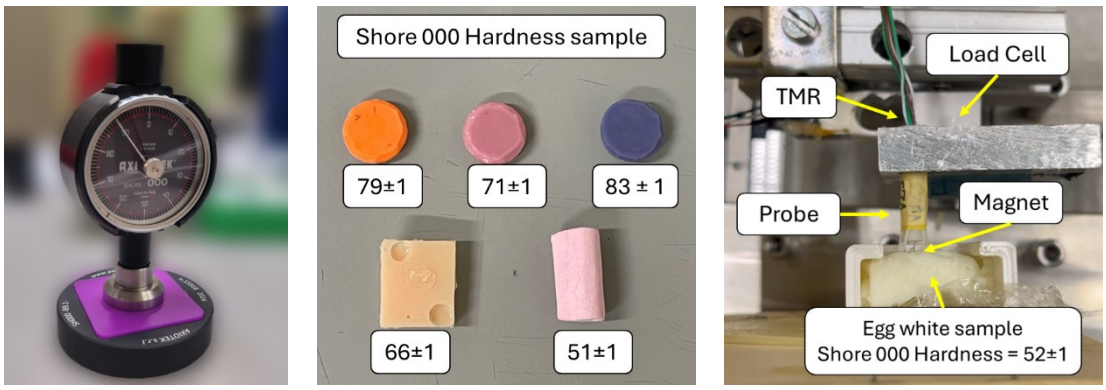

(a) (b)

Fig. 4.27 The Shore 000 durometer, the silicone samples with the Marshmallow (a) The probe pressed against the egg-white sample, during indentation tests (b). The durometer has a measurement uncertainty of 1 point on the Shore 000 scale.

4.4.3.3.4 Results of Indentation tests

The typical profiles of contact Force and tip distance signals detected during indentation tests are reported in Fig. 4.28. The force, Fig. 4.28a, rapidly reaches the peak during indentation, then it decreases while the probe holds contact. When the probe returns to the initial position, the force becomes negative and then it settles to the null value. The initial peak of the force may be influenced by dynamic effects and the following reduction derives from an assessment of the system (as discussed below). Moreover, the negative force values indicate that the probe is temporarily pulled, probably due to a temporary adhesion between the surfaces of the probe and the sample. The result of the TMR sensor, shown in Fig. 4.28b as the output in V and in Fig. 4.28c as the magnet position, i.e. the values obtained by converting the TMR data to mm, is similar to the force profile.

The results of the tests were compared using the force (F) at the end of the hold phase (matt symbols in Fig. 4.28a) and the compression of the tip ($h_{\%}$). In particular, $h_{\%}$ expresses the

compression of the tip and is calculated using equation (3) where d_0 is the displacement imposed at the probe and d is the difference between the initial and the final distances of the tip from the TMR sensor (respectively empty and matt symbols in Fig. 4.28b and Fig. 4.28c, as reported in (1).

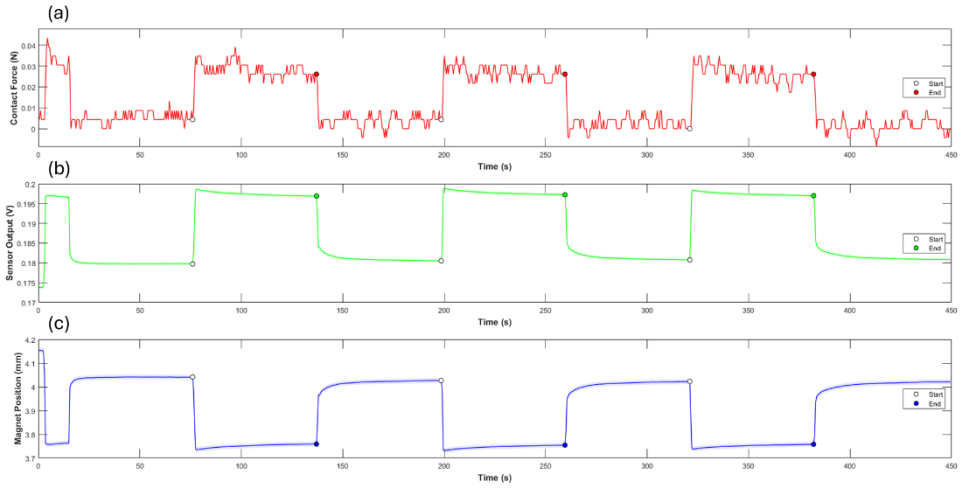

Fig. 4.28 Results of the indentation test. (a) "Contact Force" on the tip detected by the load cell and , "Sensor Output" and the "Magnet Position", detected by the TMR sensor. (b and c).As already mentioned, from previous tests it was found that the TMR sensor has a measurement uncertainty of 4.7E-04 V, while the micrometric slide has a resolution of 0.010 mm.

The results of the experiments are reported in Fig. 4.29 and Fig. 4.30 respectively in terms of the average values of F and $h_{\%}$ upon the 3 indentations. Moreover, data were linearly interpolated as a function of the hardness (dashed lines) and RMSE of the regressions was estimated (shaded area). Finally, the regressions were inversely used to estimate the egg hardness through the experimental results (F and $h_{\%}$) and the prediction was compared with the actual hardness of the white egg sample (52 ± 1 Shore 000 hardness). The summary of the regressions is reported in Table 4.6.

The sensitivity of Force (F) to the hardness of the samples (Fig. 4.29) depends on the number of beams (N) and the print speed (v_0). This becomes more evident if the Force slopes for N = 5 are compared. In fact, the force required to compress the tip depends on its stiffness which, in turn, depends on N and w which is influenced by the v_0 as reported in Fig. 4.29 and Fig. 4.30. Moreover, the response is almost linear and RMSE values are small.

The sensitivity of tip deformation ($h_{\%}$) to the sample hardness (Fig. 4.30) depends less on the tip design and makes this index generally more robust than the tip design. This is confirmed by Fig. 4.31 which compares the actual hardness of the white egg sample with the ones predicted by the regression models. In particular, the values predicted using $h_{\%}$ (Fig. 4.31b) are more precise and less variable than the ones obtained using force data

(Fig. 4.31b). On the contrary, linearity and RMSE depend on the tip design (Table 4.5). In particular, the most performing tips are the ones printed with a speed v_0 = 10 mm/s which have the strongest linear trend (i.e. highest Adj. R^2) and, in cases of N = 4 and 5, the lowest RMSE. Furthermore, the error of these two probes in predicting the hardness of boiled white egg is 0.80% and 3.5% respectively. Finally, the indentation force during white egg tests is lower than 0.05 N, which is slightly lower but comparable with data present in literature [199,213]. This validates the capability of the probes to characterize the hardness of a biological tissue-like material. Comparing all tested cases, the tip deformation $h_{\%}$ = 0 corresponds to a Shore 000 hardness of approximately 50. This value represents a lower limit for the application of the probe, a limit that probably can be overcome by increasing the flexibility of the tips.

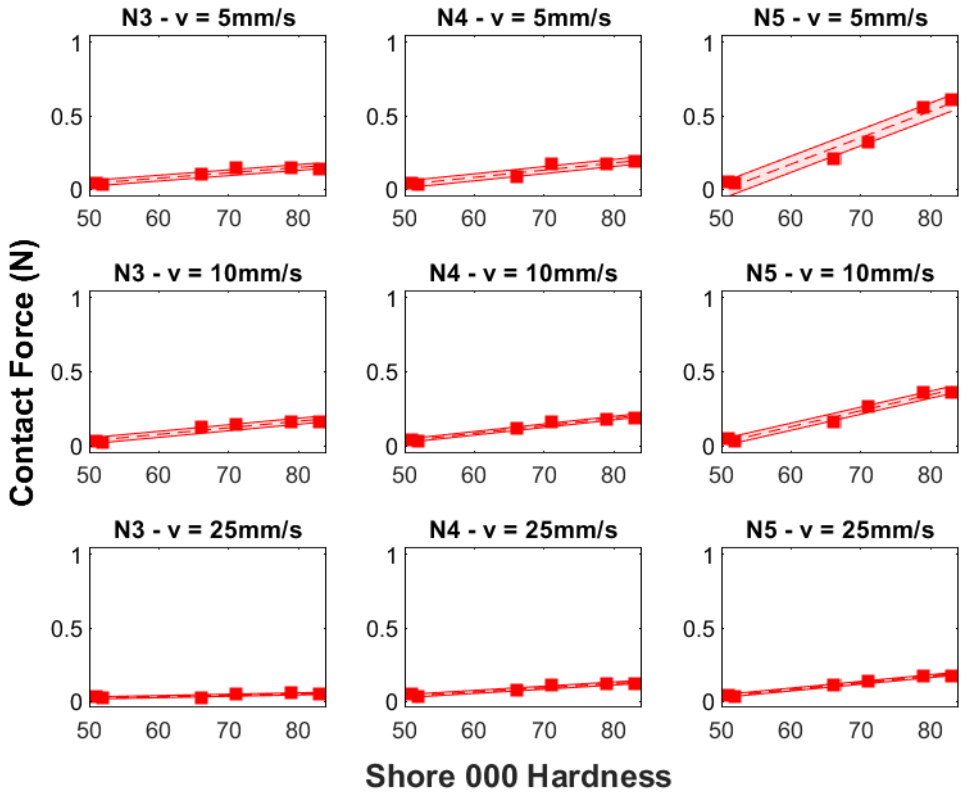

Fig. 4.29 Indentation test – Force (F) results. The contact force between the probe and the samples as the material hardness, number of beams (N) and printing speed (v_0) change. The dashed lines represent the linear regression model, colored areas are the RMSE.

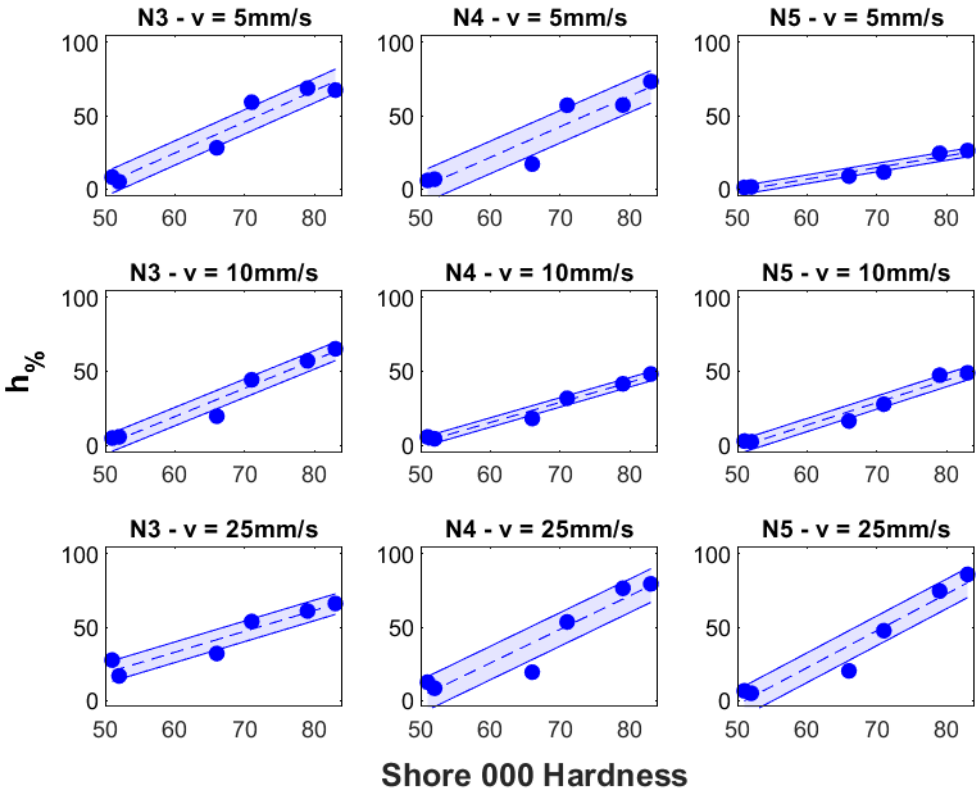

Fig. 4.30 Indentation test – Compression ($h_{\%}$) results. Compression of the tip as the material hardness, number of beams (N) and printing speed (v_0) change. The dashed lines represent the linear regression model, colored areas are the RMSE.

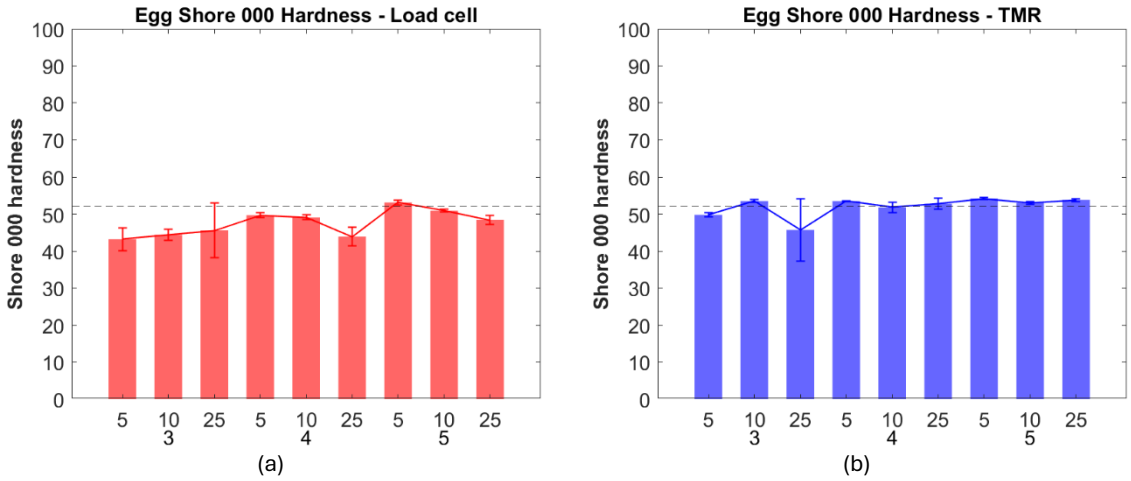

Fig. 4.31 Comparison of the measured hardness of the boiled egg white (Shore 000 hardness 52 – dashed line) with the values predicted using the trends of the contact force - F (a) and the tip compression - $h_{\%}$ (b).

Table 4.6 Regression Model - Load Cell: in this table are reported the most important results obtained with the regression model, obtained from Load Cell data. m = slope of the regression model; adj. R^2 = adjusted R^2; RMSE = Root Mean Square Error; Pred. Sh000 = Predicted Shore 000 hardness of the Egg sample from the Linear regression model; Δ% = percentage variation between the measure obtained with the Shore 000 hardness durometer and the value predicted from linear models

Tests		Contact Force – F, load cell					Deformations - $h_{\%}$, TMR				
N	v_0	Model			Pred. Sh000		Model			Pred. Sh000	
		m	adj. R^2	RMSE	Egg	Δ%	m	adj. R^2	RMSE	Egg	Δ%
3	5	0.0030	0.80	0.019	43	-17%	2.1	0.88	9.4	50	-4%
3	10	0.0040	0.89	0.020	44	-15%	2.0	0.92	7.1	54	3%
3	25	0.0010	0.58	0.0080	46	-12%	1.2	0.83	7.3	46	-12%
4	5	0.0050	0.82	0.027	50	-5%	2.1	0.81	13	54	3%
4	10	0.0050	0.96	0.012	49	-6%	1.4	0.96	3.7	52	0%
4	25	0.0030	0.93	0.008	44	-16%	2.3	0.82	13	53	2%
5	5	0.018	0.93	0.063	53	2%	0.82	0.91	3.3	54	4%
5	10	0.011	0.96	0.027	51	-2%	1.5	0.93	5.1	53	2%
5	25	0.0040	0.97	0.0090	48	-7%	2.6	0.89	12	54	4%

The results and discussion can be summarized as follows:

- The indentation force suggests that relief and sticking effects may occur between the probe and the sample. This may be related to the couple of materials and needs to be verified when actual tissues are indented.
- The index $h_{\%}$ is more robust than force in the prediction of the sample hardness. Therefore, the probe that has been presented is preferable to load cells for this application.
- Tips printed with a speed v_0 = 10 mm/s show a more linear response of $h_{\%}$ to the tissue hardness.
- The best performance in terms of linearity and low RMSE of $h_{\%}$ was obtained with the tip having N = 4 beams and printed with speed v_0 = 10 mm/s. Comparable results were achieved with N = 5 and v_0 = 10 mm/s.
- Overall, the developed probes are capable of predicting the hardness of materials in the range of 51 ± 1 to 83 ± 1 Shore 000 hardness. Outside this range, the tested probes are not usable.

4.5 Conclusions

The design of the third faced challenging aspects deriving from its application, the manufacturing process and the measurement performances. In particular, the probe has to be inserted through the nostril which imposes a maximum width of 4.00 to 5.00 mm. Moreover,

the flexibility required by the tip imposes the fabrication of features having sub-millimetric dimensions.

The first prototype results show a high repeatability of the tests with a mean variation for the three specimens tested < 1%, underling that the system can discern the different hardness of materials, even if at that stage its diameter is too high.

The innovative design of the second prototype reduces the overall dimension of the probe so to fit within the nasal cavities. In fact, the previous version had a diameter of 8.4 mm, while the new has a diameter of 5.6 mm. The two parts of the probe: the body, and the tip, were fabricated through FFF additive manufacturing technology, respectively in PLA for stability and TPU for deformability. Two different tips with a thickness of 0.75 mm and 0.45 mm were evaluated. In particular, the 0.45 mm tip revealed a lower scattering of the measures and the Shore 00 hardness for the egg white specimen was measured 16 ± 2.02.

The development of the third prototype focused its attention on the characterization of the printing process to determine how to control the dimensions of the part. Then, different designs of the probes were fabricated, tested and evaluated, in order to find the optimal design.

The results achieved are very promising and the probe will be further developed by testing real biological tissue to evaluate its performance and validate it in the surgical field. Moreover, some other aspects require further improvements. The first is related to the range of the tissue hardness that can be tested. In fact, the results showed a lower limit for the design here considered. Therefore, more sensible tips should be tested to overcome this limit. Moreover, the current overall width of the probe is slightly larger than the requirements. Current dimensions are mostly determined by the PCB board and the printability of the case, but not the tip. At the moment, board and case are not crucial for the development of the probe, moreover, other fabrication solutions can be considered for their miniaturization before the industrialization of the product.

Chapter 5

Conclusions and Future Studies

The endoscopic transsphenoidal approach (ETA) is a novel approach used by both neurosurgeons and otolaryngologists to treat pituitary adenoma, a tumor that grows from the pituitary gland. It is well known that this surgery has a steep learning curve and requires a certain level of dexterity and hand-eye coordination to be performed. The procedure starts by inserting surgical instruments from one of the nostrils. Then, surgeons pass through the nasal cavity and approach the sphenoid sinus, where the dissection of the sphenoid bone starts, in order to expose the pituitary tumor, and then be able to remove it. Two of the most delicate aspect of the surgery are the handling of the arachnoid membrane, which covers the tumor, and choosing the best strategy to remove the adenoma, since the surgical approach changes according to its hardness, which is difficult to predict during the preoperative planning phase. The surgery can be considered successful only if the whole tumor is removed. Otherwise, it could grow back from its remnants, meaning that the patient would have to return to the operating room. Moving the arachnoid membrane can be complex, due to its fragility. Surgeons must exercise caution when moving it to search for any tumor residue. In particular, inexperienced surgeons must learn how to perform such maneuvers safely during tumor removal, since tearing the arachnoid membrane is associated with the potentially life-threatening complication risk of post-operative CSF leak.

The aim of this thesis was to enhance the learning experience for surgeons who perform the ETA surgery. To do so, two research were conducted. The first research consisted in the development of an innovative sensorized training model, with a unique feature: the reproduction of the arachnoid membrane. The goal was to develop an alternative to classical training, so that less experienced surgeons could learn in a safe environment with real-time feedback, and more experienced colleagues could evaluate whether they are ready or not to enter the operating room. The second research consisted in the development of a surgical instrument to help surgeons to characterize the type of pituitary adenoma intraoperatively, and therefore to determine the best strategy for its removal.

The research began with a comprehensive, up-to-date, state of the art analysis of the types of training that are currently available to surgeons. Besides training in the operating room, the training solutions found were divided into four categories: 1) cadaveric head model,

2) animal head model, 3) artificial models and 4) virtual/augmented reality simulators. Human cadaveric specimens constitute the current gold standard, as they provide a realistic environment, which, with specific modifications for managing ICA rupture, CSF leak, and tumor removal can enhance the training simulation. However, their availability is low due to excessive costs. Virtual Reality simulators and artificial models provided an excellent alternative. However, the lack of haptic realism and anatomical fidelity makes them ideal only for learning the basics. Augmented reality applied to cadaver-based models is an exciting solution that might be further developed in the near future. What emerged is that most of the artificial models do not provide a realistic and cost-efficient simulation of the most delicate and relatively common phase of surgery – i.e., tumor removal with arachnoid preservation.

From the results obtained by the review, an innovative training model was designed. The goal was to develop a system that could reproduce the fall of the arachnoid inside the sella turcica.

The development of the ETA sensor-based training model started from CT data of a patient's head, which was converted into an STL model. The model was a modular structure composed of different modules, each one representing a component of the "transsphenoidal route" (i.e., the anatomy encountered by the surgeons during the surgery), while the external parts were removed, in order to save materials and thus reduce costs. The model was designed using Meshmixer (Autodesk Inc.), a software for editing the mesh of 3D objects. From the skull base file, the sphenoid bone module (superior and inferior), the nasal septum module, the turbinates module (left and right), and the ethmoid bone module were obtained, with the addition of a frame, which is a non-anatomical part added to the training model as a basis for its assembly. From the face file, the nose module and the nostrils print core were obtained, which were used to guarantee the fabrication of the nostril's cavities. The modules were fabricated with the FFF technology, one of the most common additive manufacturing technologies. Each module was fabricated using an Ultimaker 3 Extended in PLA, except for the nasal septum, which was fabricated in TPU which, according to the literature, better mimics the mechanical properties of cartilage thanks to its lower flexural modulus. The nose and turbinates modules required another step for their fabrication. In fact, to better mimic the skin (nose module) and the mucosa (turbinates module), they were made by casting silicone into silicone molds. Using silicone molds allowed easier extraction of the components from the mold. The PLA printed modules of the nose, and the turbinates were used as a pattern to shape silicone molds, which was then casted in a silicone mold to reproduce the components. Finally, the model was validated by an experienced neurosurgeon who provided feedback. From a first endoscopic inspection, it appeared that the anatomy was well reproduced by the

model, however the sphenoid bone resulted slightly too thick. The flexural strength of both the TPU for the nasal septum and the silicone for the mucosa is close to the real one, but the elastic return of silicone was found to be too high. A problem that emerged from testing with surgical instruments is the thermal resistance of PLA. In fact, PLA powders produced during the drilling phase, dissolved and formed agglomerates that glued to the sphenoid bone module. Concerning the septum, even if it had a great flexural strength, its thickness was too high and, together with an elevated resilience of the material, it was difficult to cut during the simulation. Future studies will be focused on finding new materials to better mimic the bone consistency, as for example ceramics. Another aspect that will be improved is the anatomy reproduced in the model, by adding other obstacles that surgeons find during ETA approaches, such as the optic nerve and the internal carotid artery.

The first part of the thesis focused its attention on the development of a preliminary sensorized system able to mimic the arachnoid membrane and the CSF within it, when an external force is applied to them. In the literature, the arachnoid was reproduced with polymeric food film, based on former works and surgeons' experience. The first prototype showed low repeatability from one test to another, but an interesting inter-test repeatability which gave hope for future development. The arachnoid membrane was mimicked with polymeric film and the CSF was reproduced with distilled water. Preliminary tests demonstrated a strong linear correlation between pressure and force on the membrane (R^2 of 0.97 and sensitivity of 1.3 N/kPa). Then, the model was evaluated during a hands-on session that involved 11 experienced international surgeons who simulated a pituitary adenoma resection procedure, using pieces of boiled egg white to emulate the tumor. The preliminary threshold value is of interest, but this is a statistically limited result, since the size of the pool of surgeons who tested the model (n = 11). In order to validate the sensor-based model, the aim for the future is to produce several training models and to design specific training sessions. In this way it will be possible to better evaluate a critical threshold value with other experienced surgeons that can be used as a parameter to assess whether a less experienced surgeon/resident is able to perform simulated tumor mass removal without exceeding this threshold value. Then, training sessions will be conducted during specific neurosurgical summer schools and/or workshops to teach participants how to handle the arachnoid membrane before the operating room. During the session, force values and the surgeon's feedback were collected. Results on force were in line with the literature and allowed the identification of three working areas (Safe, Warning, and CSF Leak), which can be used to evaluate the trainee's performance. The innovative features of the model received valuable feedback from the surgeons. In particular, the arachnoid and the consistency of the pituitary

tumor were determined to be well mimicked. Future research will focus on improving the thickness and rigidity of the arachnoid and on how to achieve different consistencies for the pituitary adenoma. Also, bleeding will be reproduced, in order to offer a more vivid and realistic experience to surgeons who have little experience in ETA surgery. New sensors will be integrated into the training model to provide more data about the surgeon's performance to prepare them for entering the operating room with more confidence. Additionally, research will also focus on the reduction of the electronic setup's dimensions, with the objective of developing a portable version for testing purposes.

The last part of the thesis describes the development of an innovative surgical instrument, the probe, for in-vivo measurement of the hardness of the PA. The probe consists of three parts: a highly deformable tip, a TMR sensor with a magnet, and a rigid case. The working principle is based on how the deformation of the tip varies as it indents tissues of different hardness. In particular, the harder the tissue the larger the deformation. This particular use of a TMR sensor represented the main novelty of the project: the evaluation of the mechanical properties, in this case the hardness of soft tissues, by measuring the deformation of the tip, which is determined as the displacement undergone by the magnet during compression of the instrument. In this way it is possible to have an enclosed environment for the electronics, thus enabling sterilization processes. The tip has a flat end which is sustained by slender beams that flex during indentation. The magnet is mounted on the flat end and the TMR detects its displacement. In this way, it is possible to estimate the deformation of the tip and correlate it to the hardness of the tissue. The first prototype proposed is a novel and innovative sensorized probe capable of detecting the hardness of a soft material, by measuring the variation of the magnetic field generated by the displacement of a magnet glued to the tip with a magneto resistive sensor. After an initial calibration of the probe, indentation tests were performed with Shore A silicones. Results show a high repeatability of the tests with a mean variation for the three specimens < 1%: this indicates good repeatability of the probe under the same test conditions.

The second prototype, the “Working Probe”, is an improved version of the probe. An innovative design reduces the overall dimension of the probe so as to fit within the nasal cavities. In fact, the previous version had a diameter of 8.4 mm, while the new one has a diameter of 5.6 mm. Additionally, two different tips thickness, 0.75 mm and 0.45 mm, were evaluated. From indentation tests, the 0.45 mm tip revealed a lower scattering of the measures and the Shore 00 hardness for the egg white specimen was measured to be 16.1,

with a standard deviation of 2.02. Furthermore, the force obtained in indentation tests using the egg white sample to mimic the pituitary adenoma is consistent with the literature.

The improvement of the third prototype, the “Optimized Probe”, was focused on the characterization of the manufacturing process to control the dimensions of the beams, particularly their width. Initially, experimental tests were conducted to evaluate the repeatability and stability of the process as process parameters changed (layer height, nominal line width and print speed). Then, results were used to determine a regression model to predict and control the dimensions of the micro-beams. In particular, the results showed the feasibility ranges and how the print speed can only control the amount of extruded material in terms of deposited line width. Then, 18 probes having a different design in terms of beam width and number were fabricated. Widths from 0.42 mm to 0.63 mm (corresponding to print speed from 25 mm/s down to 5 mm/s) and 3 to 5 beams were considered. Then, the probes were used to indent specimens having a hardness from 51 ± 1 to 83 ± 1 Shore000 for a total of 6 samples: 4 made of casting silicone, 1 marshmallow and 1 boiled egg white sample. Indentation tests were conducted together with a Load Cell to additionally evaluate the force applied to each sample during the test. According to the results, the best probe designs in terms of robustness of the fabrication process in terms of accuracy, sensitivity and linearity of the measure were the ones with 4 and 5 beams fabricated with a print speed of 10 mm/s and a layer height of 0.05 mm. Moreover, these probes were able to estimate the hardness of the egg white and showed an error of > 1 % and 2 % respectively, validating the capability of the probe in testing adenoma tissue-like materials.

The results achieved are very promising and the probe will be further developed by testing real biological tissue to evaluate its performance and validate it in the surgical field. Moreover, some other aspects require further improvements. The first one is related to the range of tissue hardness that can be tested. In fact, the results showed a lower limit for the design here considered. Therefore, tips with a higher sensitivity should be tested to overcome this limit. Moreover, the current overall width of the probe is slightly larger than the requirements. Future work will be conducted with an ex-vivo specimen of a pituitary adenoma in order to characterize its hardness with the defined parameter $h_{\%}$, to find the best substitute and also to define a first classification of the hardness of different pituitary adenomas.

References

[1] F. Doglietto, D.M. Prevedello, J.A. Jane, J. Han, E.R. Laws, Brief history of endoscopic transsphenoidal surgery--from Philipp Bozzini to the First World Congress of Endoscopic Skull Base Surgery, Neurosurg. Focus 19 (2005) E3.

[2] E. Agosti, G. Saraceno, J. Qiu, B. Buffoli, M. Ferrari, E. Raffetti, F. Belotti, M. Ravanelli, D. Mattavelli, A. Schreiber, L. Hirtler, L.F. Rodella, R. Maroldi, P. Nicolai, F. Gentili, W. Kucharczyk, M.M. Fontanella, F. Doglietto, Quantitative anatomical comparison of transnasal and transcranial approaches to the clivus., Acta Neurochir. (Wien) 162 (2020) 649–660. https://doi.org/10.1007/s00701-019-04152-4.

[3] F. Doglietto, M. Ferrari, D. Mattavelli, F. Belotti, V. Rampinelli, H. Kheshaifati, D. Lancini, A. Schreiber, T. Sorrentino, M. Ravanelli, B. Buffoli, L. Hirtler, R. Maroldi, P. Nicolai, L.F. Rodella, M.M. Fontanella, Transnasal Endoscopic and Lateral Approaches to the Clivus: A Quantitative Anatomic Study., World Neurosurg. 113 (2018) e659–e671. https://doi.org/10.1016/j.wneu.2018.02.118.

[4] F. Belotti, F. Doglietto, A. Schreiber, M. Ravanelli, M. Ferrari, D. Lancini, V. Rampinelli, L. Hirtler, B. Buffoli, A. Bolzoni Villaret, R. Maroldi, L.F. Rodella, P. Nicolai, M.M. Fontanella, Modular Classification of Endoscopic Endonasal Transsphenoidal Approaches to Sellar Region: Anatomic Quantitative Study, World Neurosurg. 109 (2018) e281–e291. https://doi.org/10.1016/j.wneu.2017.09.165.

[5] A. Schreiber, M. Ferrari, V. Rampinelli, F. Doglietto, F. Belotti, D. Lancini, M. Ravanelli, L.F. Rodella, M.M. Fontanella, P. Nicolai, Modular endoscopic medial maxillectomies: quantitative analysis of surgical exposure in a preclinical setting, World Neurosurg. 100 (2017) 44–55.

[6] L. Sakka, G. Coll, J. Chazal, Anatomy and physiology of cerebrospinal fluid, Eur. Ann. Otorhinolaryngol. Head Neck Dis. 128 (2011) 309–316. https://doi.org/10.1016/j.anorl.2011.03.002.

[7] G. Santona, A. Madoglio, D. Mattavelli, M. Rigante, M. Ferrari, L. Lauretti, P. Mattogno, C. Parrilla, P. De Bonis, J. Galli, A. Olivi, M.M. Fontanella, A. Fiorentino, M. Serpelloni, F. Doglietto, Training models and simulators for endoscopic transsphenoidal surgery: a systematic review, Neurosurg. Rev. 46 (2023) 248. https://doi.org/10.1007/s10143-023-02149-3.

[8] J. Lin, Z. Zhou, J. Guan, Y. Zhu, Y. Liu, Z. Yang, B. Lin, Y. Jiang, X. Quan, Y. Ke, T. Xu, Using Three-Dimensional Printing to Create Individualized Cranial Nerve Models for Skull Base Tumor Surgery, World Neurosurg. 120 (2018) e142–e152. https://doi.org/10.1016/j.wneu.2018.07.236.

[9] N. Harada, K. Kondo, C. Miyazaki, J. Nomoto, S. Kitajima, M. Nemoto, H. Uekusa, M. Harada, N. Sugo, Modified three-dimensional brain model for study of the trans-sylvian approach, Neurol. Med. Chir. (Tokyo) 51 (2011) 567–571. https://doi.org/10.2176/nmc.51.567.

[10] K. Kenan, A. İhsan, O. Dilek, C. Burak, K. Gurkan, C. Savas, The learning curve in endoscopic pituitary surgery and our experience, Neurosurg. Rev. 29 (2006) 298–305. https://doi.org/10.1007/s10143-006-0033-9.

[11] N. Choudhury, N. Gélinas-Phaneuf, S. Delorme, R. Del Maestro, Fundamentals of Neurosurgery: Virtual Reality Tasks for Training and Evaluation of Technical Skills, World Neurosurg. 80 (2013) e9–e19. https://doi.org/10.1016/j.wneu.2012.08.022.

[12] T.-Y. Hsieh, B. Cervenka, R. Dedhia, E.B. Strong, T. Steele, Assessment of a patient-specific, 3-dimensionally printed endoscopic sinus and skull base surgical model, JAMA Otolaryngol. - Head Neck Surg. 144 (2018) 574–579. https://doi.org/10.1001/jamaoto.2018.0473.

[13] M.J. Page, J.E. McKenzie, P.M. Bossuyt, I. Boutron, T.C. Hoffmann, C.D. Mulrow, L. Shamseer, J.M. Tetzlaff, E.A. Akl, S.E. Brennan, R. Chou, J. Glanville, J.M. Grimshaw, A. Hróbjartsson, M.M. Lalu, T. Li, E.W. Loder, E. Mayo-Wilson, S. McDonald, L.A. McGuinness, L.A. Stewart, J. Thomas, A.C. Tricco, V.A. Welch, P. Whiting, D. Moher, The PRISMA 2020 statement: an updated guideline for reporting systematic reviews, BMJ 372 (2021) n71. https://doi.org/10.1136/bmj.n71.

[14] M.J. Page, D. Moher, P.M. Bossuyt, I. Boutron, T.C. Hoffmann, C.D. Mulrow, L. Shamseer, J.M. Tetzlaff, E.A. Akl, S.E. Brennan, R. Chou, J. Glanville, J.M. Grimshaw, A. Hróbjartsson, M.M. Lalu, T. Li, E.W. Loder, E. Mayo-Wilson, S. McDonald, L.A. McGuinness, L.A. Stewart, J. Thomas, A.C. Tricco, V.A. Welch, P. Whiting, J.E. McKenzie, PRISMA 2020 explanation and elaboration: updated guidance and exemplars for reporting systematic reviews, BMJ 372 (2021) n160. https://doi.org/10.1136/bmj.n160.

[15] S. Chan, F. Conti, K. Salisbury, N.H. Blevins, Virtual reality simulation in neurosurgery: Technologies and evolution, Neurosurgery 72 (2013) A154–A164. https://doi.org/10.1227/NEU.0b013e3182750d26.

[16] A.R. Cohen, S. Lohani, S. Manjila, S. Natsupakpong, N. Brown, M.C. Cavusoglu, Virtual reality simulation: Basic concepts and use in endoscopic neurosurgery training, Childs Nerv. Syst. 29 (2013) 1235–1244. https://doi.org/10.1007/s00381-013-2139-z.

[17] A. Neubauer, S. Wolfsberger, Virtual endoscopy in neurosurgery: A review, Neurosurgery 72 (2013) A97–A106. https://doi.org/10.1227/NEU.0b013e31827393c9.

[18] M. Randazzo, J.M. Pisapia, N. Singh, J.P. Thawani, 3D printing in neurosurgery: A systematic review, Surg. Neurol. Int. 7 (2016) S801–S809. https://doi.org/10.4103/2152-7806.194059.

[19] V.N. Vakharia, N.N. Vakharia, C.S. Hill, Review of 3-Dimensional Printing on Cranial Neurosurgery Simulation Training, World Neurosurg. 88 (2016) 188–198. https://doi.org/10.1016/j.wneu.2015.12.031.

[20] T. Kin, H. Nakatomi, N. Shono, S. Nomura, T. Saito, H. Oyama, N. Saito, Neurosurgical virtual reality simulation for brain tumor using high-definition computer graphics: A review of the literature, Neurol. Med. Chir. (Tokyo) 57 (2017) 513–520. https://doi.org/10.2176/nmc.ra.2016-0320.

[21] B. Langridge, S. Momin, B. Coumbe, E. Woin, M. Griffin, P. Butler, Systematic Review of the Use of 3-Dimensional Printing in Surgical Teaching and Assessment, J. Surg. Educ. 75 (2018) 209–221. https://doi.org/10.1016/j.jsurg.2017.06.033.

[22] A. Shinomiya, A. Shindo, M. Kawanishi, K. Miyake, T. Nakamura, S. Matsubara, T. Tamiya, Usefulness of the 3D virtual visualization surgical planning simulation and 3D model for endoscopic endonasal transsphenoidal surgery of pituitary adenoma: Technical report and review of literature, Interdiscip. Neurosurg. Adv. Tech. Case Manag. 13 (2018) 13–19. https://doi.org/10.1016/j.inat.2018.02.002.

[23] D.H. Kim, Y. Kim, J.-S. Park, S.W. Kim, Virtual reality simulators for endoscopic sinus and skull base surgery: The present and future, Clin. Exp. Otorhinolaryngol. 12 (2019) 12–17. https://doi.org/10.21053/ceo.2018.00906.

[24] S.B. Tomlinson, B.K. Hendricks, A. Cohen-Gadol, Immersive Three-Dimensional Modeling and Virtual Reality for Enhanced Visualization of Operative Neurosurgical Anatomy, World Neurosurg. 131 (2019) 313–320. https://doi.org/10.1016/j.wneu.2019.06.081.

[25] C.M. Low, J.M. Morris, D.L. Price, J.S. Matsumoto, J.K. Stokken, E.K. O'Brien, G. Choby, Three-Dimensional Printing: Current Use in Rhinology and Endoscopic Skull Base Surgery, Am. J. Rhinol. Allergy 33 (2019) 770–781. https://doi.org/10.1177/1945892419866319.

[26] B. Baby, R. Singh, R. Singh, A. Suri, C. Arora, S. Kumar, P.K. Kalra, S. Banerjee, A Review of Physical Simulators for Neuroendoscopy Skills Training, World Neurosurg. 137 (2020) 398–407. https://doi.org/10.1016/j.wneu.2020.01.183.

[27] B. Baby, R. Singh, A. Suri, R.R. Dhanakshirur, A. Chakraborty, S. Kumar, P.K. Kalra, S. Banerjee, A review of virtual reality simulators for neuroendoscopy, Neurosurg. Rev. 43 (2020) 1255–1272. https://doi.org/10.1007/s10143-019-01164-7.
[28] J. Bajaj, P.S. Chandra, Recent Developments in Endoscopic Endonasal Approach for Pituitary Adenomas, Neurol. India 68 (2020) S79–S84. https://doi.org/10.4103/0028-3886.287671.
[29] P. Lavigne, N. Yang, Training and Surgical Simulation in Skull Base Surgery: a Systematic Review, Curr. Otorhinolaryngol. Rep. 8 (2020) 154–159. https://doi.org/10.1007/s40136-020-00280-z.
[30] E.A. Patel, A. Aydin, M. Cearns, P. Dasgupta, K. Ahmed, A Systematic Review of Simulation-Based Training in Neurosurgery, Part 1: Cranial Neurosurgery, World Neurosurg. 133 (2020) e850–e873. https://doi.org/10.1016/j.wneu.2019.08.262.
[31] L.R. Maclachlan, H. Alexander, D. Forrestal, J.I. Novak, M. Redmond, Properties and Characteristics of Three-Dimensional Printed Head Models Used in Simulation of Neurosurgical Procedures: A Scoping Review, World Neurosurg. 156 (2021) 133-146.e6. https://doi.org/10.1016/j.wneu.2021.09.079.
[32] G.M. Thiong'o, M. Bernstein, J.M. Drake, 3D printing in neurosurgery education: a review, 3D Print. Med. 7 (2021) 9. https://doi.org/10.1186/s41205-021-00099-4.
[33] H. Li, L. Lu, N. Li, L. Zi, Q. Wen, Application of Three-Dimensional (3D) Printing in Neurosurgery, Adv. Mater. Sci. Eng. 2022 (2022). https://doi.org/10.1155/2022/8015625.
[34] J. James, A.L. Irace, D.A. Gudis, J.B. Overdevest, Simulation training in endoscopic skull base surgery: A scoping review, World J. Otorhinolaryngol. - Head Neck Surg. 8 (2022) 73–81. https://doi.org/10.1002/wjo2.11.
[35] J.E. Blohm, P.A. Salinas, M.J. Avila, S.R. Barber, M.E. Weinand, T.M. Dumont, Three-Dimensional Printing in Neurosurgery Residency Training: A Systematic Review of the Literature, World Neurosurg. 161 (2022) 111–122. https://doi.org/10.1016/j.wneu.2021.10.069.
[36] S.G. Thavarajasingam, R. Vardanyan, A. Arjomandi Rad, A. Thavarajasingam, A. Khachikyan, N. Mendoza, R. Nair, P. Vajkoczy, The use of augmented reality in transsphenoidal surgery: A systematic review, Br. J. Neurosurg. 36 (2022) 457–471. https://doi.org/10.1080/02688697.2022.2057435.
[37] M. Berhouma, N.B. Baidya, A.A. Ismaïl, J. Zhang, M. Ammirati, Shortening the learning curve in endoscopic endonasal skull base surgery: A reproducible polymer tumor model for the trans-sphenoidal trans-tubercular approach to retro-infundibular tumors, Clin. Neurol. Neurosurg. 115 (2013) 1635–1641. https://doi.org/10.1016/j.clineuro.2013.02.013.
[38] F. Gagliardi, A.M. Chau, P. Mortini, A.J. Caputy, C. Gragnaniello, Skull Base Neuroendoscopic Training Model Using a Fibrous Injectable Tumor Polymer and the Nico Myriad, J. Craniofac. Surg. 29 (2018) e25–e28. https://doi.org/10.1097/SCS.0000000000004042.
[39] C. Gragnaniello, R. Nader, T. van Doormaal, M. Kamel, E.H.J. Voormolen, G. Lasio, E. Aboud, L. Regli, C.A.F. Tulleken, O. Al-Mefty, Skull base tumor model, J. Neurosurg. 113 (2010) 1106–1111. https://doi.org/10.3171/2010.3.JNS09513.
[40] C. Li, H. Zhu, J. Zheng, C. Liu, S. Gui, P. Zhao, J. Bai, Y. Zhang, Development and Application of Three Steps Training Mode for Endoscopic Transnasal Transsphenoidal Approach, J. Craniofac. Surg. 33 (2022) 1554–1558. https://doi.org/10.1097/SCS.0000000000008257.
[41] D.A. Donoho, C.E. Johnson, K.T. Hur, I.A. Buchanan, V.L. Fredrickson, M. Minneti, G. Zada, B.B. Wrobel, Costs and training results of an objectively validated cadaveric perfusion-based internal carotid artery injury simulation during endoscopic skull base surgery, Int. Forum Allergy Rhinol. 9 (2019) 787–794. https://doi.org/10.1002/alr.22319.

[42] M. Pham, A. Kale, Y. Marquez, J. Winer, B. Lee, B. Harris, M. Minnetti, J. Carey, S. Giannotta, G. Zada, A Perfusion-based Human Cadaveric Model for Management of Carotid Artery Injury during Endoscopic Endonasal Skull Base Surgery, J. Neurol. Surg. Part B Skull Base 75 (2014) 309–313. https://doi.org/10.1055/s-0034-1372470.

[43] J.N. Ciporen, B. Lucke-Wold, G. Mendez, W.E. Cameron, S. McCartney, Endoscopic Management of Cavernous Carotid Surgical Complications: Evaluation of a Simulated Perfusion Model, World Neurosurg. 98 (2017) 388–396. https://doi.org/10.1016/j.wneu.2016.11.018.

[44] P. Pacca, S.S. Jhawar, D.V. Seclen, E. Wang, C. Snyderman, P.A. Gardner, E. Aboud, J.C. Fernandez-Miranda, "Live Cadaver" Model for Internal Carotid Artery Injury Simulation in Endoscopic Endonasal Skull Base Surgery, Oper. Neurosurg. Hagerstown Md 13 (2017) 732–738. https://doi.org/10.1093/ons/opx035.

[45] J. Shen, K. Hur, Z. Zhang, M. Minneti, M. Pham, B. Wrobel, G. Zada, Objective Validation of Perfusion-Based Human Cadaveric Simulation Training Model for Management of Internal Carotid Artery Injury in Endoscopic Endonasal Sinus and Skull Base Surgery, Oper. Neurosurg. Hagerstown Md 15 (2018) 231–238. https://doi.org/10.1093/ons/opx262.

[46] D.A. Donoho, D.J. Pangal, G. Kugener, M. Rutkowski, A. Micko, S. Shahrestani, A. Brunswick, M. Minneti, B.B. Wrobel, G. Zada, Improved surgeon performance following cadaveric simulation of internal carotid artery injury during endoscopic endonasal surgery: training outcomes of a nationwide prospective educational intervention, J. Neurosurg. (2021) 1–9. https://doi.org/10.3171/2020.9.JNS202672.

[47] A. AlQahtani, N.R. London, P. Castelnuovo, D. Locatelli, A. Stamm, A.A. Cohen-Gadol, H. Elbosraty, R. Casiano, J. Morcos, E. Pasquini, G. Frank, D. Mazzatenta, G. Barkhoudarian, C. Griffiths, D. Kelly, C. Georgalas, N. Janakiram, P. Nicolai, D.M. Prevedello, R.L. Carrau, Assessment of Factors Associated With Internal Carotid Injury in Expanded Endoscopic Endonasal Skull Base Surgery, JAMA Otolaryngol.-- Head Neck Surg. 146 (2020) 364–372. https://doi.org/10.1001/jamaoto.2019.4864.

[48] E.A. Christian, J. Bakhsheshian, B.A. Strickland, V.L. Fredrickson, I.A. Buchanan, M.H. Pham, A. Cervantes, M. Minneti, B.B. Wrobel, S. Giannotta, G. Zada, Perfusion-based human cadaveric specimen as a simulation training model in repairing cerebrospinal fluid leaks during endoscopic endonasal skull base surgery, J. Neurosurg. 129 (2018) 792–796. https://doi.org/10.3171/2017.5.JNS162982.

[49] D. Mattavelli, M. Ferrari, V. Rampinelli, A. Schreiber, B. Buffoli, A. Deganello, L.F. Rodella, M.M. Fontanella, P. Nicolai, F. Doglietto, Development and validation of a preclinical model for training and assessment of cerebrospinal fluid leak repair in endoscopic skull base surgery, Int. Forum Allergy Rhinol. 10 (2020) 89–96. https://doi.org/10.1002/alr.22451.

[50] A.A. AlQahtani, A.A. Albathi, O.M. Alhammad, A.S. Alrabie, Innovative real CSF leak simulation model for rhinology training: human cadaveric design, Eur. Arch. Oto-Rhino-Laryngol. Off. J. Eur. Fed. Oto-Rhino-Laryngol. Soc. EUFOS Affil. Ger. Soc. Oto-Rhino-Laryngol. - Head Neck Surg. 275 (2018) 937–941. https://doi.org/10.1007/s00405-018-4902-y.

[51] A. AlQahtani, A. Albathi, P. Castelnuovo, F. Alfawwaz, Cerebrospinal Fluid Leak Repair Simulation Model: Face, Content, and Construct Validation, Am. J. Rhinol. Allergy 35 (2021) 264–271. https://doi.org/10.1177/1945892420952262.

[52] J. Ciporen, B. Lucke-Wold, A. Dogan, J.S. Cetas, W.E. Cameron, Dual Endoscopic Endonasal Transsphenoidal and Precaruncular Transorbital Approaches for Clipping of the Cavernous Carotid Artery: A Cadaveric Simulation, J. Neurol. Surg. Part B Skull Base 77 (2016) 485–490. https://doi.org/10.1055/s-0036-1584094.

[53] R. Mladina, N. Skitarelić, C. Cingi, L. Chen, N.B. Muluk, The Validity of Training Endoscopic Sinus and Skull Base Surgery Techniques on the Experimental Head Model,

J. Craniofac. Surg. 29 (2018) 498–501. https://doi.org/10.1097/SCS.0000000000004208.
[54] J.C. Fernandez-Miranda, J. Barges-Coll, D.M. Prevedello, J. Engh, C. Snyderman, R. Carrau, P.A. Gardner, A.B. Kassam, Animal model for endoscopic neurosurgical training: technical note, Minim. Invasive Neurosurg. MIN 53 (2010) 286–289. https://doi.org/10.1055/s-0030-1269927.
[55] Z. Awad, P. Touska, A. Arora, P. Ziprin, A. Darzi, N.S. Tolley, Face and content validity of sheep heads in endoscopic rhinology training, Int. Forum Allergy Rhinol. 4 (2014) 851–858. https://doi.org/10.1002/alr.21362.
[56] G. Isaacson, D.C. Ianacone, M.R. Wolfson, Ex vivo ovine model for pediatric flexible endoscopy training, Int. J. Pediatr. Otorhinolaryngol. 79 (2015) 2196–2199. https://doi.org/10.1016/j.ijporl.2015.10.002.
[57] R. Valentine, V. Padhye, P.-J. Wormald, Simulation Training for Vascular Emergencies in Endoscopic Sinus and Skull Base Surgery, Otolaryngol. Clin. North Am. 49 (2016) 877–887. https://doi.org/10.1016/j.otc.2016.02.013.
[58] R. Valentine, V. Padhye, P.-J. Wormald, Management of arterial injury during endoscopic sinus and skull base surgery, Curr. Opin. Otolaryngol. Head Neck Surg. 24 (2016) 170–174. https://doi.org/10.1097/MOO.0000000000000239.
[59] R. Valentine, P.-J. Wormald, A Vascular Catastrophe during Endonasal Surgery: An Endoscopic Sheep Model, Skull Base 21 (2011) 109–114. https://doi.org/10.1055/s-0031-1275255.
[60] L.B. Mallmann, O.B. Piltcher, G.R. Isolan, The Lamb's Head as a Model for Surgical Skills Development in Endonasal Surgery, J. Neurol. Surg. Part B Skull Base 77 (2016) 466–472. https://doi.org/10.1055/s-0036-1583186.
[61] R. Mladina, P. Castelnuovo, D. Locatelli, K.Đ. Vuković, N. Skitarelić, Training Cerebrospinal Fluid Leak Repair with Nasoseptal Flap on the Lamb's Head, ORL 75 (2013) 32–36. https://doi.org/10.1159/000347080.
[62] N. Skitarelić, R. Mladina, Lamb's head: The model for novice education in endoscopic sinus surgery, World J. Methodol. 5 (2015) 144–148. https://doi.org/10.5662/wjm.v5.i3.144.
[63] M.A. Masalha, K.K. VanKoevering, O.S. Latif, A.R. Powell, A. Zhang, K.H. Hod, D.M. Prevedello, R.L. Carrau, Simulation of Cerebrospinal Fluid Leak Repair Using a 3-Dimensional Printed Model, Am. J. Rhinol. Allergy (2021) 19458924211003537. https://doi.org/10.1177/19458924211003537.
[64] I. Jusue-Torres, S. Sivakanthan, C.D. Pinheiro-Neto, P.A. Gardner, C.H. Snyderman, J.C. Fernandez-Miranda, Chicken wing training model for endoscopic microsurgery, J. Neurol. Surg. Part B Skull Base 74 (2013) 286–291. https://doi.org/10.1055/s-0033-1348026.
[65] P. Sanromán-Álvarez, J.A. Simal-Julián, A. García-Piñero, P. Miranda-Lloret, Multitask Box Trainer for Endoscopic Endonasal Skull Base Surgery: ENDOtrainer, World Neurosurg. 101 (2017) 304–307. https://doi.org/10.1016/j.wneu.2017.02.008.
[66] A. Altun, C. Cokluk, Endoscopic training model for intranasal transsphenoidal hypophysis surgery using a skull model and chicken wings, Turk. Neurosurg. 30 (2020) 377–381. https://doi.org/10.5137/1019-5149.JTN.25841-19.4.
[67] S. Tikka, B.G. Chaithra, S.B. Sharma, T.N. Janakiram, A Feasible, Low-Cost, Capsicum and Tomato Model for Endoscopic Sinus and Skull Base Surgery Training, Indian J. Otolaryngol. Head Neck Surg. (2021). https://doi.org/10.1007/s12070-021-02583-z.
[68] R. Hirayama, Y. Fujimoto, M. Umegaki, N. Kagawa, M. Kinoshita, N. Hashimoto, T. Yoshimine, Training to acquire psychomotor skills for endoscopic endonasal surgery using a personal webcam trainer: Clinical article, J. Neurosurg. 118 (2013) 1120–1126. https://doi.org/10.3171/2012.12.JNS12908.

[69] R. Singh, B. Baby, N. Damodaran, V. Srivastav, A. Suri, S. Banerjee, S. Kumar, P. Kalra, S. Prasad, K. Paul, S. Anand, S. Kumar, V. Dhiman, D. Ben-Israel, K.S. Kapoor, Design and Validation of an Open-Source, Partial Task Trainer for Endonasal Neuro-Endoscopic Skills Development: Indian Experience, World Neurosurg. 86 (2016) 259–269. https://doi.org/10.1016/j.wneu.2015.09.045.

[70] S.S. Berkowitz, Teaching transnasal endoscopy to graduate students without a hospital or simulation laboratory: Pool noodles and cadavers, Am. J. Speech Lang. Pathol. 26 (2017) 709–715. https://doi.org/10.1044/2017_AJSLP-15-0119.

[71] V.K. Srivastav, B. Baby, R. Singh, P. Kalra, A. Suri, Neuro-endo-trainer-online assessment system (NET-OAS) for neuro-endoscopic skills training, in: 2017: pp. 213–219. https://doi.org/10.15439/2017F316.

[72] T. Xie, X. Zhang, Y. Gu, C. Sun, T. Liu, A low cost and stepwise training model for skull base repair using a suturing and knotting technique during endoscopic endonasal surgery, Eur. Arch. Otorhinolaryngol. 275 (2018) 2187–2192. https://doi.org/10.1007/s00405-018-5024-2.

[73] R.R. Bright, L. Varghese, R. Kurien, Construct and Validation of a Three-Dimensional Physical Model for Training in Transnasal Office Procedures, Indian J. Otolaryngol. Head Neck Surg. (2021). https://doi.org/10.1007/s12070-021-02775-7.

[74] S. Tikka, B.G. Chaithra, S.B. Sharma, T.N. Janakiram, A Feasible, Low-Cost, Capsicum and Tomato Model for Endoscopic Sinus and Skull Base Surgery Training, Indian J. Otolaryngol. Head Neck Surg. 74 (2022) 4565–4570. https://doi.org/10.1007/s12070-021-02583-z.

[75] P. Gallet, J. Rebois, D.-T. Nguyen, R. Jankowski, M. Perez, C. Rumeau, Simulation-based training in endoscopic endonasal surgery: Assessment of the cyrano simulator, Eur. Ann. Otorhinolaryngol. Head Neck Dis. 138 (2021) 29–34. https://doi.org/10.1016/j.anorl.2020.08.012.

[76] H.R. Briner, D. Simmen, N. Jones, D. Manestar, M. Manestar, A. Lang, P. Groscurth, Evaluation of an anatomic model of the paranasal sinuses for endonasal surgical training, Rhinology 45 (2007) 20–23.

[77] T. Okuda, K. Kataoka, A. Kato, Training in endoscopic endonasal transsphenoidal surgery using a skull model and eggs, Acta Neurochir. (Wien) 152 (2010) 1801–1804. https://doi.org/10.1007/s00701-010-0728-0.

[78] K.J. Shah, J.C. Peterson, D.D. Beahm, P.J. Camarata, R.B. Chamoun, Three-Dimensional Printed Model Used to Teach Skull Base Anatomy Through a Transsphenoidal Approach for Neurosurgery Residents, Oper. Neurosurg. Hagerstown Md 12 (2016) 326–329. https://doi.org/10.1227/NEU.0000000000001127.

[79] G. Chen, F. Ling, A new plastic model of endoscopic technique training for endonasal transsphenoidal pituitary surgery, Chin. Med. J. (Engl.) 123 (2010) 2576–2579. https://doi.org/10.3760/cma.j.issn.0366-6999.2010.18.016.

[80] C.-Y. Ding, X.-H. Yi, C.-Z. Jiang, H. Xu, X.-R. Yan, Y.-L. Zhang, D.-Z. Kang, Z.-Y. Lin, Development and validation of a multi-color model using 3-dimensional printing technology for endoscopic endonasal surgical training, Am. J. Transl. Res. 11 (2019) 1040–1048.

[81] D.C. Engel, A. Ferrari, A.-J. Tasman, R. Schmid, R. Schindel, S.R. Haile, L. Mariani, J.-Y. Fournier, A basic model for training of microscopic and endoscopic transsphenoidal pituitary surgery: the Egghead, Acta Neurochir. (Wien) 157 (2015) 1771–1777. https://doi.org/10.1007/s00701-015-2544-z.

[82] L.N. Kashapov, N.F. Kashapov, R.N. Kashapov, B.Y. Pashaev, The application of additive technologies in creation a medical simulator-trainer of the human head operating field, IOP Conf. Ser. Mater. Sci. Eng. 134 (2016) 012011. https://doi.org/10.1088/1757-899X/134/1/012011.

[83] N.R. London, G.G. Rangel, K. VanKoevering, A. Zhang, A.R. Powell, D.M. Prevedello, R.L. Carrau, P.C. Walz, Simulation of Pediatric Anterior Skull Base Anatomy Using a 3D Printed Model, World Neurosurg. 147 (2021) e405–e410. https://doi.org/10.1016/j.wneu.2020.12.077.
[84] T. Masuda, H. Kanako, S. Adachi, F. Arai, S. Omata, A. Morita, T. Kin, N. Saito, J. Yamashita, K. Chinzei, A. Haswgawa, T. Fukuda, Patients Simulator for Transsphenoidal Surgery, in: 2018. https://doi.org/10.1109/MHS.2018.8886922.
[85] G. Maza, K.K. VanKoevering, J.C. Yanez-Siller, T. Baglam, B.A. Otto, D.M. Prevedello, R.L. Carrau, Surgical simulation of a catastrophic internal carotid artery injury: a laser-sintered model, Int. Forum Allergy Rhinol. 9 (2019) 53–59. https://doi.org/10.1002/alr.22178.
[86] J. Muto, R.L. Carrau, K. Oyama, B.A. Otto, D.M. Prevedello, Training model for control of an internal carotid artery injury during transsphenoidal surgery, Laryngoscope 127 (2017) 38–43. https://doi.org/10.1002/lary.26181.
[87] V. Narayanan, P. Narayanan, R. Rajagopalan, R. Karuppiah, Z.A.A. Rahman, P.-J. Wormald, C.A. Van Hasselt, V. Waran, Endoscopic skull base training using 3D printed models with pre-existing pathology, Eur. Arch. Otorhinolaryngol. 272 (2015) 753–757. https://doi.org/10.1007/s00405-014-3300-3.
[88] T. Okuda, J. Yamashita, M. Fujita, H. Yoshioka, T. Tasaki, A. Kato, The chicken egg and skull model of endoscopic endonasal transsphenoidal surgery improves trainee drilling skills, Acta Neurochir. (Wien) 156 (2014) 1403–1407. https://doi.org/10.1007/s00701-014-2035-7.
[89] Z. Shen, Y. Xie, X. Shang, G. Xiong, S. Chen, Y. Yao, Z. Pan, H. Pan, X. Dong, Y. Li, C. Guo, F.-Y. Wang, The manufacturing procedure of 3D printed models for endoscopic endonasal transsphenoidal pituitary surgery, Technol. Health Care Off. J. Eur. Soc. Eng. Med. 28 (2020) 131–150. https://doi.org/10.3233/THC-209014.
[90] B.L. Tai, A.C. Wang, J.R. Joseph, P.I. Wang, S.E. Sullivan, E.L. McKean, A.J. Shih, D.M. Rooney, A physical simulator for endoscopic endonasal drilling techniques: Technical note, J. Neurosurg. 124 (2016) 811–816. https://doi.org/10.3171/2015.3.JNS1552.
[91] V. Waran, D. Pancharatnam, H.C. Thambinayagam, R. Raman, A.K. Rathinam, Y.K. Balakrishnan, T.S. Tung, Z.A. Rahman, The utilization of cranial models created using rapid prototyping techniques in the development of models for navigation training, J. Neurol. Surg. Part Cent. Eur. Neurosurg. 75 (2014) 12–15. https://doi.org/10.1055/s-0032-1330960.
[92] G. Wen, Z. Cong, K. Liu, C. Tang, C. Zhong, L. Li, X. Dai, C. Ma, A practical 3D printed simulator for endoscopic endonasal transsphenoidal surgery to improve basic operational skills, Childs Nerv. Syst. ChNS Off. J. Int. Soc. Pediatr. Neurosurg. 32 (2016) 1109–1116. https://doi.org/10.1007/s00381-016-3051-0.
[93] J.-P. Zheng, C.-Z. Li, G.-Q. Chen, Multimaterial and multicolor 3D-printed model in training of transnasal endoscopic surgery for pituitary adenoma, Neurosurg. Focus 47 (2019) E21. https://doi.org/10.3171/2019.6.FOCUS19294.
[94] J.-P. Zheng, C.-Z. Li, G.-Q. Chen, G.-D. Song, Y.-Z. Zhang, Three-Dimensional Printed Skull Base Simulation for Transnasal Endoscopic Surgical Training, World Neurosurg. 111 (2018) e773–e782. https://doi.org/10.1016/j.wneu.2017.12.169.
[95] ProDelphus, (n.d.). http://www.prodelphus.com.br/websiteBR/website/home/ (accessed December 23, 2022).
[96] 3D Printed Skull Base for Head Holder Model | A22 | KEZLEX, (n.d.). https://www.kezlex.com/en/products/skull/a22 (accessed December 3, 2022).
[97] 3D Printed Endoscopic for Pituitary Gland Model | A39 | KEZLEX, (n.d.). https://www.kezlex.com/en/products/skull/a39/ (accessed November 17, 2021).
[98] 3D Printed Internal Carotid Artery Injury ICAI Model Model | A43 | KEZLEX, (n.d.). https://www.kezlex.com/en/products/skull/a43/ (accessed December 3, 2022).

[99] Japan Medical Company, Jpn. Med. Co. (n.d.). https://japanmedicalcompany.co.jp/en (accessed March 16, 2023).
[100] SIMONT ENT AND SKULL BASE SIMULATOR - Youtube, 2008. https://www.youtube.com/watch?v=iUqcVprRXuk (accessed December 23, 2022).
[101] J. Shen, B.B. Wrobel, G. Zada, Management of Vascular Injuries During Endoscopic Skull Base Surgery: Current Strategies and Simulation-Based Educational Paradigms, Curr. Otorhinolaryngol. Rep. 5 (2017) 35–41. https://doi.org/10.1007/s40136-017-0146-4.
[102] J.F. Nogueira, A.C. Stamm, M. Lyra, F.O. Balieiro, F.S. Leão, Building a real endoscopic sinus and skull-base surgery simulator, Otolaryngol. Head Neck Surg. 139 (2008) 727–728. https://doi.org/10.1016/j.otohns.2008.07.017.
[103] S. Zymberg, F. Vaz-Guimarães Filho, M. Lyra, Neuroendoscopic training: presentation of a new real simulator, Minim. Invasive Neurosurg. MIN 53 (2010) 44–46. https://doi.org/10.1055/s-0029-1246169.
[104] Neuroendoscopic Surgery Training Simulator – GTSimulators.com, (n.d.). https://www.gtsimulators.com/products/neuroendoscopic-surgery-training-simulator-snt (accessed December 3, 2022).
[105] 3D Printed Medical Anatomy Models from JAPAN | KEZLEX, (n.d.). https://www.kezlex.com/en/ (accessed December 5, 2022).
[106] G. Chen, F. Ling, A new plastic model of endoscopic technique training for endonasal transsphenoidal pituitary surgery, Chin. Med. J. (Engl.) 123 (2010) 2576–2579.
[107] H.H.L. Chan, J.H. Siewerdsen, A. Vescan, M.J. Daly, E. Prisman, J.C. Irish, 3D rapid prototyping for otolaryngology-head and neck surgery: Applications in image-guidance, surgical simulation and patient-specific modeling, PLoS ONE 10 (2015). https://doi.org/10.1371/journal.pone.0136370.
[108] M. Lai, S. Skyrman, F. Kor, R. Homan, D. Babic, E. Edström, O. Persson, G. Burström, A. Elmi-Terander, B.H.W. Hendriks, P.H.N. De With, Development of a CT-compatible anthropomorphic skull phantom for surgical planning, training, and simulation, in: 2021. https://doi.org/10.1117/12.2577629.
[109] K. Oyama, L.F.S.D. Filho, J. Muto, D.G. de Souza, R. Gun, B.A. Otto, R.L. Carrau, D.M. Prevedello, Endoscopic endonasal cranial base surgery simulation using an artificial cranial base model created by selective laser sintering, Neurosurg. Rev. 38 (2015) 171–178. https://doi.org/10.1007/s10143-014-0580-4.
[110] J. Muto, R.L. Carrau, K. Oyama, B.A. Otto, D.M. Prevedello, Training model for control of an internal carotid artery injury during transsphenoidal surgery, The Laryngoscope 127 (2017) 38–43. https://doi.org/10.1002/lary.26181.
[111] S. Wolfsberger, M.-T. Forster, M. Donat, A. Neubauer, K. Bühler, R. Wegenkittl, T. Czech, J.A. Hainfellner, E. Knosp, Virtual endoscopy is a useful device for training and preoperative planning of transsphenoidal endoscopic pituitary surgery, Minim. Invasive Neurosurg. MIN 47 (2004) 214–220. https://doi.org/10.1055/s-2004-818523.
[112] A. Neubauer, S. Wolfsberger, M.-T. Forster, L. Mroz, R. Wegenkittl, K. Bühler, Advanced virtual endoscopic pituitary surgery, IEEE Trans. Vis. Comput. Graph. 11 (2005) 497–506. https://doi.org/10.1109/TVCG.2005.70.
[113] S. Wolfsberger, A. Neubauer, K. Bühler, R. Wegenkittl, T. Czech, S. Gentzsch, H.-G. Böcher-Schwarz, E. Knosp, Advanced virtual endoscopy for endoscopic transsphenoidal pituitary surgery, Neurosurgery 59 (2006) 1001–1009. https://doi.org/10.1227/01.NEU.0000245594.61828.41.
[114] A. Pößneck, E. Nowatius, C. Trantakis, H. Cakmak, H. Maass, U. Kühnapfel, A. Dietz, G. Strauß, A virtual training system in endoscopic sinus surgery, Int. Congr. Ser. 1281 (2005) 527–530. https://doi.org/10.1016/j.ics.2005.03.184.

[115] D.B. Clarke, R.C.N. D'Arcy, S. Delorme, D. Laroche, G. Godin, S.G. Hajra, R. Brooks, R. Diraddo, Virtual reality simulator: Demonstrated use in neurosurgical oncology, Surg. Innov. 20 (2013) 190–197. https://doi.org/10.1177/1553350612451354.
[116] R. Varshney, S. Frenkiel, L.H.P. Nguyen, M. Young, R. Del Maestro, A. Zeitouni, M.A. Tewfik, J. Hovdebo, N. Choudhury, P. Debergue, G. DeLuca, D. Jiang, V. Pazos, O. Comas, A. Neubauer, A. Cabral, D. Laroche, F. Thibault, R. DiRaddo, Development of the McGill simulator for endoscopic sinus surgery: A new high-fidelity virtual reality simulator for endoscopic sinus surgery, Am. J. Rhinol. Allergy 28 (2014) 330–334. https://doi.org/10.2500/ajra.2014.28.4046.
[117] T.-B. Won, P. Hwang, J.H. Lim, S.-W. Cho, S.H. Paek, S. Losorelli, Y. Vaisbuch, S. Chan, K. Salisbury, N.H. Blevins, Early experience with a patient-specific virtual surgical simulation for rehearsal of endoscopic skull-base surgery, Int. Forum Allergy Rhinol. 8 (2018) 54–63. https://doi.org/10.1002/alr.22037.
[118] S.A. Heredia-Pérez, K. Harada, M.A. Padilla-Castañeda, M. Marques-Marinho, J.A. Márquez-Flores, M. Mitsuishi, Virtual reality simulation of robotic transsphenoidal brain tumor resection: Evaluating dynamic motion scaling in a master-slave system, Int. J. Med. Robot. 15 (2019). https://doi.org/10.1002/rcs.1953.
[119] M. De Notaris, T. Topczewski, M. De Angelis, J. Enseñat, I. Alobid, A.M. Gondolbleu, G. Soria, J.B. Gonzalez, E. Ferrer, A. Prats-Galino, Anatomic skull base education using advanced neuroimaging techniques, World Neurosurg. 79 (2013) S16.e9-S16.e13. https://doi.org/10.1016/j.wneu.2012.02.027.
[120] NeuroVR – NeuroSim, (n.d.). https://neurosim.mcgill.ca/neurotouch (accessed December 5, 2022).
[121] NeuroTouch: Transnasal Navigation, 2011. https://www.youtube.com/watch?v=89A50YRy3gc (accessed March 16, 2023).
[122] G. Rosseau, J. Bailes, R. Del Maestro, A. Cabral, N. Choudhury, O. Comas, P. Debergue, G. De Luca, J. Hovdebo, D. Jiang, D. Laroche, A. Neubauer, V. Pazos, F. Thibault, R. Diraddo, The Development of a virtual simulator for training neurosurgeons to perform and perfect endoscopic endonasal transsphenoidal surgery, Neurosurgery 73 (2013) S85–S93. https://doi.org/10.1227/NEU.0000000000000112.
[123] Simulation Based Medical Education Solutions | CAE Healthcare, (n.d.). https://www.caehealthcare.com/ (accessed May 8, 2023).
[124] VOXEL-MAN Sinus, (n.d.). https://www.voxel-man.com/simulators/sinus/ (accessed December 23, 2022).
[125] UKE - UKE - Knowledge - Research - Healing, (n.d.). https://www.uke.de/english/ (accessed December 23, 2022).
[126] Virtual Infundibulotomy - Youtube, 2017. https://www.youtube.com/watch?v=Z0Y3-SX9Cvc (accessed December 23, 2022).
[127] B. Tolsdorff, A. Pommert, K.H. Höhne, A. Petersik, B. Pflesser, U. Tiede, R. Leuwer, Virtual reality: A new paranasal sinus surgery simulator, The Laryngoscope 120 (2010) 420–426. https://doi.org/10.1002/lary.20676.
[128] Distributors, (n.d.). https://www.voxel-man.com/distributors/ (accessed December 23, 2022).
[129] Voxel-Man ENT Full System Virtual Reality Simulator, Anat. Wareh. (n.d.). https://anatomywarehouse.com/voxel-man-ent-full-system-virtual-reality-simulator-A-112324 (accessed March 16, 2023).
[130] S.R. Barber, S. Jain, Y.-J. Son, E.H. Chang, Virtual Functional Endoscopic Sinus Surgery Simulation with 3D-Printed Models for Mixed-Reality Nasal Endoscopy, Otolaryngol. - Head Neck Surg. U. S. 159 (2018) 933–937. https://doi.org/10.1177/0194599818797586.
[131] M. Lai, S. Skyrman, C. Shan, D. Babic, R. Homan, E. Edström, O. Persson, G. Burström, A. Elmi-Terander, B.H.W. Hendriks, P.H.N. de With, Correction: Fusion of augmented

reality imaging with the endoscopic view for endonasal skull base surgery; a novel application for surgical navigation based on intraoperative cone beam computed tomography and optical tracking, PloS One 15 (2020) e0229454. https://doi.org/10.1371/journal.pone.0229454.
[132] M. Lai, S. Skyrman, C. Shan, D. Babic, R. Homan, E. Edström, O. Persson, G. Burström, A. Elmi-Terander, B.H.W. Hendriks, P.H.N. de With, Fusion of augmented reality imaging with the endoscopic view for endonasal skull base surgery; a novel application for surgical navigation based on intraoperative cone beam computed tomography and optical tracking, PLoS ONE 15 (2020) e0227312. https://doi.org/10.1371/journal.pone.0227312.
[133] L. Li, J. Yang, Y. Chu, W. Wu, J. Xue, P. Liang, L. Chen, A Novel Augmented Reality Navigation System for Endoscopic Sinus and Skull Base Surgery: A Feasibility Study, PloS One 11 (2016) e0146996. https://doi.org/10.1371/journal.pone.0146996.
[134] B.J. Dixon, H. Chan, M.J. Daly, A.D. Vescan, I.J. Witterick, J.C. Irish, The effect of augmented real-time image guidance on task workload during endoscopic sinus surgery, Int. Forum Allergy Rhinol. 2 (2012) 405–410. https://doi.org/10.1002/alr.21049.
[135] B.J. Dixon, M.J. Daly, H. Chan, A. Vescan, I.J. Witterick, J.C. Irish, Augmented image guidance improves skull base navigation and reduces task workload in trainees: A preclinical trial, The Laryngoscope 121 (2011) 2060–2064. https://doi.org/10.1002/lary.22153.
[136] B.J. Dixon, M.J. Daly, H. Chan, A. Vescan, I.J. Witterick, J.C. Irish, Augmented real-time navigation with critical structure proximity alerts for endoscopic skull base surgery, The Laryngoscope 124 (2014) 853–859. https://doi.org/10.1002/lary.24385.
[137] E. Prisman, M.J. Daly, H. Chan, J.H. Siewerdsen, A. Vescan, J.C. Irish, Real-time tracking and virtual endoscopy in cone-beam CT-guided surgery of the sinuses and skull base in a cadaver model, Int. Forum Allergy Rhinol. 1 (2011) 70–77. https://doi.org/10.1002/alr.20007.
[138] S. Cai, Y. Zhou, J. Shen, J. Guo, X. Xiong, X. Jiang, Augmented Reality Based Surgical Training and Education System for Neurosurgery, in: 2022: pp. 678–681. https://doi.org/10.1109/ICARM54641.2022.9959349.
[139] Phacon – The Patients for your Surgical Demonstration and Education, (n.d.). https://www.phacon.de/en/ (accessed November 17, 2021).
[140] Video Guide | PHACON Sinus Trainer - Youtube, 2021. https://www.youtube.com/watch?v=NDrKDvCdMuE (accessed December 23, 2022).
[141] [S-00005] PHACON Sinus Trainer – Phacon, (n.d.). https://phacon.de/en/produkt/phacon-sinus-trainer-s-00005/ (accessed December 3, 2022).
[142] phacon sinus assistant gettingstarted endoscopy - Youtube, 2020. https://www.youtube.com/watch?v=Iy9QACSR6AY (accessed December 23, 2022).
[143] [S-00007] PHACON Sinus Assistant – Phacon, (n.d.). https://phacon.de/en/produkt/phacon-sinus-assistant-s-00003/ (accessed December 3, 2022).
[144] [SN-ah] PHACON Sinus Patient “Meyer” – pituitary tumor – Phacon, (n.d.). https://phacon.de/en/produkt/sn-ah-phacon-sinus-patient-meyer-hypophysen-tumor/ (accessed May 8, 2023).
[145] The evolution of Neurosurgery Learning | UpSurgeOn, (n.d.). https://www.upsurgeon.com/ (accessed December 23, 2022).
[146] TNS Box | Self-training System for endoscopic pituitary surgery - YouTube, (n.d.). https://www.youtube.com/watch?v=71-lGn5ylck (accessed December 23, 2022).
[147] TNSBox – UpSurgeOn Store, (2023). https://store.upsurgeon.com/product/tnsbox/ (accessed February 28, 2023).

[148] Disposable Cavities – UpSurgeOn Store, (n.d.). https://store.upsurgeon.com/product/disposable-cavities/ (accessed May 8, 2023).
[149] N. Newall, D.Z. Khan, J.G. Hanrahan, J. Booker, A. Borg, J. Davids, F. Nicolosi, S. Sinha, N. Dorward, H. Marcus, High fidelity simulation of the endoscopic transsphenoidal approach: Validation of the UpSurgeOn TNS Box, Front. Surg. 9 (2022). https://doi.org/10.3389/fsurg.2022.1049685.
[150] S. Petrone, F. Cofano, F. Nicolosi, G. Spena, M. Moschino, G. Di Perna, A. Lavorato, M.M. Lanotte, D. Garbossa, Virtual-Augmented Reality and Life-Like Neurosurgical Simulator for Training: First Evaluation of a Hands-On Experience for Residents, Front. Surg. 9 (2022). https://doi.org/10.3389/fsurg.2022.862948.
[151] CardinalSim, CardinalSim (n.d.). https://med.stanford.edu/cardinalsim.html (accessed February 28, 2023).
[152] D.H. Kim, H.M. Kim, J.-S. Park, S.W. Kim, Virtual Reality Haptic Simulator for Endoscopic Sinus and Skull Base Surgeries, J. Craniofac. Surg. 31 (2020) 1811–1814. https://doi.org/10.1097/SCS.0000000000006395.
[153] E.D. Stephenson, D.R. Farquhar, M.M. Masood, G. Capra, A. Kimple, C.S. Ebert, B.D. Thorp, A.M. Zanation, Blinded Evaluation of Endoscopic Skill and Instructability After Implementation of an Endoscopic Simulation Experience, Am. J. Rhinol. Allergy 33 (2019) 681–690. https://doi.org/10.1177/1945892419860973.
[154] A. Chaudhary, S. Chopra, V.D. Sinha, Role of Three-dimensional Printing in Neurosurgery: An Institutional Experience, Asian J. Neurosurg. 16 (2021) 531–538. https://doi.org/10.4103/ajns.AJNS_475_20.
[155] S. Chopra, A.K. Boro, V.D. Sinha, 3D Printing-Assisted Skull Base Tumor Surgeries: An Institutional Experience, J. Neurosci. Rural Pract. 12 (2021) 630–634. https://doi.org/10.1055/s-0041-1734001.
[156] X. Huang, N. Fan, H.-J. Wang, Y. Zhou, X. Li, X.-B. Jiang, Application of 3D printed model for planning the endoscopic endonasal transsphenoidal surgery, Sci. Rep. 11 (2021) 5333. https://doi.org/10.1038/s41598-021-84779-5.
[157] X. Huang, Z. Liu, X. Wang, X.-D. Li, K. Cheng, Y. Zhou, X.-B. Jiang, A small 3D-printing model of macroadenomas for endoscopic endonasal surgery, Pituitary 22 (2019) 46–53. https://doi.org/10.1007/s11102-018-0927-x.
[158] M. de Notaris, K. Palma, L. Serra, J. Enseñat, I. Alobid, J. Poblete, J.B. Gonzalez, D. Solari, E. Ferrer, A. Prats-Galino, A Three-Dimensional Computer-Based Perspective of the Skull Base, World Neurosurg. 82 (2014) S41–S48. https://doi.org/10.1016/j.wneu.2014.07.024.
[159] S.S. Panesar, M. Magnetta, D. Mukherjee, K. Abhinav, B.F. Branstetter, P.A. Gardner, M. Iv, J.C. Fernandez-Miranda, Patient-specific 3-dimensionally printed models for neurosurgical planning and education, Neurosurg. Focus 47 (2019) E12. https://doi.org/10.3171/2019.9.FOCUS19511.
[160] S. Wang, S. Zhang, J. Jing, Stereoscopic virtual reality models for planning tumor resection in the sellar region, BMC Neurol. 12 (2012) 146. https://doi.org/10.1186/1471-2377-12-146.
[161] S.-S. Wang, L. Xue, J.-J. Jing, R.-M. Wang, Virtual reality surgical anatomy of the sphenoid sinus and adjacent structures by the transnasal approach, J. Cranio-Maxillofac. Surg. 40 (2012) 494–499. https://doi.org/10.1016/j.jcms.2011.08.008.
[162] X.-D. Zhang, Z.-H. Li, Z.-S. Wu, W. Lin, W.-J. Lin, J.-C. Lin, L.-M. Zhuang, A novel three-dimensional-printed paranasal sinus–skull base anatomical model, Eur. Arch. Otorhinolaryngol. 275 (2018) 2045–2049. https://doi.org/10.1007/s00405-018-5051-z.
[163] Digital future | Bracco, (n.d.). https://www.bracco.com/en-us/digital-future (accessed March 15, 2023).
[164] Q.-S. Lin, Y.-X. Lin, X.-Y. Wu, P.-S. Yao, P. Chen, D.-Z. Kang, Utility of 3-Dimensional–Printed Models in Enhancing the Learning Curve of Surgery of Tuberculum Sellae

Meningioma, World Neurosurg. 113 (2018) e222–e231. https://doi.org/10.1016/j.wneu.2018.01.215.
[165] M. Bartikian, A. Ferreira, A. Gonçalves-Ferreira, L.L. Neto, 3D printing anatomical models of head bones, Surg. Radiol. Anat. SRA 41 (2019) 1205–1209. https://doi.org/10.1007/s00276-018-2148-4.
[166] J.S. Naftulin, E.Y. Kimchi, S.S. Cash, Streamlined, Inexpensive 3D Printing of the Brain and Skull, PloS One 10 (2015) e0136198. https://doi.org/10.1371/journal.pone.0136198.
[167] M.S. Singhvi, S.S. Zinjarde, D.V. Gokhale, Polylactic acid: synthesis and biomedical applications, J. Appl. Microbiol. 127 (2019) 1612–1626. https://doi.org/10.1111/jam.14290.
[168] D. Mitsouras, P. Liacouras, A. Imanzadeh, A.A. Giannopoulos, T. Cai, K.K. Kumamaru, E. George, N. Wake, E.J. Caterson, B. Pomahac, V.B. Ho, G.T. Grant, F.J. Rybicki, Medical 3D Printing for the Radiologist, Radiogr. Rev. Publ. Radiol. Soc. N. Am. Inc 35 (2015) 1965–1988. https://doi.org/10.1148/rg.2015140320.
[169] L. Riva, R. Pagani, A. Fiorentino, A. Borboni, Additive manufacturing of PLA to mimic the thrust force of mandibular bone during drilling, in: 2022: pp. 199–202. https://doi.org/10.1016/j.procir.2022.06.036.
[170] K. Oyama, L.F.S. Ditzel Filho, J. Muto, D.G. de Souza, R. Gun, B.A. Otto, R.L. Carrau, D.M. Prevedello, Endoscopic endonasal cranial base surgery simulation using an artificial cranial base model created by selective laser sintering, Neurosurg. Rev. 38 (2015) 171–178; discussion 178. https://doi.org/10.1007/s10143-014-0580-4.
[171] M. Suzuki, Y. Ogawa, A. Kawano, A. Hagiwara, H. Yamaguchi, H. Ono, Rapid prototyping of temporal bone for surgical training and medical education, Acta Otolaryngol. (Stockh.) 124 (2004) 400–402. https://doi.org/10.1080/00016480410016478.
[172] K. Mori, T. Yamamoto, K. Oyama, Y. Nakao, Modification of three-dimensional prototype temporal bone model for training in skull-base surgery, Neurosurg. Rev. 32 (2009) 233–239. https://doi.org/10.1007/s10143-008-0177-x.
[173] J.B. Hochman, J. Kraut, K. Kazmerik, B.J. Unger, Generation of a 3D printed temporal bone model with internal fidelity and validation of the mechanical construct, Otolaryngol.--Head Neck Surg. Off. J. Am. Acad. Otolaryngol.-Head Neck Surg. 150 (2014) 448–454. https://doi.org/10.1177/0194599813518008.
[174] J.B. Hochman, C. Rhodes, D. Wong, J. Kraut, J. Pisa, B. Unger, Comparison of cadaveric and isomorphic three-dimensional printed models in temporal bone education, Laryngoscope 125 (2015) 2353–2357. https://doi.org/10.1002/lary.24919.
[175] B.L. Tai, Y.-T. Kao, N. Payne, Y. Zheng, L. Chen, A.J. Shih, 3D Printed composite for simulating thermal and mechanical responses of the cortical bone in orthopaedic surgery, Med. Eng. Phys. 61 (2018) 61–68. https://doi.org/10.1016/j.medengphy.2018.08.004.
[176] A.K. Dąbrowska, G.-M. Rotaru, S. Derler, F. Spano, M. Camenzind, S. Annaheim, R. Stämpfli, M. Schmid, R.M. Rossi, Materials used to simulate physical properties of human skin, Skin Res. Technol. 22 (2016) 3–14. https://doi.org/10.1111/srt.12235.
[177] P. Liacouras, J. Garnes, N. Roman, A. Petrich, G.T. Grant, Designing and manufacturing an auricular prosthesis using computed tomography, 3-dimensional photographic imaging, and additive manufacturing: a clinical report, J. Prosthet. Dent. 105 (2011) 78–82. https://doi.org/10.1016/S0022-3913(11)60002-4.
[178] G. Lamouche, B.F. Kennedy, K.M. Kennedy, C.-E. Bisaillon, A. Curatolo, G. Campbell, V. Pazos, D.D. Sampson, Review of tissue simulating phantoms with controllable optical, mechanical and structural properties for use in optical coherence tomography, Biomed. Opt. Express 3 (2012) 1381–1398. https://doi.org/10.1364/BOE.3.001381.

[179] M. Bjellerup, Novel method for training skin flap surgery: polyurethane foam dressing used as a skin equivalent, Dermatol. Surg. Off. Publ. Am. Soc. Dermatol. Surg. Al 31 (2005) 1107–1111. https://doi.org/10.1097/00042728-200509000-00004.
[180] Z. Shen, Y. Xie, X. Shang, G. Xiong, S. Chen, Y. Yao, Z. Pan, H. Pan, X. Dong, Y. Li, C. Guo, F.-Y. Wang, The manufacturing procedure of 3D printed models for endoscopic endonasal transsphenoidal pituitary surgery, Technol. Health Care Off. J. Eur. Soc. Eng. Med. 28 (2020) 131–150. https://doi.org/10.3233/THC-209014.
[181] N. Harada, K. Kondo, C. Miyazaki, J. Nomoto, S. Kitajima, M. Nemoto, H. Uekusa, M. Harada, N. Sugo, Modified Three-Dimensional Brain Model for Study of the Trans-sylvian Approach, Neurol. Med. Chir. (Tokyo) 51 (2011) 567–571. https://doi.org/10.2176/nmc.51.567.
[182] J. Lin, Z. Zhou, J. Guan, Y. Zhu, Y. Liu, Z. Yang, B. Lin, Y. Jiang, X. Quan, Y. Ke, T. Xu, Using Three-Dimensional Printing to Create Individualized Cranial Nerve Models for Skull Base Tumor Surgery, World Neurosurg. 120 (2018) e142–e152. https://doi.org/10.1016/j.wneu.2018.07.236.
[183] M. Berhouma, N.B. Baidya, A.A. Ismaïl, J. Zhang, M. Ammirati, Shortening the learning curve in endoscopic endonasal skull base surgery: a reproducible polymer tumor model for the trans-sphenoidal trans-tubercular approach to retro-infundibular tumors, Clin. Neurol. Neurosurg. 115 (2013) 1635–1641. https://doi.org/10.1016/j.clineuro.2013.02.013.
[184] T. Okuda, K. Kataoka, A. Kato, Training in endoscopic endonasal transsphenoidal surgery using a skull model and eggs, Acta Neurochir. (Wien) 152 (2010) 1801–1804. https://doi.org/10.1007/s00701-010-0728-0.
[185] D.C. Engel, A. Ferrari, A.-J. Tasman, R. Schmid, R. Schindel, S.R. Haile, L. Mariani, J.-Y. Fournier, A basic model for training of microscopic and endoscopic transsphenoidal pituitary surgery: the Egghead, Acta Neurochir. (Wien) 157 (2015) 1771–1777; discussion 1777. https://doi.org/10.1007/s00701-015-2544-z.
[186] T. Mashiko, T. Konno, N. Kaneko, E. Watanabe, Training in Brain Retraction Using a Self-Made Three-Dimensional Model, World Neurosurg. 84 (2015) 585–590. https://doi.org/10.1016/j.wneu.2015.03.058.
[187] UltiMaker PLA TDS, (n.d.). https://support.makerbot.com/s/article/1667410781972 (accessed November 25, 2024).
[188] C. Zhuo, L. Lei, Z. Yulin, L. Wentao, W. Shuangxia, W. Chao, Z. Yaqian, H. Shuman, D. Dong, Creation and validation of three-dimensional printed models for basic nasal endoscopic training, Int. Forum Allergy Rhinol. 9 (2019) 695–701. https://doi.org/10.1002/alr.22306.
[189] UltiMaker TPU 95A TDS, (n.d.). https://support.makerbot.com/s/article/1667410781018 (accessed November 25, 2024).
[190] Download SDS and Technical Bulletins (TB/TDS), Smooth- Inc (n.d.). https://www.smooth-on.com/documents/?doc=all (accessed November 25, 2024).
[191] A. Colpani, A. Fiorentino, E. Ceretti, Feasibility analysis and characterization of an extrusion-based AM process for a two-component and biocompatible silicone, J. Manuf. Process. 49 (2020) 116–125. https://doi.org/10.1016/j.jmapro.2019.11.017.
[192] G. Santona, T. Fapanni, A. Fiorentino, F. Doglietto, M. Serpelloni, Preliminary study of a sensorized system for real-time feedback for arachnoid collapse during neurosurgical training, in: 2023 IEEE Int. Workshop Metrol. Ind. 40 IoT MetroInd40IoT, 2023: pp. 233–238. https://doi.org/10.1109/MetroInd4.0IoT57462.2023.10180173.
[193] T. Okuda, J. Yamashita, M. Fujita, H. Yoshioka, T. Tasaki, A. Kato, The chicken egg and skull model of endoscopic endonasal transsphenoidal surgery improves trainee drilling skills, Acta Neurochir. (Wien) 156 (2014) 1403–1407. https://doi.org/10.1007/s00701-014-2035-7.

[194] G. Wen, Z. Cong, K. Liu, C. Tang, C. Zhong, L. Li, X. Dai, C. Ma, A practical 3D printed simulator for endoscopic endonasal transsphenoidal surgery to improve basic operational skills, Childs Nerv. Syst. ChNS Off. J. Int. Soc. Pediatr. Neurosurg. 32 (2016) 1109–1116. https://doi.org/10.1007/s00381-016-3051-0.
[195] G. Santona, T. Fapanni, A. Fiorentino, F. Doglietto, M. Serpelloni, Preliminary Study on a 3D Printed Sensorized Probe to Characterize Pituitary Adenoma Hardness, 2023. https://doi.org/10.1109/MetroInd4.0IoT57462.2023.10180133.
[196] G. Santona, A. Fiorentino, F. Doglietto, M. Serpelloni, A Novel 3D Printed Sensorized Surgical Instrument to Characterize Pituitary Adenoma: Development and Initial Validation, in: 2024 IEEE Int. Workshop Metrol. Ind. 40 IoT MetroInd40 IoT, 2024: pp. 7–11. https://doi.org/10.1109/MetroInd4.0IoT61288.2024.10584245.
[197] J.H. Thomas, Fluid dynamics of cerebrospinal fluid flow in perivascular spaces, J. R. Soc. Interface 16 (2019) 20190572. https://doi.org/10.1098/rsif.2019.0572.
[198] M.A. Masalha, K.K. VanKoevering, O.S. Latif, A.R. Powell, A. Zhang, K.H. Hod, D.M. Prevedello, R.L. Carrau, Simulation of Cerebrospinal Fluid Leak Repair Using a 3-Dimensional Printed Model, Am. J. Rhinol. Allergy 35 (2021) 802–808. https://doi.org/10.1177/19458924211003537.
[199] J.R. Bekeny, P.J. Swaney, R.J. Webster III, P.T. Russell, K.D. Weaver, Forces applied at the skull base during transnasal endoscopic transsphenoidal pituitary tumor excision, J. Neurol. Surg. Part B Skull Base 74 (2013) 337–341. https://doi.org/10.1055/s-0033-1345108.
[200] V.A. Chandankhede, S.K. Singh, R. Roy, S. Goyal, M.S. Sridhar, M.S. Gill, Transnasal Transsphenoidal Approach for Pituitary Tumors: An ENT Perspective, Indian J. Otolaryngol. Head Neck Surg. 72 (2020) 239–246. https://doi.org/10.1007/s12070-020-01803-2.
[201] M.J. Rutkowski, K.-E. Chang, T. Cardinal, R. Du, A.R. Tafreshi, D.A. Donoho, A. Brunswick, A. Micko, C.-S.J. Liu, M.S. Shiroishi, J.D. Carmichael, G. Zada, Development and clinical validation of a grading system for pituitary adenoma consistency, J. Neurosurg. 134 (2020) 1800–1807. https://doi.org/10.3171/2020.4.JNS193288.
[202] L. Wei, S. Lin, K. Fan, D. Xiao, J. Hong, S. Wang, Relationship between pituitary adenoma texture and collagen content revealed by comparative study of MRI and pathology analysis, (n.d.).
[203] J. Yamamoto, S. Kakeda, S. Shimajiri, M. Takahashi, K. Watanabe, Y. Kai, J. Moriya, Y. Korogi, S. Nishizawa, Tumor Consistency of Pituitary Macroadenomas: Predictive Analysis on the Basis of Imaging Features with Contrast-Enhanced 3D FIESTA at 3T, Am. J. Neuroradiol. 35 (2014) 297–303. https://doi.org/10.3174/ajnr.A3667.
[204] D. De Alcubierre, G. Puliani, A. Cozzolino, V. Hasenmajer, M. Minnetti, V. Sada, V. Martines, A. Zaccagnino, A.G. Ruggeri, R. Pofi, E. Sbardella, M.A. Venneri, Pituitary adenoma consistency affects postoperative hormone function: a retrospective study, BMC Endocr. Disord. 23 (2023) 92. https://doi.org/10.1186/s12902-023-01334-1.
[205] K.A. Smith, J.D. Leever, R.B. Chamoun, Prediction of Consistency of Pituitary Adenomas by Magnetic Resonance Imaging, J. Neurol. Surg. Part B Skull Base 76 (2015) 340–343. https://doi.org/10.1055/s-0035-1549005.
[206] A. Acitores Cancela, V. Rodríguez Berrocal, H. Pian, J.S. Martínez San Millán, J.J. Díez, P. Iglesias, Clinical relevance of tumor consistency in pituitary adenoma, Hormones 20 (2021) 463–473. https://doi.org/10.1007/s42000-021-00302-5.
[207] M. Černý, V. Sedlák, V. Lesáková, P. Francůz, D. Netuka, Methods of preoperative prediction of pituitary adenoma consistency: a systematic review, Neurosurg. Rev. 46 (2022) 11. https://doi.org/10.1007/s10143-022-01909-x.
[208] K. Navindaran, J.S. Kang, K. Moon, Techniques for characterizing mechanical properties of soft tissues, J. Mech. Behav. Biomed. Mater. 138 (2023) 105575. https://doi.org/10.1016/j.jmbbm.2022.105575.

[209] R.M.A. Hassan, Y.E. Almalki, M.A.A. Basha, S.K. Alduraibi, A.H. Hassan, M. Aboualkheir, Z.A. Almushayti, A.K. Alduraibi, M.M. Amer, A.M.A. Basha, M.M. Refaat, Predicting the Consistency of Pituitary Macroadenomas: The Utility of Diffusion-Weighted Imaging and Apparent Diffusion Coefficient Measurements for Surgical Planning, Diagnostics 14 (2024) 493. https://doi.org/10.3390/diagnostics14050493.

[210] F. Bioletto, N. Prencipe, A.M. Berton, L.S. Aversa, D. Cuboni, E. Varaldo, V. Gasco, E. Ghigo, S. Grottoli, Radiomic Analysis in Pituitary Tumors: Current Knowledge and Future Perspectives, J. Clin. Med. 13 (2024) 336. https://doi.org/10.3390/jcm13020336.

[211] D.C. Stewart, A. Rubiano, K. Dyson, C.S. Simmons, Mechanical characterization of human brain tumors from patients and comparison to potential surgical phantoms, PloS One 12 (2017) e0177561. https://doi.org/10.1371/journal.pone.0177561.

[212] Stiffness Assessment and Lump Detection in Minimally Invasive Surgery Using In-House Developed Smart Laparoscopic Forceps, IEEE J. Transl. Eng. Health Med. 10 (2022) 2500410. https://doi.org/10.1109/JTEHM.2022.3180937.

[213] A.K. Golahmadi, D.Z. Khan, G.P. Mylonas, H.J. Marcus, Tool-tissue forces in surgery: A systematic review, Ann. Med. Surg. 2012 65 (2021) 102268. https://doi.org/10.1016/j.amsu.2021.102268.